Development and improved fabrication of microfluidic devices for local delivery to investigate properties of healthy and inflamed lymph node tissue ex vivo slices.

Megan Ann Catterton

Severn, Maryland

B.A. Chemistry, St. Mary's College of Maryland, 2014

A Dissertation presented to the Graduate Faculty of the University of Virginia in Candidacy

for the Degree of Doctor of Philosophy

Department of Chemistry

University of Virginia

May 2021

Abstract:

Local delivery of chemical analytes to ex vivo tissue slices is a useful mechanism for studying their intrinsic properties, such as diffusivity and tortuosity, which can give new insights into healthy tissue homeostasis and diseased tissue states. Microfluidic devices allow for the manipulation of small volumes of liquid and are well suited to preform local delivery to tissues. **Chapter 2** demonstrates the potential of local delivery devices to study tissue properties by investigating the diffusivity of inflamed lymph node tissue after vaccination, and characterizing the diffusion coefficients. Mice were vaccinated with different adjuvants, which are the components of vaccines that promote an immune response. Adjuvant-dependent changes in diffusivity and tortuosity were observed. One of the limitations with previous static delivery port microfluidic devices is the handling of the tissue that is required by the user to target sub-sections of the tissue. Tissue slices are fragile and extraneous handling can cause mechanical damage. **Chapter 3** will improve local delivery technology by directly addressing user-handling with a SlipChip design. A SlipChip is a two-phase microfluidic device that consists of two components separated by an oil layer allowing for rearrangement of the fluidic pathway. Using the SlipChip, we can protect the tissue slice from excessive handling by housing the tissue in a chamber and reconfiguring the device to position a port beneath a tissue. The movable microfluidic port device was able to target substructures as small as 200 μm. The first iteration of this movable microfluidic port device required extensive fabrication steps to achieve the design. Digital light processing (DLP) 3D printing is an alternative fabrication method that can simplify the fabrication of the device to make it more accessible for other collaborators and allow for rapid prototyping of more sophisticated designs. Achieving a 3D printed SlipChip movable port device required verification that resin printing can create a fluorinated surface that is flat, smooth and optically clear. **Chapter**

4, highlights the validation of a versatile and robust method to selectively pattern a fluorinated surface onto a DLP printed component. Utilizing a fluoroalkyl silane, this novel method only requires a simple coating step without prior surface activation. Using this surface modification method, the first SlipChip with DLP 3D printing is fabricated in **Chapter 5.** First, I investigated the optical transparency, surface smoothness, and biocompatibility of the printed parts, to ensure they were adequate for the movable port device. Then printed movable port SlipChip successfully delivered to sequentially tissue without any leakage. The work in this thesis has focused primarily on improving local delivery to tissue while demonstrating the need for such technology to probe intrinsic properties of tissues. The future of this technology is dependent on the accessibility to collaborators, which has been achieved through 3D printing and is now set up to advance even further.

This dissertation is dedicated in memory to Mary and James Catterton, my dearest Grandparents. Even though you are no longer with me, I still feel your love for me and I am the person I am today because of you and your guidance.

Acknowledgements:

Earning my Ph.D. has been one of the most challenging and rewarding experiences of my life. Like every adventure and stage in life there have been low moments, but I knew going through graduate school that the journey was worth it and that there was nothing else I would rather be doing with my life. Standing on the precipice of the end, there are so many people I have to thank for their help along the way. First, I would like to thank Dr. Rebecca Pompano for being my advisor. When I joined the lab there was only three members, and through the years I have had the privilege to see the lab grow and you along with it into the amazing mentor you are today. It has been an amazing and unique experience to be a part of the beginning of a lab that I know will one day be a leader in the field. You inspire me with your hard work and dedication through the years and have pushed me to the be a better scientist. You encouraged me to be creative with my work, but was also there to force me to slow down and critically evaluate the problem that I need to solve. Thank you for suffering through so many of my bad paper drafts as you endeavored to make me a better writer. Your support has helped me through these last 6 years and I cannot express how grateful I am to have had you as a mentor.

Next, I want thank my lab mates. We have prided ourselves on being a lab that is collaborative and friendly, and without you all graduate school would have been a lonely endeavor. I love you all and I am so grateful you all put up with my shenanigans and event planning schemes. Some of my favorite memories came from the many lab events like the Christmas parties, but what I appreciate the most were the everyday interactions of telling silly stories, gushing over the latest tv craze and getting to know everyone over the last couple of years. A special thank you to two amazing undergraduate researchers Tim Freeman and Alyssa Montalbine, for your help on work presented in this thesis. Mentoring you both has pushed me to be a better teacher, mentor and

communicator. You both astound me with your brilliance, and I wish you both luck as you embark on your further graduate work.

There are two Alumnus from the lab that I would like to thank specifically. The first is Dr. Ashley Ross who was a post-doc when I first joined the lab and who's work was the basis for the start of my thesis. She also was the first person to mentor and train me in the lab and taught me so many necessary skills. Next, I have to thank my lab husband Dr. Maura Belanger, you were my better half in lab. You were always there to help edit any of my writing, listen to any troubleshooting ideas I had and rant to about the latest bad book I had read. Our adventures to escape rooms, Disney cruises and the various concerts were some of my best memories during the last 6 years. I am so lucky to have you as a friend, and I could not have done this without you.

The friends I have made in Charlottesville are some of the most caring and wonderful people I have ever known. Thank you, Michael and Alexa, for the fun TV nights, great debates and cookies. Michael you are like the brother I never had and your friendship and support helped me so much especially during the first two busy years of grad school. Alexa, we've shared such fun trips both on the east and west coast, your unending thirst for life and new experiences has led to so many fun times together. Love ya, Chica. Mary, Ressi and Bill, my Waynesboro buddies thank you for giving me a place to escape to when research was hard and my experiments weren't working.

Finally, I would like to thank my family whose support has been crucial over the last few years. Mom and Dad thank you for the love and support, even when you were not sure what I was doing with the crazy chemistry degree. Morgan and Madison, you've inspired me with the wonderful young women you have become. I hope to have your drive and determination Mad, and your poise and courage to try new things Momo. I love you all so much and you mean everything to me.

Table of Contents

Abstract: i
Acknowledgements: iv
Table of Contents vi
List of figures x
List of Tables xii
List of Equations xiii
Chapter 1: Introduction 1.1
1.1 Local chemical stimulation is necessary for a better understanding of tissue response 1.1
1.2 Cell function and communication is dependent of tissue organization 1.1
1.2.1 Diffusion is a major component of cellular communication 1.3
1.2.2 Lymph nodes as a model system to target for local delivery 1.4
1.3 Different model systems for studying protein transport and responses in lymph nodes 1.5
1.4 Microfluidic devices are a strategy for local delivery to tissue 1.7
1.4.1 Microfluidics are well suited for biological applications including tissue culture 1.7
1.4.2 A brief history of microfluidics 1.7
1.4.3 Foundational physics necessary for microfluidics devices. 1.9
1.4.4 Microfluidics devices can be used for local stimulation 1.12
1.5 Research Goals and Concluding Remarks 1.12
1.6 References: 1.13
Chapter 2: Diffusivity of immunized lymph node tissue measured with microfluidic integrated optical imaging 2.21
2.1 Abstract: 2.21
2.2 Introduction: 2.22
2.3 Methods: 2.24
2.3.1 Device Fabrication 2.24
2.3.2 Animal work: 2.24
2.3.3 Tissue slice collection 2.25
2.3.4 Delivery and data collection 2.25
2.3.5 Data analysis 2.26
2.3.6 Tortuosity measurements 2.27
2.3.7 Predictions of Free Diffusion coefficients 2.28
2.4 Results and Discussion: 2.28

2.4.1 Experimental design and set up 2.28
2.4.2 Diffusivity of non-binding dextrans in immunized tissues 2.29
2.4.3 Diffusivity of an anti-inflammatory immunotherapeutic in immunized tissues 2.32
2.4.4 Tortuosity of immunized tissue and area inflamed node 2.35
2.5 Proposed work: 2.36
2.5.1 Repeating diffusivity experiments at 37˚C 2.36
2.5.2 Directly measuring the extracellular space of a live lymph node slice 2.37
2.6 Conclusions: 2.39
2.7 References: 2.39
Chapter 3: User-defined local stimulation of live tissue through a movable microfluidic port 3.44
3.1 Abstract 3.44
3.2 Introduction 3.45
3.3 Methods 3.47
3.3.1 Device Fabrication 3.47
3.3.2 R_fOEG synthesis 3.49
3.3.3 Interfacial tension and contact angle measurements 3.49
3.3.4 Fluorosilanization of delivery and chamber components 3.50
3.3.5 Preparation of agarose and tissue slices 3.50
3.3.6 Device assembly and operation 3.51
3.3.7 Measurement of gap height 3.52
3.3.8 Validation of tissue viability after delivery 3.53
3.3.9 Delivery experiments 3.54
3.4 Results and Discussion 3.56
3.4.1 Design of the chip 3.56
3.4.2 Design criteria for fabrication and surface chemistry 3.57
3.4.3 Capillary pressure provided controlled delivery without leakage 3.59
3.4.4 Delivery into the sample was governed by convection 3.63
3.4.5 Tissue viability was not affected by stimulation on the device 3.66
3.4.6 On-demand stimulation of live tissue slices through the movable port 3.67
3.5 Conclusions 3.70
3.6 References: 3.70
Chapter 4: Versatile and selective fluorination of the surface of polymeric materials after stereolithography 3D printing 4.76
4.1 Abstract 4.76
4.2 Introduction 4.77

4.3 Methods 4.79
4.3.1 3D Printing 4.79
4.3.2 Surface Treatment of 3D Printed Pieces 4.80
4.3.3 Contact Angle Measurement 4.80
4.3.4 Surface Chemistry Characterization with Infrared Spectroscopy 4.81
4.3.5 Robustness testing 4.81
4.3.6 Selective Patterning of 3D Printed Surfaces 4.81
4.3.7 Data Analysis 4.82
4.4 Results and Discussion 4.83
4.4.1 Plasma oxidation was not necessary or effective for silanization of SLA printed pieces 4.83
4.4.2 Solvent deposition was most effective when a fluorocarbon oil was used as a solvent. 4.86
4.4.3 Time dependence of the reaction provides support for covalent bond formation 4.86
4.4.4 Robustness and stability of fluorination procedure 4.88
4.4.5 Patterning of surface hydrophobicity on 3D printed parts 4.90
4.4.6 Silanization of a suite of SLA resins demonstrates broad applicability 4.93
4.5 Conclusions 4.95
4.6 References 4.95
Chapter 5: Rapid fabrication of a polymeric SlipChip with movable ports by digital light processing 3D printing 5.102
5.1 Abstract: 5.102
5.2 Introduction 5.103
5.3 Methods 5.106
5.3.1 Device design, 3D printing, and laser etching 5.106
5.3.2 Fluorination of resin surface and contact angle measurements 5.107
5.3.3 Surface profilometry 5.106
5.3.4 Animal work and tissue slice collection 5.107
5.3.5 Analysis of tissue viability 5.108
5.3.6 Assembly and local delivery with the 3D printed SlipChip 5.109
5.3.7 Analysis of delivery widths 5.110
5.3.8 Delivery to lymph node tissue 5.111
5.3.9 Measurement of curvature of printed pieces 5.107
5.4 Results and Discussion 5.112

5.4.1 DLP Resin material considerations for use in a SlipChip device 5.112
5.4.2 Optimization of the key features of the channel component. 5.115
5.4.3 Optimization of the chamber component. 5.118
5.4.4 The DLP printed Movable Port SlipChip was tested for functionality 5.120
5.4.5 Future outlook for the technical advancment of the movable port device 5.121
5.5 Conclusion: 5.122
5.6 References: 5.123
Chapter 6: Conclusions and Future Directions 6.127
6.1 Conclusions 6.127
6.2 Future Directions 6.129
6.2.1 Biocompatibility of 3D resin 6.129
6.2.2 Modifications to the movable port device design 6.131
6.2.3 Incorporating in-tissue assays for spatially resolved read-outs 6.133
6.2.4 Develop a microfluidic device for rapid immunohistostaining of live tissue slices. 6.134
6.3 References: 6.135

List of Figures

Figure 1.1 Cell signaling is dependent on diffusion.. ..... 1.3
Figure 1.2 Schematic of lymph node with a B cell follicle, T cell zone and medulla labelled. .. 1.5
Figure 1.3 Various strategies for fabrication of microfluidic devices.. ..... 1.8
Figure 1.4 Schematic of relevant device dimensions and capillary pressure. 1.10

Figure 2.1 Overview of experimental design and the microIOI device. 2.28
Figure 2.2 An example delivery and Day 1 post-vaccination effective diffusion coeffiecents. 2.30
Figure 2.3 The effective Diffusion coefficients of 3, 10 and 70 kDa dextrans on day 4 post vaccination. 2.31
Figure 2.4 The mean effective diffusion coefficients of two antibodies.. ..... 2.32
Figure 2.5: Area of lymph nodes after vaccination. 2.35
Figure 2.6 Visualizing the extracellular space in lymph nodes. 2.37

Figure 3.1 Design and prototype of the movable port device. 3.56
Figure 3.2: Fabrication strategy for the movable port device. 3.57
Figure 3.3 Interfacial tension of 1xPBS and FC-40 oil as a function of the concentration of RfOEG. 3.58
Figure 3.4: Delivery through aligned ports was controlled by the capillary pressure and pressure due to flow resistance 3.59
Figure 3.5 Wetting on the top surface of the gap. 3.62
Figure 3.6 The spread of analyte was controlled by the flow rate and length of delivery. 3.64
Figure 3.7 An illustration of the geometry used to calculate the Peclét number. 3.65
Figure 3.8: Tissue viability was unaffected by stimulation on the device. 3.66
Figure 3.9 The SlipChip-based device was capable of multiple deliveries to lymph node slices. 3.68

Figure 4.1: Effects of plasma treatment and silanization on the chemistry and hydrophobicity of DLP printed pieces. 4.83
Figure 4.2 Air/water contact angles of BV007A after silanization. 4.84
Figure 4.3 The ATR FT-IR spectra of a 1.5 mm acrylic sheet. 4.85
Figure 4.4: Time dependence of the chemical reaction. 4.87
Figure 4.5 Normalized data of the contact angle, carbonyl peak area, and fingerprint area after various amount of time exposed to the fluoroalkyl silane. 4.88
Figure 4.6 Robustness of the method to the age of the printed piece, abrasion, and storage time after silanization. 4.89
Figure 4.7 Using the optimized silanization procedure for surface patterning and on other SLA/DLP resins. 4.92

Figure 5.1 Investigation the compatibility of the resin for optical transparency, surface roughness, surface chemistry, and biocompatibility. 5.112
Figure 5.2 The optimization of the channel component of the movable port device. 5.115
Figure 5.4: Port array for size optimization. 5.117

Figure 5.3 The optimization of the chamber component of the movable port device. 5.118
Figure 5.5 Laser etched port shapes. 5.119
Figure 5.6 Demonstration of local delivery to both agarose and live tissue slices. 5.120

Figure 6.1 Conceptual design for culturing with chamber component of the movable port device. 6.132
Figure 6.2 Conceptual design of a three-channel delivery component for the movable port device. 6.132
Figure 6.3 Schematic for local stimulation of lymph node coupled with a glucose uptake assay. 6.133
Figure 6.4 COMSOL modeling was used to simulate the fluid velocity through the device. . 6.135

List of Tables

Table 2.1 Free diffusion Coefficients Measurements. 2.30
Table 2.2 Diffusion coefficients and Tortuosity calculations. 2.34
Table 2.3 Diffusion coefficients measured for 10 kDa dextran in naïve tissue 2.36

Table 3.1: Capillary pressure calculations for conditions tested in Figure 3b. 3.60
Table 3.2: Calculation of pressure due to flow resistance for varied flow rates in Figure 3b. .. 3.61

Table 4.1: Printing settings for different resin on the 405 nm light source CADworks3D M50 printer. 4.80
Table 4.2 The contact angle for plasma treated glass and PDMS. 4.86

Table 5.1 Port diameter was optimized for consistency and the smallest size 5.119

List of Equations

Equation 1.1 ..... 1.4
Equation 1.2 ..... 1.10
Equation 1.3 ..... 1.10
Equation 1.4 ..... 1.10
Equation 1.5 ..... 1.11
Equation 1.6 ..... 1.11

Equation 2.1 ..... 2.26
Equation 2.2 ..... 2.27
Equation 2.3 ..... 2.27
Equation 2.4 ..... 2.27
Equation 2.5 ..... 2.28
Equation 2.6 ..... 2.37

Equation 3.1 ..... 3.53
Equation 3.2 ..... 3.55
Equation 3.3 ..... 3.55
Equation 3.4 ..... 3.60
Equation 3.5 ..... 3.61
Equation 3.6 ..... 3.61
Equation 3.7 ..... 3.65

Equation 4.1 ..... 4.82
Equation 4.2 ..... 4.89

Chapter 1: Introduction

1.1 Local chemical stimulation is necessary for a better understanding of tissue responses

Coordinated responses in a tissue or body start from localized events, yet the primary approach when studying ex vivo tissue stimulation, as compared to in vivo signals, is to use a global stimulation.[1] Global stimulation activates the entire sample in a uniform manner, which is in direct contrast to how signaling throughout tissues naturally occurs. Many diseases such as stroke or seizure start from a local disruption to cell signaling or in the vessels structure of brain tissue.[2,3] A homeostatic example of local stimulation affecting a cascade response is the initiation of skeletal muscle contraction.[4] Another example of a local change generating a response is the adaptive immune response in the lymph node where a cascade of cell types are activated to fight infections to protect the host organism.[5] Microfluidic devices are uniquely suited to perform localized chemical stimulation to ex vivo tissues to better mimic in vivo events.[6,7] Controlling and selectively perturbing the tissue microenvironment with local delivery is advantageous for future development of novel therapeutics and drugs, as well as understanding protein transport in healthy and diseased states of tissues.

1.2 Cell function and communication is dependent on tissue organization

Structural organization of tissues plays a crucial role in the maintenance of homeostasis. The body is comprised of different organ systems that have evolved to have a specific function and work together to maintain homeostasis. These organs are made up of tissues, which are an organized collection of cells and their surrounding matrix. The extracellular matrix (ECM) is the non-cellular component present in all tissues that provides structure and aids in function.[8] The ECM is responsible for biochemical and biomechanical cues for tissue morphogenesis, differentiation and homeostasis.[9,10] Components within tissues work in a coordinated fashion to

perform tissue specific functions such as: secretion, excretion, protection, communication, structural support and movement.[11] The organization within a tissue is important, as it allows cells to communicate effectively and carry out the function of the tissue.[12–15] Disease occurs when there is a disruption in the structure or communication pathways within the tissue microenvironment.[16] Therefore, understanding tissue and its surrounding microenvironment is important for understanding both healthy and diseased tissue states.[17]

To coordinate tissue function and maintain homeostasis, cells must be able to successfully communicate within tissues. Cells interact with their surroundings through physical and chemical cues, which can stimulate or trigger responses such as cell growth, proliferation, differentiation, motility, and apoptosis.[18] Physical cues that will trigger a cellular response include the stiffness and mechanical properties of the surrounding matrix, and fluid flow.[19] Here I will focus on the immune system as a case study for chemical communication, though this phenomenon is present in many other body functions as well. Immune responses utilizes small signaling proteins called cytokines and chemokines.[20] A cytokine is a small (5-20 kDa) protein that is produced and secreted by a cell. The cytokine can modulate the behavior of either the cytokine-secreting cell or the cells surrounding it.[21] Cytokines generally enhance or inhibit other signaling between cells. A chemokine is a subset of cytokine that induces a chemotactic response resulting in the directed movement of cells. Chemokines can be soluble or bound to the extracellular matrix.[20] Movement of these signaling proteins plays a key role in cellular communication and the spatiotemporal distribution of the proteins affects how the signal is transmitted throughout the tissue.[22]

1.2.1 Diffusion is a major component of cellular communication

Signaling molecules within the tissue must propagate from a point source to conduct a coordinated response. There are different ranges for cellular communication: autocrine and juxtracrine signals have the shortest ranges where the cell signals to itself or only direct neighbors respectively, paracrine signals have a range of 40 to 200 µm (multiple cell lengths), and endocrine signals traverse the entire body (Figure 1.1a-d).[22] Signaling range is affected by a host of factors but of most interest to this work is the ability of signals to move freely through the tissue. Movement of signaling proteins through tissue is affected by active transport mechanism, convective fluid flow, and diffusion. Both active transport and convective flow is necessary for

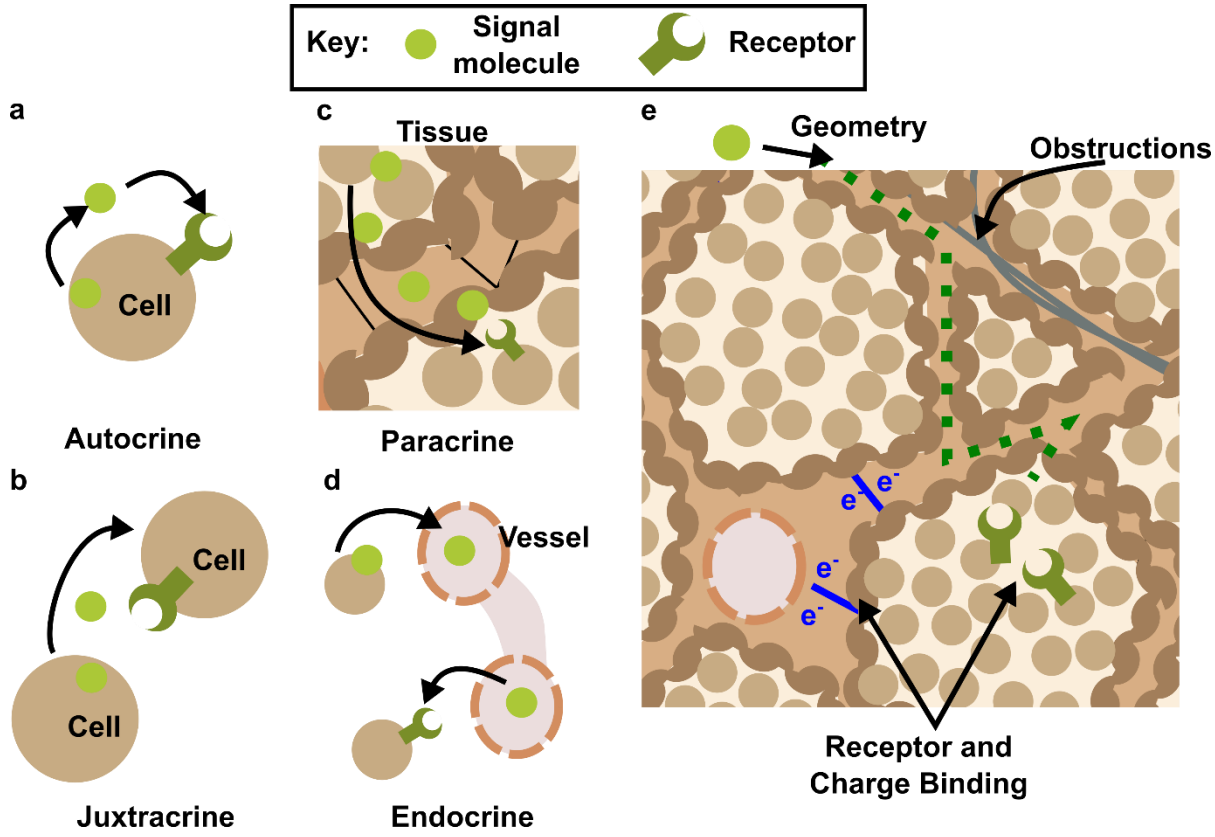

Figure 1.1 Cell signaling is dependent on diffusion. Schematic of the different types of cell signaling: (a) autocrine, (b) juxtracrine, (c) paracrine, and (d) endocrine. (e) Diffusion of signaling molecules is hindered by the geometry of the tissue, obstructions in the extracellular space, and binding events within the tissue.

endocrine signaling[22,23] while diffusion plays a key role in paracrine signaling as seen in this thesis.[22]

Diffusion within tissue is complex due to a variety of hinderances small molecules can encounter in the extracellular space (ECS). Diffusion is the movement of molecules from high concentration to low concentration. Diffusion of proteins in tissue can be hindered by the geometry and obstructions within the ECS, and binding events to the ECM or to their receptors on other cells (Figure 1.1e).[24,25] Diffusion for small proteins follow a random walk pattern, we can be express by the expression

$$x^2 = 2nDt \qquad \text{Equation 1.1,}$$

where x^2 is the mean displacement, n is the number of dimensions (1, 2 or 3), D is the diffusion coefficient (m^2/s), and t is time (s).[26] The diffusion coefficient (or "diffusivity") describes the movement of a molecule through a medium and is dependent on molecular species, matrix properties, concentration, temperature and pressure. I want to expand the knowledge of intercellular chemical communication in healthy and diseased tissues by studying the diffusivity of tissue with novel microfluidic platforms and ex vivo tissue slices.

1.2.2 Lymph nodes as a model system to target for local delivery

Lymph nodes can be used as a model system for tissue hybrid chip development, because they are a highly organized with dynamic and complex responses to stimulation. Lymph nodes are a secondary organ of the immune system where the adaptive immune response develops thus protecting the organism from infections and diseases.[27] Lymphatics, the vessel component of the

immune system, drain in a unidirectional fashion into and through the lymph node, presenting antigens (potential activating motifs) and signaling proteins (chemokines and cytokines) to resident cells. The structure of the nodes is critical to coordinating an adaptive immune response and immune memory to a foreign antigen. The lymph node can be reduced into three major components: the outer cortex which contains B Cell follicles, a T cell zone or paracortex, and the medulla (Figure 1.2).[28] The structural backbone of the lymph node is made of fibroblastic reticular cells, which control the expansion of the lymph node during an immune response.[29] Lymph node structure is dynamic and changes to accommodate the development of an immune response, which is generally inflammatory in nature.[30–32] Little is known about the diffusion of proteins within the lymph node.[24,25] Understanding protein transport within the lymph node, especially in an inflamed state, will allow for more intelligently designed drug therapies and vaccines and give a better understanding of the lymph node.

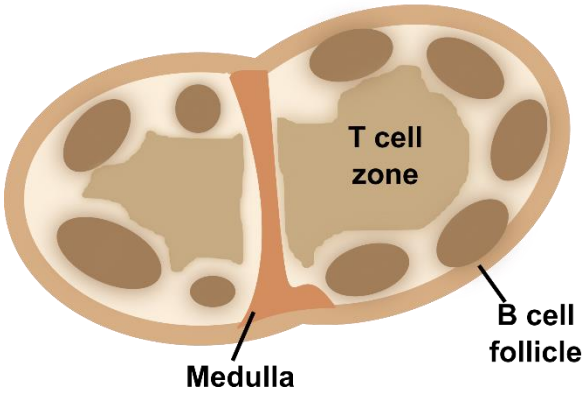

Figure 1.2 Schematic of lymph node with a B cell follicle, T cell zone and medulla labelled.

1.3 Different model systems for studying protein transport and responses in lymph nodes

Immunology has three approaches for studying lymph node tissue functions: in vivo, in vitro, and ex vivo. An in vivo model approach is one in which the experiment is performed in a living organism using imaging or electrochemical readouts. A common use for this model is seen in preclinical trials of drugs to assess any off-target effects.[33,34] The method retains the spatial organization, native fluid flow, and cell recruitment within tissues and their microenvironment. However, in vivo analysis is limited in its accessibility for experimental parameters such as precise stimulation of sub-structures, control stimulant concentration, and repeated temporally resolved

read-outs. Additionally, external imaging set-ups for in vivo models are complex and expensive, which might not be accessible for all labs. Due to the complexity of many experimental set-ups, it is difficult to achieve high experimental throughput.

The in vitro approach utilizes cell cultures to probe specific cell types and interactions as well as elucidate mechanisms behind cell behavior. Single or multiple cell types are grown or cultured in a well plate.[35] Cell cultures allow for more experimental flexibility in terms of precise control over the cellular environment, stimulation and time point analysis, with easily multiplexed experimental designs compatible with high throughput analyses. However, cell cultures lack the complexity and spatial organization of a tissue and can be too reductive of a model to be a true representation of physiological conditions.

The ex vivo approach is a middle ground alternative to the previous two approaches using tissue slices. Tissue slices were first developed in the field of neuroscience for brain tissue, specifically to study electro and biochemical stimulation of substructure within the brain.[36] Since then, the method has been used to study other organs i.e. pancreas, liver, heart, lung, and lymph node.[37–41] In this approach, the live tissue slices (300-400 μm thick) retain the organization and complexity of in vivo models, while combining the experimental accessibility of an in vitro cell culture.[41] Slices also allow for the stimulation of sub-structures within the tissue and, compared to in vivo models, a higher throughput potential with a reduction of animal use. I will be using this approach throughout the rest of the thesis to investigate tissue properties like diffusivity with microfluidic devices.

1.4 Microfluidic devices are a strategy for local delivery to tissue

1.4.1 Microfluidics are well suited for biological applications including tissue culture

Microfluidic devices are uniquely suited for tissue slice culture due to the highly controlled environment that can be generated in these devices.[6] Microfluidic devices offer an efficient way to deliver nutrients, remove waste, provide the ability for highly controlled chemical stimulation, and are compatible with modern imaging techniques.[25] Tissue slices have been cultured in microfluidics devices since the early 2000s, beginning with brain slices.[36] The first microfluidic devices used with tissue slices were designed to improve culture conditions of the tissues by improving oxygenation and exposure to nutrients from fluid flow.[42] Since then, the purpose of the microfluidic device has extended to enable stimulation and analytical readouts for a variety of tissues such as lymph nodes, tumors, gut, liver, and pancreatic islets to name a few.[7,43–47]

1.4.2 A brief history of microfluidics

The field of microfluidics refers to the manipulation and control of miniscule volumes of fluids (μL, 10^{-6} to pL,10^{-12}), within a network of channels housed in a device. These microfluidic channels range from micrometers to millimeters in dimension. Microfluidics developed from the electrical engineering field, when micro-electromechanical systems (MEMS) fabrication techniques and principles were applied to fluid-filled networks.[48] These very first microfluidic devices were fabricated on silicon wafers or etched into glass, and were used to perform chromatography.[49]

The catalyst for the rapid expansion in the microfluidics field was the development of soft-lithography spearheaded by the Whitesides group as a fabrication technique. Soft-lithography fabrication begins with photolithography, a process that uses light to make patterns in a photosensitive material to make a master mold on silicon wafers. The master molds are used to

make replicates in a soft rubber-like polymer, polydimethylsiloxane (PDMS), with the intended channels of the device.[50] The use of soft-lithography allowed researchers to quickly fabricate copies of a device from a single mold in a cheap, biocompatible material, that could be easily functionalized to bond with itself making enclosed channels easier to fabricate.[51] Major advancements in the field of microfluidics are due to innovations in fabrication methods to expediate the fabrication process and reduce the cost of the device.

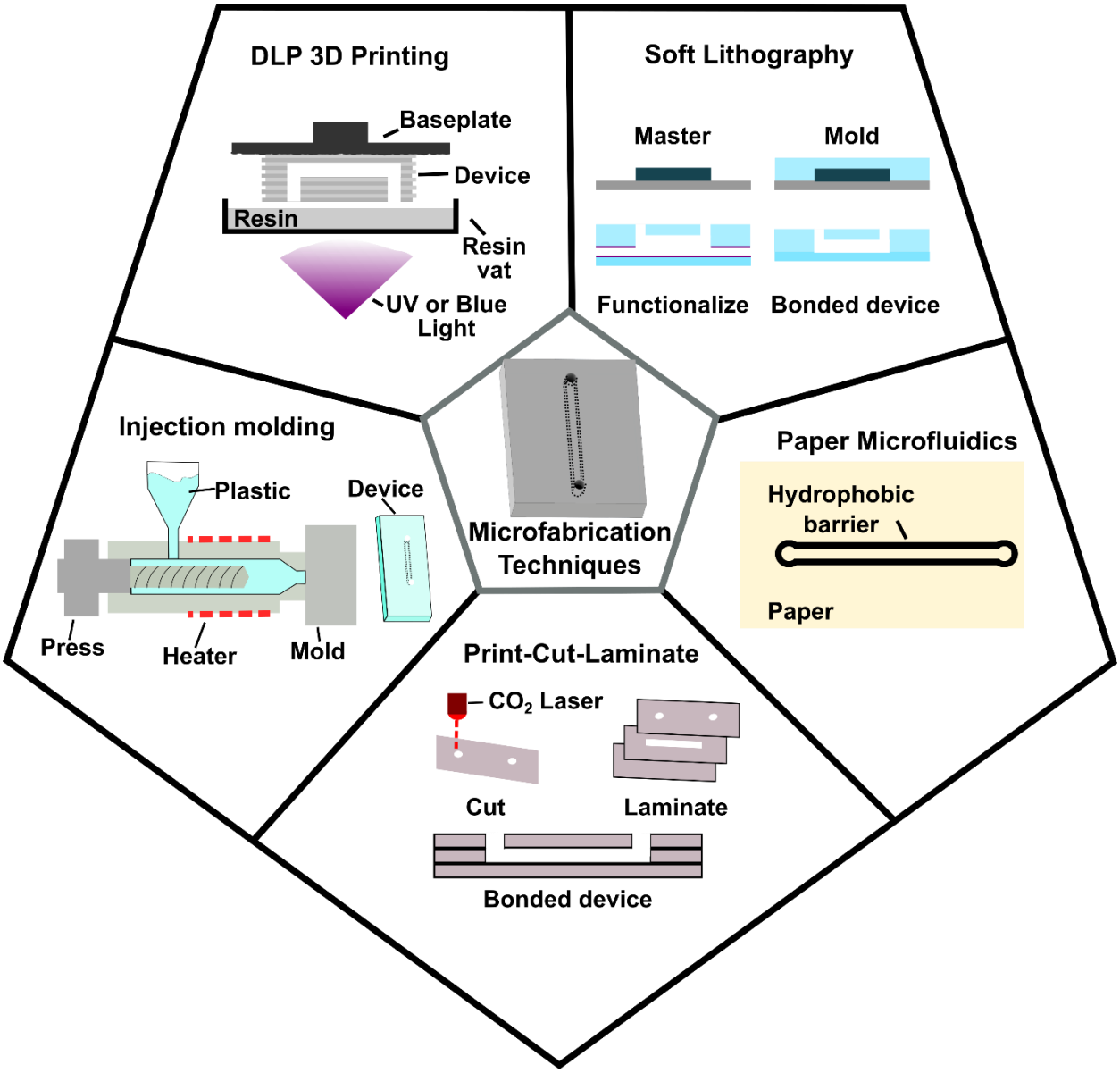

Figure 1.3 Various strategies for fabrication of microfluidic devices. Versions of soft lithography, print-cut-laminate, and DLP 3D printing strategies will be used in this thesis.

Since then, other methods of fabrication have diversified the field of microfluidics (Figure 1.3). The Whitesides group also the first to developed paper microfluidics, which uses self-wicking paper and hydrophobic barriers to fabricate self-pumping microchannels.[52] The Landers lab developed the print-cut-laminate method, which uses a laser etcher to cut thin materials, such as overhead transparencies, coated in printed adhesive, that are assembled and laminated to form a single chip.[53] Injection molding and hot embossing are microfluidic techniques with the largest potential for commercialization, since these methods mold thermoplastics with a high throughput to create cost-effective and reproducible microfluidic devices.[54] These two methods are not meant for rapid prototyping, but enable production at a larger scale of a finalized design. 3D printing is another innovation with the potential to transform the field of microfluidics. 3D printing is an additive method of fabrication that allows rapid prototyping of more complex geometry in a user-friendly single manufacturing step.[55] The resolution with 3D printing for microfluidic devices is currently in a sub-millimeter scale (0.5 -1 mm dimensions), but some printers have achieved truly microfluidic (< 100 μm) channel dimensions.[56]

1.4.3 Foundational physics necessary for microfluidics devices.

Liquids on a small scale, such as within a microfluidic device, behave differently than at a larger scale.[57] Specifically, the fluid dynamics are dominated by different forces at the microscale. Fluid flow can be described as turbulent or laminar. These terms differ by how possible is it to predict the position of a particle as a function of time. Turbulent flow is chaotic and unpredictable, with the fluid moving in irregular patterns which causes mixing. In contrast, laminar fluid flow moves in uniforms paths which leads to multiple fluids being able to move along parallel to one another without mixing.

The Reynolds number (Re) describes the flow regime, and is defined by the equation

$$Re = \frac{\rho v D_h}{\mu} \qquad \text{Equation 1.2,}$$

where ρ is the fluid density, ν is the fluid velocity, D_h is the hydraulic diameter, and μ is the fluid viscosity. The hydraulic diameter is determined by the cross-sectional geometry of the channel. A Re < 2300 is considered laminar flow, and Re increases as the flow becomes turbulent.[57] The cross-sectional geometry is typically small enough in the channels of most microfluidic devices that flow is generally laminar.

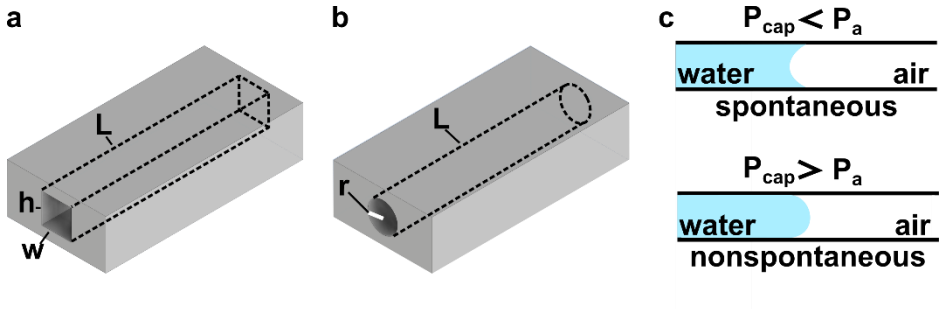

Figure 1.4 Schematic of relevant device dimensions and capillary pressure (a) A square channel with the width (w), height (h) and length (L) labeled. (b) A channel with a circular cross-section with the length (L) and radius (r) labelled. (c) An example schematic of a water and air system for both spontaneous and nonspontaneous flow.

The second equation that dominates fluid dynamics on a small scale (and large) is fluidic resistance:

$$Q = \Delta P / R \qquad \text{Equation 1.3,}$$

where Q is the flow rate, ΔP is the pressure drop across a channel, and R is the resistance in a channel. There are two common cross-sectional geometries in microfluidics, a rectangle and a circle. The resistance of a rectangular channel can be calculated from the equation,

$$R = \frac{12\mu L}{wh^3}\left[1 - \frac{h}{w}\left(\frac{192}{\pi^5}\tanh\left(\frac{\eta\pi w}{2h}\right)\right)\right]^{-1} \qquad \text{Equation 1.4,}$$

where L is length of the channel, w is width, and h is the height (Figure 1.4a). Equation 1.4 applies to microchannels with a low aspect ratio (w ≈ h), there is a simpler variation for rectangular channels with a high aspect ratio (w>>h or h<<w), but is not applicable for the devices discussed in this thesis. For the resistance for a circular channel can be calculated from the equation,

$$R = \frac{8\mu L}{\pi r^4} \quad \text{Equation 1.5,}$$

where r is the radius of the circle (Figure 1.4b). The resistance to flow is important for many calculations in microfluidics including understanding pressure drops across a system, ensuring equal flow down multiple channels, and passive fluidic valving.

Two-phase microfluidic devices are a specialized sub-field of microfluidics that uses two immiscible phases, witha wide range of applications including chemical reactions, material synthesis, PCR and cell culture.[58,59] These phases may flow parallel to one another or be used to form droplets.[58] Surface chemistry of the microfluidic device plays a critical role in the function of these devices, specifically the control over which surfaces are wet by each phase.[60] Capillary pressures is responsible for directing and controlling flow in some two-phase devices.[61,62] The Young-Laplace equation describes capillary pressure (P_{cap}),

$$\Delta P_{cap} = \gamma\kappa \quad \text{Equation 1.6,}$$

where γ is the interfacial tension and κ is the local mean curvature which is critical for spontaneous flow in a two-phase system. The relationship between capillary pressure and ambient pressure in a system determines if fluid flow will be spontaneous or nonspontaneous (Figure 1.4c).

1.4.4 Microfluidics devices can be used for local stimulation

Local stimulation with microfluidic devices has been achieved in a variety of ways. Some devices that have been used for localized delivery incorporate microfluidic channels and a permeable membrane to deliver hundreds microns wide stripes of analyte to the tissue.[47] This approach was used to multiplex drug screening in tumor tissues, but would not be appropriate for targeting circular substructures within a tissue. Another approach is to use device with channels that have ports on top of channels to deliver to a tissue situated above the port.[7,24,63] In this configuration, the user can stimulate sub-structures within a tissue from a point source, but alignment of the sub-structure of interest and the port is dependent on user-manipulation of the tissue. Excessive handling can lead to mechanical damage to the tissue. Another microfluidic device, called the chemistrode, can be positioned like an electrode and deliver in a push-pull manner.[64] This device was optimized for thin (10 μm) fixed tissue slices and single cell cultures and the push-pull mechanism may not be sufficient to deliver all the way through a thick live (300 μm) slice.[65,66] As such, it was determined that a microfluidic device that minimized user-handling of tissues slices and allowed for local point source delivery to live thick tissue slices was of interest to study spatiotemporally resolve events in tissue systems.

1.5 Research Goals and Concluding Remarks

In this work, I focused on developing and utilizing microfluidic devices for precise local delivery of chemicals to tissue slices using lymph node tissue as a model system. By utilizing this technology, we can begin to ask questions about the diffusivity of the tissue microenvironment in both healthy and diseased states. **Chapter 2** will focus on the application of a stationary local delivery device to a diseased tissue model. Lymph nodes from vaccination mice were used as a

model for inflammation. Diffusion coefficient and the tortuosity of the tissue were then measured in the inflamed tissue for the first time.

After identifying that tissue handling was an issue in the previous stationary local delivery device, a novel design was proposed and tested. These devices improve upon the previous static port technology by repositioning the delivery port beneath a slice protected in a culture chamber. In **Chapter 3,** a proof-of-concept movable microfluidic port device will be demonstrated highlighting the physics behind such a device. The movable microfluidic port device allows for repetitive sequential deliveries able to targe substructures (<200 μm) within a tissue slice, but the device involves a complex fabrication process.

In order to simplify the fabrication process and enable sharing of the technology with collaborators, a 3D printed fabrication method was explored. First, in **Chapter 4** the surface of photopolymerizing resins will be chemically modified to be selectively fluorophilic and hydrophobic, which is critical for two-phase microfluidic devices, such as the movable microfluidic port device that has both an aqueous and oil phase. Then, I demonstrate in C**hapter 5** digital light processing (DLP) printing as a method for movable-port device fabrication. Finally, I will conclude in C**hapter 6** with a discussion of impact of this type of technology and future applications.

1.6 References:

1. Pompano, R. R., Chiang, A. H., Kastrup, C. J. & Ismagilov, R. F. Conceptual and Experimental Tools to Understand Spatial Effects and Transport Phenomena in Nonlinear Biochemical Networks Illustrated with Patchy Switching. *Annu. Rev. Biochem.* **86**, 333–356 (2017).
2. Kim, J. Y., Kawabori, M. & Yenari, M. A. Innate inflammatory responses in stroke: mechanisms and potential therapeutic targets. *Curr. Med. Chem.* **21**, 2076–2097 (2014).

3. Bower, M. R., Stead, M., Meyer, F. B., Marsh, W. R. & Worrell, G. A. Spatiotemporal neuronal correlates of seizure generation in focal epilepsy. *Epilepsia* **53**, 807–816 (2012).
4. Kuba, K. Effects of catecholamines on the neuromuscular junction in the rat diaphragm. *J. Physiol.* **211**, 551–570 (1970).
5. Qi, H., Kastenmüller, W. & Germain, R. N. Spatiotemporal Basis of Innate and Adaptive Immunity in Secondary Lymphoid Tissue. *Annu. Rev. Cell Dev. Biol.* **30**, 141–167 (2014).
6. Huang, Y., Williams, J. C. & Johnson, S. M. Brain slice on a chip: opportunities and challenges of applying microfluidic technology to intact tissues. *Lab. Chip* **12**, 2103 (2012).
7. Ross, A. E., Belanger, M. C., Woodroof, J. F. & Pompano, R. R. Spatially resolved microfluidic stimulation of lymphoid tissue ex vivo. *The Analyst* **142**, 649–659 (2017).
8. Morgado, F. N., da Silva, A. V. A. & Porrozzi, R. Infectious Diseases and the Lymphoid Extracellular Matrix Remodeling: A Focus on Conduit System. *Cells* **9**, (2020).
9. Bissell, M. J., Hall, H. G. & Parry, G. How does the extracellular matrix direct gene expression? *J. Theor. Biol.* **99**, 31–68 (1982).
10. Vaday, G. G. & Lider, O. Extracellular matrix moieties, cytokines, and enzymes: dynamic effects on immune cell behavior and inflammation. *J. Leukoc. Biol.* **67**, 149–159 (2000).
11. Biga, L. M. *et al.* 4.1 Types of Tissues. in *Anatomy & Physiology* (OpenStax/Oregon State University, 2019).
12. Steinberg, M. S. Goal-directedness in embryonic development. *Integr. Biol. Issues News Rev.* **1**, 49–59 (1998).
13. Sainte-Marie, G., Peng, F.-S. & Bélisle, C. Overall architecture and pattern of lymph flow in the rat lymph node. *Am. J. Anat.* **164**, 275–309 (1982).

14. Hadamitzky, C. *et al.* Age-dependent histoarchitectural changes in human lymph nodes: an underestimated process with clinical relevance? *J. Anat.* **216**, 556–562 (2010).
15. Thompson, H. L., Smithey, M. J., Surh, C. D. & Nikolich-Žugich, J. Functional and Homeostatic Impact of Age-Related Changes in Lymph Node Stroma. *Front. Immunol.* **8**, (2017).
16. Frantz, C., Stewart, K. M. & Weaver, V. M. The extracellular matrix at a glance. *J. Cell Sci.* **123**, 4195–4200 (2010).
17. Strand, D. W., Franco, O. E., Basanta, D., Anderson, A. R. A. & Hayward, S. W. Perspectives on Tissue Interactions in Development and Disease. *Curr. Mol. Med.* **10**, 95–112 (2010).
18. Basoli, F. *et al.* Biomechanical Characterization at the Cell Scale: Present and Prospects. *Front. Physiol.* **9**, (2018).
19. Ruprecht, V. *et al.* How cells respond to environmental cues – insights from bio-functionalized substrates. *J. Cell Sci.* **130**, 51–61 (2017).
20. Ramesh, G., MacLean, A. G. & Philipp, M. T. Cytokines and Chemokines at the Crossroads of Neuroinflammation, Neurodegeneration, and Neuropathic Pain. *Mediators Inflamm.* **2013**, (2013).
21. Zhang, J.-M. & An, J. Cytokines, Inflammation and Pain. *Int. Anesthesiol. Clin.* **45**, 27–37 (2007).
22. Müller, P. & Schier, A. F. Extracellular movement of signaling molecules. *Dev. Cell* **21**, 145–158 (2011).
23. Nebyla, M., Přibyl, M. & Schreiber, I. Effects of Convective Transport on Chemical Signal Propagation in Epithelia. *Biophys. J.* **102**, 990–1000 (2012).

24. Ross, A. E. & Pompano, R. R. Diffusion of cytokines in live lymph node tissue using microfluidic integrated optical imaging. *Anal. Chim. Acta* **1000**, 205–213 (2018).
25. C, N. & S, H. Brain Extracellular Space: The Final Frontier of Neuroscience. *Biophys. J.* **113**, 2133–2142 (2017).
26. Berg, H. C. *Random Walks in Biology*. (Princeton University Press, 1993).
27. Charles A Janeway, J., Travers, P., Walport, M. & Shlomchik, M. J. The course of the adaptive response to infection. *Immunobiol. Immune Syst. Health Dis. 5th Ed.* (2001).
28. Willard-Mack, C. L. Normal structure, function, and histology of lymph nodes. *Toxicol Pathol* **34**, 409–424 (2006).
29. Tomei, A. A., Siegert, S., Britschgi, M. R., Luther, S. A. & Swartz, M. A. Fluid Flow Regulates Stromal Cell Organization and CCL21 Expression in a Tissue-Engineered Lymph Node Microenvironment. *J. Immunol.* **183**, 4273–4283 (2009).
30. Acton, S. E. & Reis e Sousa, C. Dendritic cells in remodeling of lymph nodes during immune responses. *Immunol. Rev.* **271**, 221–229 (2016).
31. Yang, C.-Y. *et al.* Trapping of naive lymphocytes triggers rapid growth and remodeling of the fibroblast network in reactive murine lymph nodes. *Proc. Natl. Acad. Sci.* **111**, E109–E118 (2014).
32. Gregory, J. L. *et al.* Infection Programs Sustained Lymphoid Stromal Cell Responses and Shapes Lymph Node Remodeling upon Secondary Challenge. *Cell Rep.* **18**, 406–418 (2017).
33. Mak, I. W., Evaniew, N. & Ghert, M. Lost in translation: animal models and clinical trials in cancer treatment. *Am. J. Transl. Res.* **6**, 114–118 (2014).
34. Liu, Y. *et al.* A Plasmonic Gold Nanostar Theranostic Probe for In Vivo Tumor Imaging and Photothermal Therapy. *Theranostics* **5**, 946–960 (2015).

35. Duval, K. *et al.* Modeling Physiological Events in 2D vs. 3D Cell Culture. *Physiology* **32**, 266–277 (2017).

36. Collingridge, G. L. The brain slice preparation: a tribute to the pioneer Henry McIlwain. *J. Neurosci. Methods* **59**, 5–9 (1995).

37. Marciniak, A. *et al.* Using pancreas tissue slices for in situ studies of islet of Langerhans and acinar cell biology. *Nat. Protoc.* **9**, 2809–2822 (2014).

38. Olinga, P. & Schuppan, D. Precision-cut liver slices: A tool to model the liver ex vivo. *J. Hepatol.* **58**, 1252–1253 (2013).

39. Wang, K. *et al.* Cardiac tissue slices: preparation, handling, and successful optical mapping. *Am. J. Physiol.-Heart Circ. Physiol.* **308**, H1112–H1125 (2015).

40. Henjakovic, M. *et al.* Ex vivo testing of immune responses in precision-cut lung slices. *Toxicol. Appl. Pharmacol.* **231**, 68–76 (2008).

41. Belanger, M. C. *et al.* Acute Lymph Node Slices Are a Functional Model System to Study Immunity Ex Vivo. *ACS Pharmacol. Transl. Sci.* **4**, 128–142 (2021).

42. Passeraub, Ph. A., Almeida, A. C. & Thakor, N. V. Design, Microfabrication and Analysis of a Microfluidic Chamber for the Perfusion of Brain Tissue Slices. *Biomed. Microdevices* **5**, 147–155 (2003).

43. van Midwoud, P. M., Merema, M. T., Verpoorte, E. & Groothuis, G. M. M. A microfluidic approach for in vitro assessment of interorgan interactions in drug metabolism using intestinal and liver slices. *Lab. Chip* **10**, 2778–2786 (2010).

44. L. Glieberman, A. *et al.* Synchronized stimulation and continuous insulin sensing in a microfluidic human Islet on a Chip designed for scalable manufacturing. *Lab. Chip* **19**, 2993–3010 (2019).

45. Queval, A. *et al.* Chamber and microfluidic probe for microperfusion of organotypic brain slices. *Lab. Chip* **10**, 326–334 (2010).
46. Richardson, A. *et al.* A microfluidic organotypic device for culture of mammalian intestines ex vivo. *Anal. Methods* **12**, 297–303 (2020).
47. Chang, T. C. *et al.* Parallel microfluidic chemosensitivity testing on individual slice cultures. *Lab Chip* **14**, 4540–4551 (2014).
48. Convery, N. & Gadegaard, N. 30 years of microfluidics. *Micro Nano Eng.* **2**, 76–91 (2019).
49. Manz, A., Graber, N. & Widmer, H. M. Miniaturized total chemical analysis systems: A novel concept for chemical sensing. *Sens. Actuators B Chem.* **1**, 244–248 (1990).
50. Duffy, D. C., McDonald, J. C., Schueller, O. J. A. & Whitesides, G. M. Rapid Prototyping of Microfluidic Systems in Poly(dimethylsiloxane). *Anal. Chem.* **70**, 4974–4984 (1998).
51. Morbioli, G. G., Speller, N. C. & Stockton, A. M. A practical guide to rapid-prototyping of PDMS-based microfluidic devices: A tutorial. *Anal. Chim. Acta* **1135**, 150–174 (2020).
52. Martinez, A. W., Phillips, S. T., Butte, M. J. & Whitesides, G. M. Patterned Paper as a Platform for Inexpensive, Low Volume, Portable Bioassays. *Angew. Chem. Int. Ed Engl.* **46**, 1318–1320 (2007).
53. Thompson, B. L. *et al.* Inexpensive, rapid prototyping of microfluidic devices using overhead transparencies and a laser print, cut and laminate fabrication method. *Nat. Protoc.* **10**, 875–886 (2015).
54. Gale, B. K. *et al.* A Review of Current Methods in Microfluidic Device Fabrication and Future Commercialization Prospects. *Inventions* **3**, 60 (2018).
55. Bhattacharjee, N., Urrios, A., Kang, S. & Folch, A. The upcoming 3D-printing revolution in microfluidics. *Lab. Chip* **16**, 1720–1742 (2016).

56. Beauchamp, M. J., Nordin, G. P. & Woolley, A. T. Moving from millifluidic to truly microfluidic sub-100-μm cross-section 3D printed devices. *Anal. Bioanal. Chem.* **409**, 4311–4319 (2017).

57. Beebe, D. J., Mensing, G. A. & Walker, G. M. Physics and applications of Microfluidics in biology. *Annu. Rev. Biomed. Eng.* **4**, 261–286 (2002).

58. Zhao, C.-X. & Middelberg, A. P. J. Two-phase microfluidic flows. *Chem. Eng. Sci.* **66**, 1394–1411 (2011).

59. Tsukamoto, M. *et al.* Cell separation by an aqueous two-phase system in a microfluidic device. *Analyst* **134**, 1994–1998 (2009).

60. Günther, A. & F. Jensen, K. Multiphase microfluidics: from flow characteristics to chemical and materials synthesis. *Lab. Chip* **6**, 1487–1503 (2006).

61. Hansang Cho, Ho-Young Kim, Ji Yoon Kang, & Tae Song Kim. How the capillary burst microvavle works. *J. Colloid Interface Sci.* **306**, 379–385 (2007).

62. Pompano, R. R., Platt, C. E., Karymov, M. A. & Ismagilov, R. F. Control of initiation, rate, and routing of spontaneous capillary-driven flow of liquid droplets through microfluidic channels on SlipChip. *Langmuir* **28**, 1931–1941 (2012).

63. Mohammed, J. S., Caicedo, H. H., Fall, C. P. & Eddington, D. T. Microfluidic add-on for standard electrophysiology chambers. *Lab. Chip* **8**, 1048–1055 (2008).

64. Chen, D. *et al.* The chemistrode: A droplet-based microfluidic device for stimulation and recording with high temporal, spatial, and chemical resolution. *Proc. Natl. Acad. Sci.* **105**, 16843–16848 (2008).

65. Lovchik, R. D., Kaigala, G. V., Georgiadis, M. & Delamarche, E. Micro-immunohistochemistry using a microfluidic probe. *Lab. Chip* **12**, 1040–1043 (2012).

66. Kashyap, A., Autebert, J., Delamarche, E. & Kaigala, G. V. Selective local lysis and sampling of live cells for nucleic acid analysis using a microfluidic probe. *Sci. Rep.* **6**, (2016).

Chapter 2: Diffusivity of immunized lymph node tissue measured with microfluidic integrated optical imaging.

2.1 Abstract:

Protein transport plays a key role in cellular communication and coordination during an immune response. Cytokines (signaling proteins) move through the lymph node via diffusion, a process not well understood in the context of immunity. Binding to the extracellular matrix, charge interactions, and tortuosity, a measure of physical hindrance, are all potential factors that impact the molecule diffusion. Using a microfluidic Integrated Optical Imaging system (microIOI), developed to measure the diffusion coefficients of proteins in live tissue, we were able to analyze protein diffusion following model vaccination with three different adjuvants, Alum, poly(I:C), and complete Freud's adjuvant (CFA). Adjuvants are the part of the vaccine that elicits the immune response. Cytokine-sized dextrans (3 and 10 kDa) were used as a nonbinding probe to determine how physical changes in lymph node tissue, impacted diffusivity. Diffusion coefficient were measured 1- and 4-days post-vaccination. On day 1, 10 kDa dextrans had a smaller diffusion coefficient than 3 kDa dextrans ($p < 0.0001$) as expected but there were no significant differences across adjuvants. On day 4, 3 kDa dextrans had significantly higher diffusion coefficients in the poly(I:C) and CFA conditions ($p < 0.001$ and $p < 0.05$, respectively) compared to Alum and PBS. Due to anti-TNFα antibodes role in immunotherapies, diffusion coefficients were also measured for an anti-TNFα antibod and its isotype control. There were no significant differences between diffusion coefficients of either antibody in the different adjuvant conditions. Understanding changes in transport during immune responses could lead to improved development of immunotherapies.

2.2 Introduction:

Diffusion plays a critical role in the biodistribution of proteins and drug therapeutics. Proteins control and direct the communication, response, and movement of a diverse array of cells within tissues.[1] In the lymph node, signaling proteins establish concentration gradients that are essential to tissue morphogenesis, chemotaxis, and trigging response pathways, such as inflammation.[2–6] Signaling proteins role in inflammation makes them potential targets for immunotherapies to treat a wide range of inflammatory autoimmune diseases.[7–10] Little is known about how these molecules diffuse through the lymph node.[11] Both signaling proteins and immunotherapies are subject to interstitial flow, diffusion, and binding events when traversing the complex extracellular matrix of the lymph node, making protein transport within the lymph node critical for controlling immune responses.[12] Previous work has measured cytokine diffusion coefficients and tortuosity within naïve lymph node tissue.[13] The impact of convective flow of immunotherapies in lymph node tissue has been studied, but the contribution of diffusion on immunotherapy transport has not been explored.[12] The spread of these molecules is dependent on tissue permeability and membrane surface area which may change drastically in an inflamed state of the lymph node.[14] It is currently unclear how diffusion of cytokines and chemokines would change in a lymph node during an immune response. We hypothesize that in order to design immunotherapy drugs intelligently, we must first understand protein transport in the lymph node during inflammatory immune responses. Though there are many mechanisms for protein transports, we focused solely understanding diffusion-based transport within the lymph node.

One of the first steps in an immune response is inflammation or swelling of the lymph node. During inflammation, the lymph node undergoes major structural rearrangement, has an influx of cells and is the location for cell activation.[15] One day after a triggered immune response, activation

markers (CD69) is upregulated on all lymphocytes.[16] 2-5 days post the initial activation event, inflammation of the node is apparent, with the structural stromal cell network stretching to accommodate the influx of cells to the lymph node.[17,18] The tortuosity in inflamed lymph nodes is currently unknown. We hypothesize that the massive rearrangement and swelling that lymph nodes undergo during an immune response could affect the tortuosity of the tissue, based on previous research in inflamed brain tissue.[19–21]

A common approach to study immune responses in mice is to use subcutaneous injections of adjuvants (an immune response activator) with a model antigen, such as ovalbumin (OVA), to mimic a vaccine.[22] Different adjuvants can elicit distinct mechanistic pathways for vaccine immunogenicity. Aluminum salts (Alum), and Complete Freund's adjuvant (CFA), a water-in-mineral oil emulsion that contains killed-mycobacteria, are adjuvants that create pro-inflammatory responses at the injection site by forming a depot that recruits innate immune cells that activate immune responses.[23] Poly(I:C) is a mimic of viral dsRNA that engages with Toll-like receptor 3, causing the induction of an immune response..[24] Poly(I:C) is a soluble adjuvant that diffuses directly to the lymph node from the site of injection. We anticipated a change in diffusivity as a result of increased swelling in the lymph node; however, prior research in inflamed brain tissue have demonstrated both increases and decreases in diffusivity depending on the specific situation.[25–28]

Here, we investigated how different adjuvant induced inflammatory responses in the lymph node impacted the diffusion of protein sized molecules using a microfluidic integrated optical imaging (microIOI) device in intact live tissue slices.[13] Using tissue slices preserves the necessary structural arrangements of cells while allowing substructures to be targeted.[29,30] First, we measured the diffusion coefficients of various sized dextrans, non-binding sugars, on day 1 and 4 post-

vaccination of mice and calculated the tortuosity of the immunized tissue. Then, we measured the diffusion coefficients of an immunotherapeutic (an infliximab bio-mimic) used to treat chronic inflammation diseases, and its isotype control in inflamed lymph nodes. Next, we are exploring ways to measure the extracellular space within the lymph node post-vaccination to correlate the results of the diffusion and tortuosity experiments with a physiological change.

2.3 Methods:

2.3.1 Device Fabrication

A Microfluidic Integrated Optical Imaging (micro-IOI) device was fabricated using polydimethylsiloxane (PDMS), molded using master molds made in a class 1,000 cleanroom, to form a single channel chip, as previously published.[13] PDMS was mixed at a 10:1 ratio of silicon elastomer base to curing agent (Ellsworth Adhesives, Germantown WI, USA). The device consisted of three layers. The top layer contained the inlet and outlet holes that served to hold the tubing (0.75 mm Weico Wire, Edgewood, NY) for delivery of labelled molecules. Holes for the inlet and outlet were punched with 0.75 mm tissue biopsy punch (World Precision Instruments, Sarasota FL, USA). The top layer also contains the tissue culture chamber punched with a 12-mm tissue biopsy punch. The middle layer is a laser etched 250 µm PDMS sheet (Stockwell Elastomerics, Inc, PA USA) that contains a delivery port in the middle of the channel. All layers are aligned visually and bonded using air plasma.

2.3.2 Animal work:

All animal work was approved by the Animal Care and Use Committee at the University of Virginia. Female C57BL/6 mice between 9-12 weeks of age (Jackson Laboratory, USA) were housed in a vivarium and given food and water ab libitum. Mice were vaccinated one or four days prior to experiments by subcutaneous injections of total volume of 200 µL dispersed between four

locations. Vaccinations consisted of 96 µg of OVA (Invivogen, San Diego, CA, USA > 98% purity) in solutions 1:1 (v/v) of 1 x phosphate buffered saline (PBS) (DPBS without calcium or magnesium (Lonza, Walkersville, MD, U.S.A.) with adjuvant (Alum 5 µg/mL, Poly(I:C) 0.5 mg/mL, CFA 0.5mg/mL, (Invivogen). For the vehicle control mice were injected with just 1x PBS and OVA.

2.3.3 Tissue slice collection

On the day of the experiments lymph node slices were collected as previously reported. [13,29,30] Briefly, the six peripheral lymph nodes were collected and embed in 6% agarose (Lonza, Walkersville MD, USA), then sliced 300 µm thick using a Leica VT1000S (Bannockburn, IL, USA) vibratome set to a speed of 90 and frequency of 3. Lymph nodes were sliced in cold 1x PBS and collected individually with a paint brush and were immediately placed in 37° C "complete media" (RPMI (Lonza, 16-167F) supplemented with 10% FBS (VWR, Seradigm USDA approved, 6 89510-186), 1× l-glutamine (Gibco Life Technologies, 25030-081), 50 U/mL Pen/Strep (Gibco), 50 µM beta-mercaptoethanol (Gibco, 21985-023), 1 mM sodium pyruvate (Hyclone, GE USA), 1× non-essential amino acids (Hyclone, SH30598.01), and 20 mM HEPES (VWR, 97064–362) and allowed to rest for 1 hour in a 37° incubator.

After an hour, the slices were immunostained with fluorescent rat anti-mouse/human B220/CD 45R using previously published methods (Biolegend, clone RA3-6B2).[31] The fluorescent tag attached to the B220 antibody varied depending on the fluorescent probes used for the delivery experiment.

2.3.4 Delivery and data collection

Prior to delivery, the MicroIOI device was placed on the stage of an upright microscope (Zeiss, Germany). Next, a 50-µL Hamilton syringe was used to fill the channel of the device with the

fluorescent-probe solution and then the outlet was plugged. For delivery, the tissue chamber was filled with 1x PBS. Lymph node slice was then placed into the chamber, and aligned so that the delivery port was under the area of interest for delivery. Area of interest was defined as being low B220 fluorescent intensity. A single image was taken prior to delivery, to correct for autofluorescence during analysis. The fluorescent solution was then delivered to the slice at 0.2 μL/min for 5 seconds. Fluorescently labeled neutral dextrans with various moleculars weights (3, 10, and 70 kDa dextrans, ThermoFisher) or fluorescently labelled anti-TNFα antibody and its isotype control (anti-TNFα clone: MP6-XT22 and isotype control: eBRG1, eBiosciences) were delivered to lymph node slices, Fluorescent labels were adjusted to accommodate multiple probes in each delivery. After delivery, the lymph node was imaged once every 30 seconds for 180 seconds as the fluorescent solution spread. Following the 180-second diffusion, the lymph node was removed, and the tissue chamber was washed with 1x PBS before repeating the imaging sequence.

2.3.5 Data analysis

For data analysis, a linescan was drawn across the lymph node region where delivery took place on the pre-delivery image and for diffusion monitoring images in Zeiss Zen 2 Lite software. Fluorescent intensities were then exported to Microsoft excel and the background autofluorescence was subtracted. These data were then fitted to a Gaussian distribution,

$$y = Ae^{-0.5(\frac{x}{\sigma})^2} \qquad \text{Equation 2.1,}$$

in Graphpad Prism 8, where A is the amplitude of the curve, x is the distance along the linescan (μm), and σ is the standard deviation of the Guassian curve. At this point, the strong fluorescent signal coming from the exit port was manually excluded by removal of the points directly over the

delivery port. The concentration distribution of 2-dimensional diffusion from a point source can be described by the equation,

$$C(r,t) = \frac{N}{4\pi DtL} e^{-\frac{r^2}{4Dt}} \qquad \text{Equation 2.2,}$$

where N is the number of moles of analyte released (mol), D is the diffusion coefficient ($\mu m^2/s$), t is the time (s), L is the length in the height of the tissue slice (300 μm), and r is the radial displacement of the molecule from the initial point source (μm). From the Gaussian fit, the standard deviation is related to the diffusion coefficient via the following relationship,

$$\sigma^2 = 2Dt \quad \text{Equation 2.3}$$

The diffusion coefficient was determined by finding the slope of the linear regression of $\frac{\sigma^2}{2} vs\ t$. All statistics were calculated using Graphpad Prism 8.

2.3.6 Tortuosity measurements

Tortuosity (λ) was calculated from the following equation:

$$\lambda = \sqrt{\frac{D}{D^*}} \qquad \text{Equation 2.4,}$$

where D is the free diffusion coefficient, and D* is the apparent diffusion coefficient measured in the lymph node tissue. As the equation implies, the larger the tortuosity value the more hindrance there is to the diffusion of a molecule in the extracellular matrix of the tissue. The free diffusion coefficients were measured using 0.3% agarose, to prevent residual convection from the delivery from interfering with the measurements.

2.3.7 Predictions of Free Diffusion coefficients

To predict the free diffusion coefficients of the dextrans and estimate the stokes radius of the antibodies, the Stokes-Einstein equation was used,

$$D = \frac{kT}{6\pi\eta R} \qquad \text{Equation 2.5 ,}$$

where D is the free diffusion coeffiecent, k is the Boltzmann constant (1.3 x10^{-16} g cm^2/s^2 K), T is the temperature (K), η is the solvent viscosity (0.0089 g/cm s for PBS at 25˚C, and R is the stokes radius (cm).

2.4 Results and Discussion:

2.4.1 Experimental design and set up

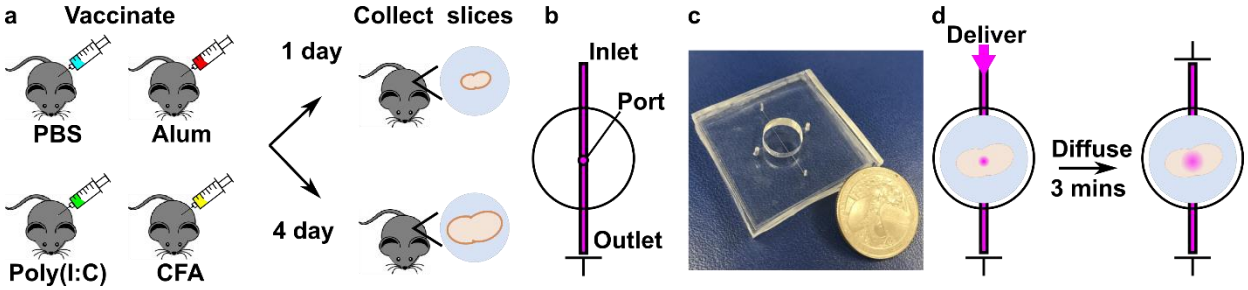

Figure 2.1 Overview of experimental design and the microIOI device. a) Mice were injected subcutaneously with ovalbumin (ova) and adjuvant (1x PBS (sham), Alum, Poly (I:C), or CFA) to induce inflammation in the nodes. After 1- or 4-days post- vaccination the lymph nodes were collected and sliced. Slices were then placed in a MicroIOI device (b) schematic of the device with a United States quarter for size reference and c) an image. d) A 5 second delivery of fluorescent macromolecules was stopped, and the macromolecules were allowed to diffuse for a period of 3 mins with images taken every 30 seconds.

To test the diffusivity of protein sized molecules in inflamed lymph node tissue, mice were first vaccinated with OVA and one of four different adjuvants: Alum, Poly(I:C), CFA, and PBS (sham adjuvant) (Figure 2.1a). The lymph nodes were collected and sliced either one- or four-days post vaccination (Figure 2.1a). Day 1 was chosen because it would be before lymph node expansion.[18] Poly(I:C) and other soluble factors would have reached the node within minutes to a

few hours,[16,23] initiating the immune response before the first time point. Day 4 was chosen to examine any changes in tissue diffusivity due to the node's expansion.[17]

The diffusivity and tortuosity of the inflamed lymph node were measured using a previously described microIOI device (Figure 2.1b and c)**.**[13] The microIOI device is a PDMS microfluidic device that houses a tissue slice in a culture chamber. Beneath the culture chamber is a microfluidic channel with a small (90 μm diameter) port that was used to delivery soluble analytes to the tissue in a short (3 second) pulse (Figure 2.1d). After the initial delivery, diffusion of the analytes was monitored by taking images every 30 secs for the next 3 mins, similar to well-established IOI methods used by Nicolson in the brain.[32,33] The microIOI technique is advantageous for studying sensitive tissues because it is a non-invasive delivery technique to sliced tissue.

2.4.2 Diffusivity of non-binding dextrans in immunized tissues

To distinguish any differences in the geometric properties of the extracellular space (ECS) in immunized tissue, we first measured the diffusion coefficients of non-binding molecules in vaccinated lymph node tissue. Starting with an inert, non-binding molecule demonstrates the movement through the tissue without the added complexity of binding interactions, allowing us to calculate the tortuosity of the lymph nodes.[20] Small molecular weight (3 and 10 kDa) and a larger 70 kDa dextrans were used as a non-binding molecule. The smaller dextrans stokes radius are similar in size to critical signaling protein called cytokines, that play a major role in immune responses in lymph nodes [13]. The larger 70 kDa dextran was chosen to mimic the stokes radius of more complex proteins like antibodies. First, we predicted and measured the free diffusion for all probes in a 0.3% agarose solution, to be able to calculate the tortuosity of the tissue (Table 2.1). For the non-binding dextrans, our predicted free diffusion coffiecients were in good agreement with our measured values.

Table 2.1 Free diffusion Coefficients Measurements were taken at 21 ˚C in 0.3% agarose (n=5). The error is the standard error of mean (SEM).

Probe	Stokes radius (nm)	Predicted D_{free} ($x10^{-7}cm^2/s$)	Measured D_{free} ($x10^{-7}cm^2/s$)
3 kDa	1.4 [a]	15	16 ± 0.09 (7)
10 kDa	2.3 [a]	9.6	8.1 ± 0.04 (7)
70 kDa	6.0 [a]	3.7	4.7 ± 0.03 (6)
Anti-TNFα	4.4 [b]	-	8.3 ± 1.0 (5)
isotype	3.0 [b]	-	5.5 ± 1.1 (5)

[a] *From reported stokes radius of the product sheet.*
[b] *Estimated from Equation 2.5*

Next, dextrans were local delivered to the T cell region (low B220 signal regions in immunostained lymph node slices) and diffusion was monitored using the microIOI device (Figure 2.2a). The apparent diffusion coefficients were measured for 3 and 10 kDa dextrans on day 1 post-vaccination (Figure 2.2b) in vaccinated lymph node tissue. When comparing the different dextrans, we observed the expected a difference due to the stokes radius of the dextrans (Table 2.1), as the smaller 3 kDa dextran was significantly faster ($p < 0.0001$) than the 10 kDa dextran (Figure 2.2b).

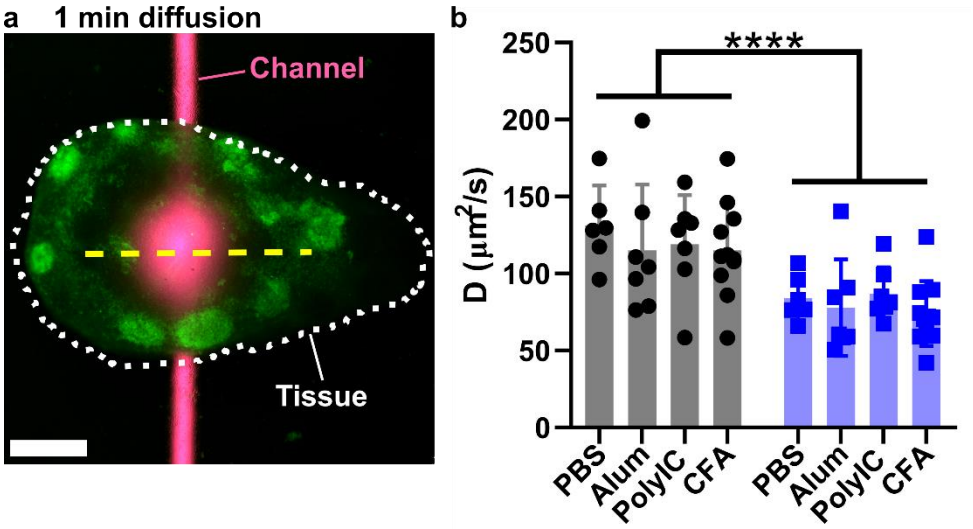

*Figure 2.2 An example delivery and Day 1 post-vaccination effective diffusion coeffiecents. An image of CFA immunized tissue slice day 4 (outlined in white) after delivery (a). The tissue was immunostained with anti-B220 for B cells (green) and a combination of 3 kDa dextran (labeled with Alexa Fluor 647) and 10 kDa dextran (labeled with rhodamine) was delivered to the slice (delivery magenta). The yellow dotted line is an example of the profile drawn across the delivery. Scale bar is 500 µm. b) Mean diffusion coefficients for both 3 kDa (black) and 10 kDa (blue) dextran. Error bars show Std. Dev. Each dot represents an individual lymph node slice, n=7. **** is a p-value <0.0001 between the different dextrans by 2-way ANOVA.*

When comparing the diffusion coefficients across the various vaccinated conditions, on day one there was no significant differences. We interpreted this to mean that none of the adjuvants had, mounted an immune response yet large enough to affect the diffusivity of the tissue at this time point.

We expected on day 4 post-vaccination that differences between adjuvant conditions would become apparent due to the inflammation of the lymph nodes. We delivered and measured the diffusion coefficients for all three dextrans (3, 10 and 70 kDa) to each of the vaccinated conditions and the PBS sham (Figure 2.3). The apparent diffusion coefficients for the 3 and 10 kDa dextrans in poly(I:C) vaccinated tissue slices were significantly greater than the PBS vehicle control and the Alum vaccinated slices as determined by a one-way ANOVA (Figure 2.3a and b). In CFA vaccinated slices, the effective diffusion coefficient for 3 and 10 kDa dextrans had a greater rate of diffusion, but the diffusion coefficient was not significantly greater than the PBS vehicle control and Alum condition. The effective diffusion coefficients for the 70 kDa dextran was not significantly different (faster or slower) in any of the vaccinated conditions compared to the vehicle

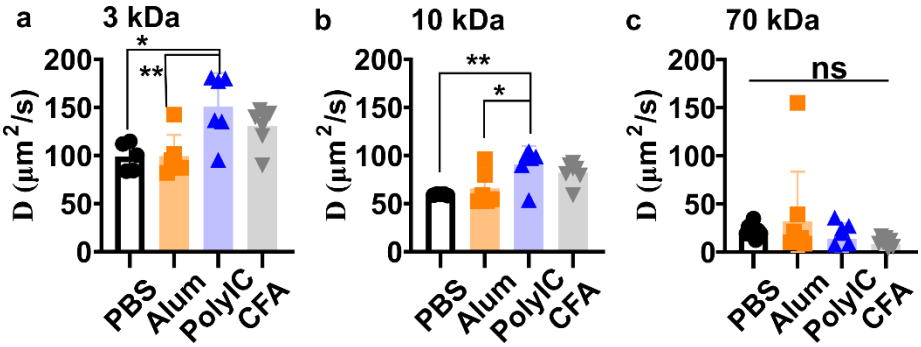

*Figure 2.3 The effective Diffusion coefficients of 3, 10 and 70 kDa dextrans on day 4 post vaccination. The mean diffusion coeffiecent for the different dextrans3 (a), 10 (b) and 70 kDa (c) in lymph node slices after immunization with various adjuvants (bars show mean ± Std dev, n=7). Each dot represents an individual lymph node slice. One-way ANOVA were used to compare the different adjuvant conditions for each dextran. * had a p value < 0.05 and ** had p-value < 0.01.*

control (Figure 2.3c). We interpret this to mean the steric hindrance of the larger dextran is greater than any changes to the extracellular space due to the vaccination of the mouse. Since the

difference between the small dextrans' apparent diffusion coefficients occurred on day 4, all subsequent measurements in this paper were done on day 4 post-vaccination.

2.4.3 Diffusivity of an anti-inflammatory immunotherapeutic in immunized tissues

Next, we tested a more complex molecule that had the potential to bind to sites within the tissue. Immunotherapies are a growing field of drugs used to treat a variety of diseases such as cancer and various autoimmune diseases. They have also been used to treat allergies and minimize the risk of tissue rejection in transplants. These drugs work by boosting or suppressing the patient's immune system.[34] One example of an immunotherapy is infliximab, which is an anti- TNF-α antibody that is used to treat Crohn's disease, rheumatoid arthritis and various other inflammatory autoimmune disease. The drug is given intravenously which means it has the potential to interact with the lymph node, and the biodistribution of a monoclonal antibody will affect the efficacy of the drug.[14] Apparent diffusion coefficients of immunotherapies have yet to be characterized in lymph nodes in both naïve and inflammatory states. We hypothesized that in an inflamed state of the tissue there would be more potential binding sites for an anti-inflammatory antibody. The binding of this molecule could further hinder the diffusion through tissue. Since the tissue were immunostained prior to diffusion measurements, we believe that this minimized off target binding

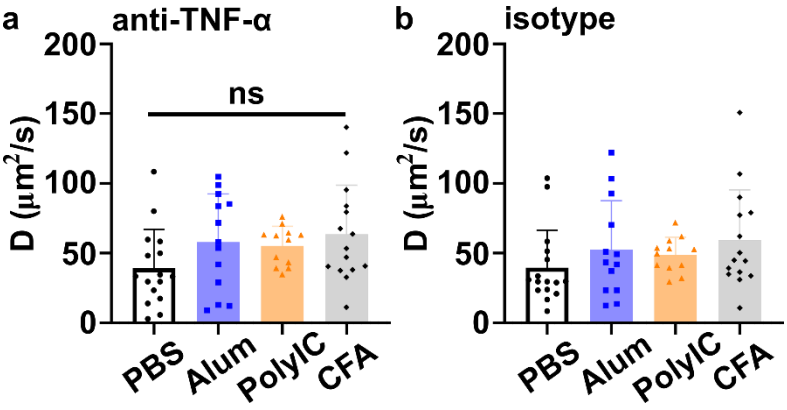

*Figure 2.4 The mean effective diffusion coefficients of two antibodies an antiTNF-α therapeutic antibody (a) and its isotype control (b). Error bars were Std dev. Each dot represents an individual lymph node slice, n=7. One-way ANOVA were used to compare the different adjuvant conditions for each dextran. * had a p value < 0.05 and ** had p-value < 0.01.*

of the antibody through FC-receptor mediated interactions as these receptors are blocked during the staining procedure.

We measured the apparent diffusion coefficient of an infliximab analog is MP6-XT22, a rat anti-murine TNF-α mAb infliximab and its isotype control (Figure 2.4).[35] The isotype control was a non-binding control that was used to determine if there was any hindered diffusion of the infliximab analog due to target binding. There was no significant difference between the apparent diffusion coefficients of the antibodies in any of the different adjuvant conditions. This agrees with the previous non-binding data where the larger 70 kDa dextran had no differences as well. This was probably due to the steric hinderance of the molecules being larger than any changes in the extracellular space induced by the adjuvant. There was also no apparent hindrance to diffusion due to binding effects, since there were no significant differences between the antibodies compared across the adjuvant conditions. This lack of hinderance might be due to a saturation of binding sites from the large concentration of antibodies delivered, which was necessary to visualize the diffusion in tissue. All apparent diffusion coefficients and tortuosity calculations were compiled in Table 2.2 below.

Table 2.2 Diffusion coefficients and Tortuosity calculations. Measurements were taken at 21 ˚C. The error is the standard error of mean, (n) were each sample is a different lymph node slice.

		Diffusion Coefficient ($x10^{-7}cm^2/s$)		Tortuosity[a]	
Adjuvant		**Day 1**	**Day 4**	**Day 1**	**Day 4**
PBS	**3 kDa**	13 ± 1.0 (5)	10 ± 0.7 (5)	1.1 ± 0.06	1.3 ± 0.06
	10 kDa	8 ± 0.6 (5)	6 ± 0.03 (5)	1.0 ± 0.04	1.2 ± 0.03
	70 kDa	-	3 ± 2.4 (8)	-	1.4 ± 0.1
	Anti-TNFα	-	4.4 ± 1.0 (18)	-	1.4 ± 0.18
	isotype	-	4.3 ± 0.7 (18)	-	1.2 ± 0.15
Alum	**3 kDa**	12 ± 2.0 (6)	10 ± 0.9 (6)	1.2 ± 0.09	1.3 ± 0.07
	10 kDa	8 ± 1 (6)	7 ± 0.7 (6)	1.0 ± 0.08	1.1 ± 0.07
	70 kDa	-	2 ± 0.2 (8)	-	1.2 ± 0.46
	Anti-TNFα	-	5.0 ± 1.1 (14)	-	1.3 ± 0.17
	isotype	-	5.3 ± 0.9 (14)	-	1.0 ± 0.13
Poly (I:C)	**3 kDa**	12 ± 1 (6)	15 ± 1.4 (6)	1.2 ± 0.08	1.0 ± 0.05
	10 kDa	9 ± 0.7 (6)	9 ± 0.7 (6)	1.0 ± 0.04	0.9 ± 0.04
	70 kDa	-	1 ± 0.7 (8)	-	2.3 ± 0.37
	Anti-TNFα	-	6.7 ± 1.9 (13)	-	1.1 ± 0.12
	isotype	-	5.9 ± 1.1 (13)	-	1.0 ± 0.13
CFA	**3 kDa**	12 ± 0.9 (7)	13 ± 0.8 (7)	1.2 ± 0.045	1.1 ± 0.05
	10 kDa	7 ± 0.6 (7)	8 ± 0.4 (7)	1.0 ± 0.05	1.0 ± 0.03
	70 kDa	-	0.8 ± 0.2 (8)	-	1.8 ± 0.51
	Anti-TNFα	-	8.8 ± 1.9 (17)	-	1.0 ±0.12
	isotype	-	8.8 ± 2.1 (17)	-	0.8 ± 0.13

[a] *Tortuosity was calculated using Equation 2.4*

2.4.4 Tortuosity of immunized tissue and area inflamed node

We hypothesized that an inflammatory response would correspond with a change in hindrance, which would have reflected in the tortuosity of the tissue. Tortuosity describes the structure of a porous matrix, which can be applied to the extracellular space in tissue. Here, we use tortuosity to describe the extracellular space of lymph node tissue vaccinated with the different adjuvants and vehicle control. Table 2.2 reports the tortuosity of the different dextrans measured for the different adjuvant conditions on the different days. Both the poly(I:C) and CFA vaccinated mice exhibited a lower tortuosity than the vehicle control or alum. The tortuosity of tissue vaccinated with poly(I:C) was significantly ($P<0.05$) lower than the vehicle control for both dextrans (3 and 10 kDa) on day 4 (Table 2.2). The decrease in tortuosity lead to the hypothesis that poly(I:C) and CFA would elicit a stronger inflammatory immune response from the lymph nodes compared to Alum and the vehicle control, which could be seen in the enlargement of the whole organ. To investigate if CFA and poly(I:C) elicits a stronger inflammatory response than the alum and the vehicle control, we measured the area of vaccinated lymph nodes (Figure 2.5). There was a significant increase in size when comparing any of the adjuvant conditions to the vehicle control, but there were no significant differences between the different adjuvant conditions.

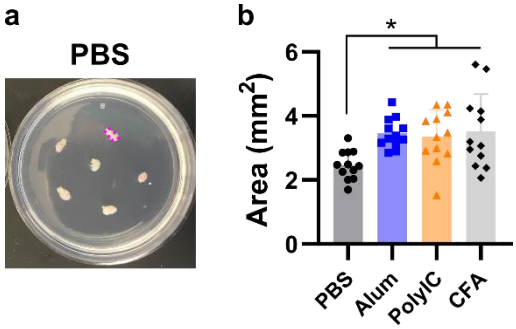

*Figure 2.5: Area of lymph nodes after vaccination. (a) Lymph nodes embedded in agarose and (b) the area of the embedded nodes for the various adjuvant conditions (mean± Std dev, n=12). One-way ANOVA, turkey's multiple comparison, * p <0.05.*

2.5 Proposed work:

2.5.1 Repeating diffusivity experiments at 37˚C

The first step in completing this work is to repeat these experiments at 37˚C (physiological temperature). All the data collected so far has been at room temperature, but it would be more useful for the field to provide data that was collected at 37˚C to better mimic in vivo conditions. While the trends observed at room temperature were intriguing, we must verify that the trends hold when the tissue is at a physiological temperature. This can be accomplished by degassing the device and analyte solution prior to running the experiment on a benchtop incubator. Interestingly, when comparing diffusion coefficients for 10 kDa dextrans in naive mice measured on the same day, we found that the measured diffusion coefficient at 37˚C (1.1 x10^7 cm^2/s) was slower than the diffusion coefficient measured at room temperature (7.5 x10^7 cm^2/s) (Table 2.3). We had hypothesized that the behavior of the diffusion in tissue might differ from free diffusion expectations which would have had the diffusion coefficient increase with temperature. We thought that hinderance events in the tissue may be larger than any temperature effects on the rate of diffusion, but did not expect that diffusion would actually decrease when the tissue was at physiological temperature. One potential explanation is that the stromal network, the structural backbone of the lymph node which accommodates the massive rearrangement during an immune response, was affected by temperature in the tissue, the contraction or relaxation of the network may affect the extracellular space within the tissue. This question about the state of the stromal network brings us to another set of experiments that would strengthen the work.

Table 2.3 Diffusion coefficients measured for 10 kDa dextran in naïve tissue (n=9). The error is the standard error of mean (SEM).

	Temp (˚C)	D_{eff} (x10^7 m^2/s)
Literature[13]	37	6.7 ± 2
Measured	35.5	1.1 ± 3.9
	21	7.5 ± 4

2.5.2 Directly measuring the extracellular space of a live lymph node slice.

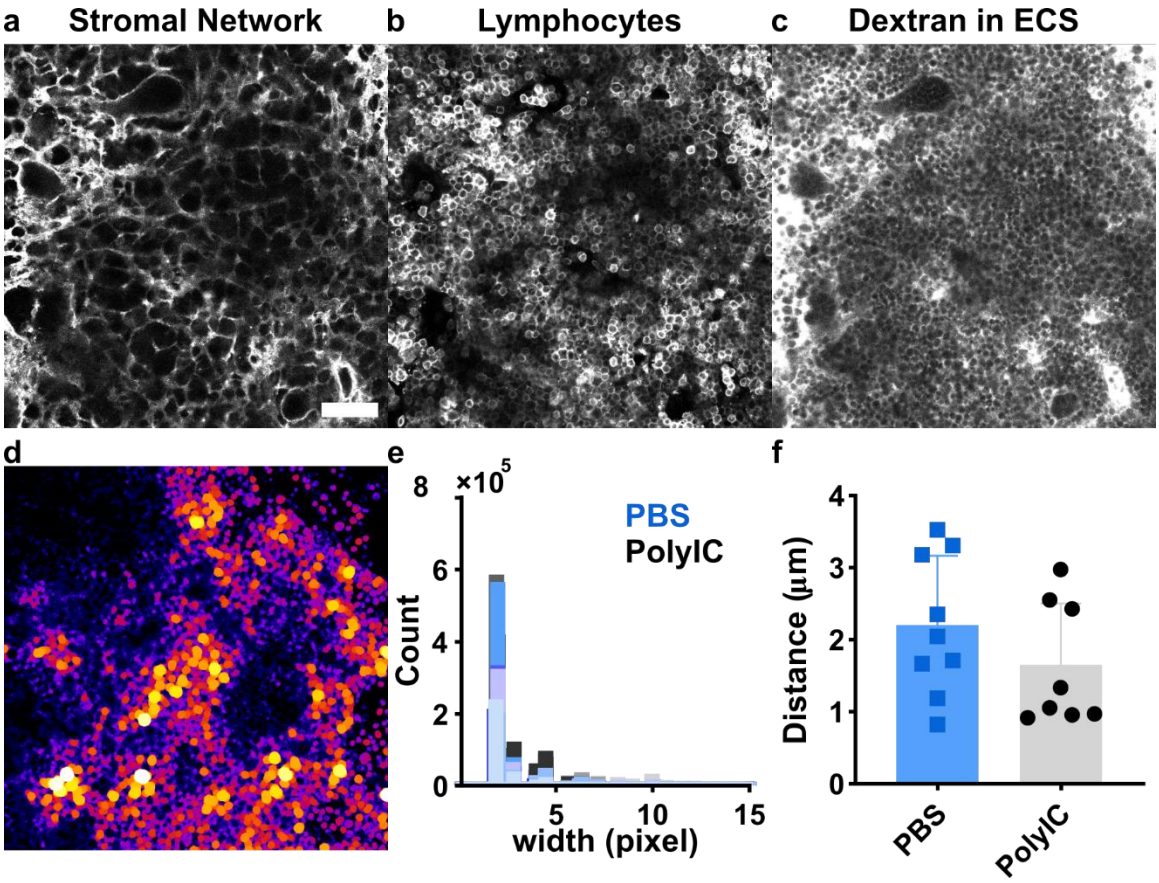

Figure 2.6 Visualizing the extracellular space in lymph nodes. Confocal images of a naïve lymph node immunostained with anti-podoplanin to mark the stromal network (a), and anti-CD 45 to outline lymphocytes (b). The tissue slice was soaked FITC labeled 150 kDa dextran visualize the extracellular space (c). Scale bar for all images is 50 µm. d) An example heat map result of the image processing on a slice that was vaccinated with poly(I:C). e) The histogram of widths across images of slices vaccinated with poly(I:C) and a vehicle control (PBS) and (f) the resulting widths from the histogram (mean ± Std dev, n=8). The mean widths are not significantly different between the mice vaccinated with poly(I:C) and a sham, unpaired t-test p>0.05.

Currently, it is not trivial to directly measure the extracellular space (ECS) of a live tissue slice. The conventional way to express the extracellular space is to use a volume fraction (α),

$$\alpha = Vecs/Vtotal \quad \text{Equation 2.6,}$$

which is the volume of the tissue (Vtotal) containing the volume of the ECS (Vecs).[36] This holistic approach to the extracellular space may not express minute changes differ across various regions in a tissue. Fixed slices have been used to measure the extra cellular space in tissues, but common

fixation methods cause the extracellular space to shrink.[37,38] As such, a new method that measures the ECS in live ex vivo tissue slices with confocal microscopy will be advantageous to understanding diffusion in tissues. To visualize the extra cellular space, large (70 and 150 kDa) dextrans that are excluded from cells but able to freely diffuse without the hindrance of binding events have been piloted as a probe for confocal microscopy ECS imaging. Confocal microscopy is able to achieve higher resolution images compared to widefield microcopy, enough to visualize individual cells (Figure 2.6a and b). The large dextran probe can also be seen excluded from the cells using confocal microscopy (Figure 2.6c), but characterizing the mean widths between cells requires more complex image analysis as it is not practical to try and manually measure the widths between cells.

One approach attempted to quantify the widths of the ECS across the whole image was to use local radial distances. Sequentially across a thresholded image, circles were fit within the fluorescent area. The diameters of the circles were the width of the ECS at that location in the image (Figure 2.6d). Theses widths were binned and counted to find the average width in the image (Figure 2.6e and f). The current threshold method is insufficient and a program is needed to be able to intelligently threshold an image by setting up local thresholds to highlight the signal from the extracellular space that may not be uniformly bright across the image. One potential limitation of this technology is that spaces below a certain width may be below the limit of detection in the microscope. Additionally, the large probe may be excluded from smaller spaces within the tissue. The probe can be adjusted to a smaller dextran that is still excluded from cells.

Similarly, visualizing the relaxation of the stromal network can give insights into the adjuvant dependent changes in diffusivity of the tissue. The stromal network in the lymph node is comprised of fibroblastic reticular cells (FRC) that control the expansion of the node through their

relaxation state.[15,39] This phenomenon has already been demonstrated by the Acton lab to be measurable in lymph nodes after vaccination with Alum.[15] It would be interesting to see if there was a difference in the expansion of this network after vaccination with different adjuvants. Using confocal images, we can use a program similar to the one described for the extracellular space to determine the area between labelled FRCs.

2.6 Conclusions:

Here, we measured the diffusivity and tortuosity of inflamed lymph node tissue using a microIOI technique. These results indicate that there might be an adjuvant dependent changes to the diffusivity of the tissue. Work still needs to be done to verify that these trends hold when the diffusion is measured at physiological temperatures and to give a biological explanation for the phenomenon. One method that is under development would be a method to visualize the extracellular space in live ex vivo tissue, which would be a powerful technique applicable to different tissues types. Understanding changes in transport of signaling molecules during an inflammation response could lead to improved design and development of immunotherapies.

2.7 References:

1. Turner, M. D., Nedjai, B., Hurst, T. & Pennington, D. J. Cytokines and chemokines: At the crossroads of cell signalling and inflammatory disease. *Biochim. Biophys. Acta BBA - Mol. Cell Res.* **1843**, 2563–2582 (2014).
2. Lander, A. D. How Cells Know Where They Are. *Science* **339**, 923–927 (2013).
3. Christian, J. L. Morphogen gradients in development: from form to function: Morphogen gradients in development: from form to function. *Wiley Interdiscip. Rev. Dev. Biol.* **1**, 3–15 (2012).

4. Wiig, H. & Swartz, M. A. Interstitial Fluid and Lymph Formation and Transport: Physiological Regulation and Roles in Inflammation and Cancer. *Physiol. Rev.* **92**, 1005–1060 (2012).
5. Pompano, R. R., Chiang, A. H., Kastrup, C. J. & Ismagilov, R. F. Conceptual and Experimental Tools to Understand Spatial Effects and Transport Phenomena in Nonlinear Biochemical Networks Illustrated with Patchy Switching. *Annu. Rev. Biochem.* **86**, 333–356 (2017).
6. Jin, T., Xu, X. & Hereld, D. Chemotaxis, chemokine receptors and human disease. *Cytokine* **44**, 1–8 (2008).
7. Victor, F. C., Gottlieb, A. B. & Menter, A. Changing paradigms in dermatology: tumor necrosis factor alpha (tnf-α) blockade in psoriasis and psoriatic arthritis. *Clin. Dermatol.* **21**, 392–397 (2003).
8. Taylor, P. C., Williams, R. O. & Maini, R. N. Immunotherapy for rheumatoid arthritis. *Curr. Opin. Immunol.* **13**, 611–616 (2001).
9. Hu-Lieskovan, S., Robert, L., Homet Moreno, B. & Ribas, A. Combining Targeted Therapy With Immunotherapy in BRAF-Mutant Melanoma: Promise and Challenges. *J. Clin. Oncol.* **32**, 2248–2254 (2014).
10. Feldmann, M. & Steinman, L. Design of effective immunotherapy for human autoimmunity. *Nature* **435**, 612–619 (2005).
11. Perona-Wright, G., Mohrs, K. & Mohrs, M. Sustained signaling by canonical helper T cell cytokines throughout the reactive lymph node. *Nat. Immunol.* **11**, 520–526 (2010).
12. Thomas, S. N., Rohner, N. A. & Edwards, E. E. Implications of Lymphatic Transport to Lymph Nodes in Immunity and Immunotherapy. *Annu. Rev. Biomed. Eng.* **18**, 207–233 (2016).

13. Ross, A. E. & Pompano, R. R. Diffusion of cytokines in live lymph node tissue using microfluidic integrated optical imaging. *Anal. Chim. Acta* **1000**, 205–213 (2018).
14. Tabrizi, M., Bornstein, G. G. & Suria, H. Biodistribution mechanisms of therapeutic monoclonal antibodies in health and disease. *AAPS J.* **12**, 33–43 (2010).
15. Martinez, V. G. *et al.* Fibroblastic Reticular Cells Control Conduit Matrix Deposition during Lymph Node Expansion. *Cell Rep.* **29**, 2810-2822.e5 (2019).
16. Hutchison, S. *et al.* Antigen depot is not required for alum adjuvanticity. *FASEB J.* **26**, 1272–1279 (2012).
17. Acton, S. E. & Reis e Sousa, C. Dendritic cells in remodeling of lymph nodes during immune responses. *Immunol. Rev.* **271**, 221–229 (2016).
18. Khan, Z. *et al.* Slow CCL2-dependent translocation of biopersistent particles from muscle to brain. *BMC Med.* **11**, 99 (2013).
19. SHERPA, A. D., VAN DE NES, P., XIAO, F., WEEDON, J. & HRABETOVA, S. Gliotoxin-induced swelling of astrocytes hinders diffusion in brain extracellular space via formation of dead-space microdomains. *Glia* **62**, 1053–1065 (2014).
20. Syková, E. & Nicholson, C. Diffusion in Brain Extracellular Space. *Physiol. Rev.* **88**, 1277–1340 (2008).
21. Hrabětová, S. & Nicholson, C. Dextran Decreases Extracellular Tortuosity in Thick-Slice Ischemia Model. *J. Cereb. Blood Flow Metab.* **20**, 1306–1310 (2000).
22. Clem, A. Fundamentals of vaccine immunology. *J. Glob. Infect. Dis.* **3**, 73 (2011).
23. Apostólico, J. de S., Lunardelli, V. A. S., Coirada, F. C., Boscardin, S. B. & Rosa, D. S. Adjuvants: Classification, Modus Operandi, and Licensing. *J. Immunol. Res.* **2016**, (2016).

24. Ngoi, S. M., Tovey, M. G. & Vella, A. T. Targeting Poly I:C to the TLR3-independent pathway boosts effector CD8 T cell differentiation through IFNα/β. *J. Immunol. Baltim. Md 1950* **181**, 7670–7680 (2008).

25. Nicholson, C. & Syková, E. Extracellular space structure revealed by diffusion analysis. *Trends Neurosci.* **21**, 207–215 (1998).

26. Bihan, D. L. *et al.* Diffusion tensor imaging: Concepts and applications. *J. Magn. Reson. Imaging* **13**, 534–546 (2001).

27. Barzó, P., Marmarou, A., Fatouros, P., Hayasaki, K. & Corwin, F. Contribution of vasogenic and cellular edema to traumatic brain swelling measured by diffusion-weighted imaging. *J. Neurosurg.* **87**, 900–907 (1997).

28. Schwartz, R. B., Mulkern, R. V., Gudbjartsson, H. & Jolesz, F. Diffusion-weighted MR imaging in hypertensive encephalopathy: clues to pathogenesis. *AJNR Am. J. Neuroradiol.* **19**, 859–862 (1998).

29. Belanger, M. C. *et al. Acute lymph node slices are a functional model system to study immunity ex vivo*. http://biorxiv.org/lookup/doi/10.1101/865543 (2019) doi:10.1101/865543.

30. Ross, A. E., Belanger, M. C., Woodroof, J. F. & Pompano, R. R. Spatially resolved microfluidic stimulation of lymphoid tissue ex vivo. *The Analyst* **142**, 649–659 (2017).

31. Groff, B. D., Kinman, A. W. L., Woodroof, J. F. & Pompano, R. R. Immunofluorescence staining of live lymph node tissue slices. *J. Immunol. Methods* **464**, 119–125 (2019).

32. Nicholson, C. & Tao, L. Hindered diffusion of high molecular weight compounds in brain extracellular microenvironment measured with integrative optical imaging. *Biophys. J.* **65**, 2277–2290 (1993).

33. Thorne, R. G. & Nicholson, C. In vivo diffusion analysis with quantum dots and dextrans predicts the width of brain extracellular space. *Proc. Natl. Acad. Sci.* **103**, 5567–5572 (2006).
34. Immunotherapies for autoimmune diseases. *Nat. Biomed. Eng.* **3**, 247–247 (2019).
35. Filler, S. G. *et al.* Pharmacokinetics of Murine p75-Fc Fusion Protein and MP6-XT22 Anti-Murine TNF-α mAb in Mice. *J. Investig. Dermatol. Symp. Proc.* **12**, 52–56 (2007).
36. C, N. & S, H. Brain Extracellular Space: The Final Frontier of Neuroscience. *Biophys. J.* **113**, 2133–2142 (2017).
37. Cragg, B. Overcoming the failure of electronmicroscopy to preserve the brain's extracellular space. *Trends Neurosci.* **2**, 159–161 (1979).
38. Korogod, N., Petersen, C. C. & Knott, G. W. Ultrastructural analysis of adult mouse neocortex comparing aldehyde perfusion with cryo fixation. *eLife* **4**, e05793 (2015).
39. Brown, F. D. & Turley, S. J. Fibroblastic Reticular Cells: Organization and Regulation of the T Lymphocyte Life Cycle. *J. Immunol. Baltim. Md 1950* **194**, 1389–1394 (2015).

Chapter 3: User-defined local stimulation of live tissue through a movable microfluidic port

Adapted From:
Catterton, M. A., Dunn, A. F. & Pompano, R. R. Lab. Chip 18, 2003–2012 (2018).

3.1 Abstract

Many *in vivo* tissue responses begin locally, yet most *in vitro* stimuli are delivered globally. Microfluidics has a unique ability to provide focal stimulation to tissue samples with precise control over fluid location, flow rate, and composition. However, previous devices utilizing fixed ports beneath the tissue required manual alignment of the tissue over the ports, increasing the risk of mechanical damage. Here we present a novel microfluidic device that allows the user to define the location of fluid delivery to a living tissue slice without manipulating the tissue itself. The device utilized a two-component SlipChip design to create a mobile port beneath the tissue slice. A culture chamber perforated by an array of ports housed a tissue slice and was separated by a layer of fluorocarbon oil from a single delivery port, fed by a microfluidic channel in the movable layer below. We derived and validated a physical model, based on interfacial tension and flow resistance, to predict the conditions under which fluid delivery occurred without leakage into the gap between layers. Aqueous solution was delivered reproducibly to samples of tissue and gel, and the width of the delivery region was controlled primarily by convection. Tissue slice viability was not affected by stimulation on the device. As a proof-of-principle, we showed that live slices of lymph node tissue could be sequentially targeted for precise stimulation. In the future this device may serve as a platform to study the effects of fluid flow in tissues and to perform local drug screening.

3.2 Introduction

Microfluidic platforms that chemically stimulate tissue *ex vivo* are a promising tool to mimic the local events that occur *in vivo*.[1,2] Cells in tissue are highly organized and use secreted signals such as small molecules, and proteins to communicate with one another and coordinate the functions of the tissue.[3–6] Many *in vivo* responses start from a local event that produces a focal source of soluble signals, including blood clotting after local vessel injury and neutrophil swarming after local tissue damage.[7–9] In order to better understand cellular communication in a structured tissue, it is useful to have an *ex vivo* platform to reproduce local stimulation on demand. Microfluidic devices can deliver chemical stimuli to substructures a few hundred microns in diameter in order to reveal how local responses initiate and propagate outward into the surrounding tissue.[10–18] Such tools have been developed and tested for use with living samples of brain, tumor, and lymph node. These tools may enable a better understanding of cell-cell communication and the physical properties of various tissues, to enhance mechanistic models of health and disease.

Ideally, a microfluidic device for local stimulation of live tissue would minimize the handling required of fragile tissue, allow delivery anywhere in the sample and, for thick tissue slices, deliver to the core of the tissue. Tissue slices for live culture are often 300 – 400 μm thick, and the damage from slicing may extend 10 – 100 μm deep, depending on the type of tissue.[19,20] Available microfluidic devices can be generally categorized as featuring either stationary ports or a movable push-pull probe. In the stationary port design, microchannels connected to a layer of ports or a membrane deliver fluid locally to a tissue sample.[10–14] To access a particular region, the tissue slice is manipulated over the port(s), which may increase the risk of mechanical damage, particularly if repositioning is required. Since the ports are found in predetermined locations, these devices cannot always accommodate the significant variability of size and morphology between slice

samples. Alternatively, probe-like microfluidic devices for local push-pull delivery allow the user to reposition the device instead of the tissue slice.[15–18,21] Push-pull delivery has been optimized for cell cultures and thin fixed tissue (typically 10 μm thick);[22,23] it is likely that fluid flow may not perfuse through the depth of a thick tissue slice. Therefore, in order to enable flexible stimulation of thick tissue slices, a device that combines both the mobility of a push-pull probe and the deep fluid penetration of an underlying port device is needed.

To achieve this goal, we adapted reconfigurable SlipChip technology and modified it for continuous fluid flow. A SlipChip is a two-phase microfluidic device, typically with two opposing plates (i.e. top and bottom) containing aqueous droplets in their channels and wells.[24] A thin oil layer is sandwiched between the two plates to prevent leakage while the movement of the plates relative to one another provides on-demand rearrangement of fluidic pathways. SlipChips have been used to perform chemical assays, PCR, and culture of both bacterial and mammalian cells,[25–28] but challenges remain for use with live tissue samples. While most SlipChips are explicitly designed to avoid the use of external pumps,[29,30] continuous local stimulation of tissue requires the use of pump-driven flow for uninterrupted fluid delivery. Furthermore, though most SlipChips consist of two layers,[24,26,28–30] most port-based local stimulation devices require at least three layers (microchannel layer, port layer, culture chamber layer).[10,12–14,31]

This paper presents the first self-contained microfluidic device with a movable port for tissue stimulation. We describe the design and fabrication of a prototype multi-layer device and describe the physical parameters needed to constrain pump-driven flow to the desired port. The robustness and resolution of local delivery were investigated under a range of biologically relevant flow rates. Finally, we demonstrated local delivery to multiple locations in a live lymph node slice without manual alignment of the slice.

3.3 Methods

3.3.1 Device Fabrication

The device was designed using AutoCad LT 2015. The delivery component was fabricated from 4 layers: a glass backing layer, a PDMS layer containing a 100-µm by 100-µm channel, an acrylic layer containing a 90-µm inner diameter delivery port, and a PDMS inlet. The backing layer, a 2 inch x 2 inch x 1.5 mm unpatterned glass slide (VWR, Radnor, PA USA), provided mechanical support for the device. The PDMS channel and inlet layers were fabricated using standard soft-lithography procedures.[32] Briefly, a transparency mask was created in AutoCAD, and printed at 20,000 DPI by CAD/Art Services, Inc (Brandon, OR). Master molds were fabricated in a Class 1000 clean room, using photolithography of SU-8 3050 photoresist (Microchem, Westborough MA, USA) on 3" silicon wafers (University Wafer, South Boston MA, USA). The channel layer and inlet replicas were made of polydimethylsiloxane using a 5:1 ratio of silicon elastomer base to curing agent (Slygard 184 Silicone Elastomer, Ellsworth Adhesives, Germantown WI, USA). The channel inlet was punched with a 0.75-mm I.D. tissue punch (World Precision Instruments, Sarasota FL, USA). To create the delivery port layer, two 90-µm inner diameter delivery ports were laser etched (Versa Laser 3.5, Universal Laser Systems, Scottsdale AZ, USA), at a power setting of 7% and a speed of 10%, into a 0.2 mm clear optical grade cast acrylic sheet (Astra Products Inc., Baldwin, NY USA).

To assemble the delivery component, first the unpatterned glass and PDMS channel layers were treated with air plasma (Tegal Plasmod) for 2 mins and brought into contact, with the glass on the flat face of the PDMS piece. Next, the acrylic delivery port layer was chemically bonded to the PDMS channel layer and inlet layer. To perform chemical bonding, both PDMS pieces and the acrylic piece were treated with air plasma for 1.5 mins, then treated with silane solution (Sigma

Aldrich, St. Louis MO, USA) for 25 mins.[33] The acrylic piece was submerged fully in a solution containing 1:10 v/v (3-aminopropyl)trimethoxysilane (APTMS):ethanol, and the two PDMS pieces were submerged partially in a solution containing 1:10 v/v (3-glycidyloxypropyl)trimethoxysilane (GPTMS): ethanol solution. Full submersion of the acrylic layer ensured that both sides of the acrylic were silanized. After silanization, all layers were thoroughly cleaned with ethanol and water and dried with nitrogen. The acrylic delivery port was aligned visually with the PDMS channel, and the pieces were brought into good contact. The PDMS inlet layer was then similarly bonded to the top of the acrylic delivery port layer. Once assembled, the device was left at room temperature for one hour to complete the reaction between the amino- and epoxy-silanes.

The chamber component was fabricated from 3 layers: a 0.2-mm clear optical grade cast acrylic sheet containing an array of ports of 80-µm inner diameter, a rigid acrylic support, and a PDMS culture chamber to house the tissue. The port array was produced by laser etching as in the delivery port layer. The acrylic layer consisted of a rigid 1.5-mm acrylic sheet (McMaster-Carr, Princeton, NJ USA), laser-etched with a 10-mm hole using a power setting of 20% and a speed of 2%. The culture chamber was fabricated in PDMS using soft-lithography and a 10-mm hole punch (World Precision Instruments, Sarasota FL, USA). To assemble the chamber component, the PDMS piece was chemically bonded to the rigid acrylic piece as described above. The two acrylic pieces were bonded together by using clear polyester double-sided adhesive tape (Adhesives Research, Inc., Glen Rock, PA USA) that was laser-etched in advance with a 10-mm hole using a power setting of 15% and a speed of 10%.

3.3.2 R_fOEG synthesis

Triethyleneglycol mono[1H,1H-perfluorooctyl]ether, R_fOEG, was synthesized using published protocols.[34–36] R_fOEG was stored at a stock concentration of 20 mg/mL in FC-40 (Sigma Aldrich, St. Louis MO, USA) at -20°C. For experiments, R_fOEG was diluted to a working concentration of 0.5 mg/mL in FC-40 unless otherwise specified.

3.3.3 Interfacial tension and contact angle measurements

Interfacial tensions and contact angles were measured on a ramé-hart goniometer (model 200-00, ramé-hart instrument co., Succasunna NJ, USA). Interfacial tension was measured by generating a hanging drop of FC40 oil (density 1.855 g/mL) in aqueous saline (density 1.000 g/mL). A 100-μL syringe (Hamilton 1710 with 26s gauge needle) was prepared with PTFE tubing and filled with FC-40 oil containing R_fOEG at 0, 0.1, 0.25, 0.5, or 1 mg/mL. The tip of the tubing was inserted into a cuvette of aqueous solution, typically 1x PBS containing Bovine serum albumin at 0, 0.1, or 1 mg/mL (BSA, Fatty Acid-free, Thermo Fisher Scientific, Hampton NH, USA). Hanging droplets of 3 – 5 μL were generated by driving the syringe and were imaged using the goniometer. Droplets were analyzed using a pendant drop program in ImageJ to calculate interfacial tension (n = 5 droplets per condition).[37]

The contact angle for the three-phase system of oil, aqueous, and fluorinated acrylic surface was measured using DROPimage Advanced software. A silianized piece of acrylic with a port attached by tubing to a syringe was submerged in FC-40 containing various concentrations of R_fOEG. Then a 3-5 μL aqueous droplet containing various amounts of BSA was formed in the oil by applying manual pressure to the syringe. Contact angle was measured for four droplets per condition.

3.3.4 Fluorosilanization of delivery and chamber components

Once both components were fabricated, their acrylic faces were silanized to produce a fluorophilic and hydrophobic surface, using a modification of a gas-phase silanization procedure designed for glass.[29,30] First, both components were treated with air plasma for 1 min. A 300 µL aliquot of tridecafluoro-1,1,2,2-tetrahydrooctyl trichlorosilane (Gelest Inc., Morrisville PA, USA) was placed into a small polypropylene dish in a vacuum desiccator, followed immediately by the two components, and a vacuum was applied for 2 hours. Each component was thoroughly rinsed with water and ethanol and dried with nitrogen. Next, the hydrophobic silane was removed from inside the ports and chamber of the chamber component by plasma treatment for 1 min, while the acrylic face was protected by a clean piece of thin PDMS (SSP, Ballston Spa NY, USA).

3.3.5 Preparation of agarose and tissue slices

All animal work was approved by the Institutional Animal Care and Use Committee at the University of Virginia under protocol #4042, and was conducted in compliance with guidelines from the University of Virginia Animal Care and Use Committee and the Office of Laboratory Animal Welfare at the National Institutes of Health (United States). Both male and female C57BL/6 mice (Jackson Laboratories or Taconic, USA) were used while 7-16 weeks old. On the day of the experiment, the mice were anesthetized with isofluorane and euthanized by cervical dislocation. Six peripheral (inguinal, brachial, and axillary) lymph nodes were removed and placed in ice-cold DPBS (without Calcuim or Magnesium 17-512F/24, Lonza, Walkerville MD, USA), for a brief recovery. The lymph nodes were embedded in 6% low melting point agarose prepared in 1 x PBS and chilled on ice, then punched out using a 10-mm tissue punch (World Precision). A vibratome (Lecia VT1000S, Bannockburn, IL, USA), set at a speed of 90 and a frequency of 3, was used to slice the tissue 300 µm thick in ice-cold 1 x PBS. The slices were immersed in warm

culture media (RPMI supplemented with 10% FBS, 1% L-glutamine an 1% Pen/Strep, 1% Non-essential amino acids, 50 μM beta-Mercaptoethanol, 1 mM pyruvate, 20 mM HEPES (Fisher Scientific, Hampton NH, USA).All tissue slices were placed in a sterile incubator at 37°C with 5% CO_2 and allowed to recover for 1 hour before the start of experiments.

Fresh lymph node slices were immunostained for B cells before being used in delivery experiments. The procedure will be described in an upcoming publication. Briefly, non-specific staining was blocked using antibody CD16/32 (clone 93, Biolegend, San Diego CA, USA), and B cells were labeled with FITC-labeled CD45R/B220 antibody (clone RA3-6B2, Biolegend). Stained slices were washed thoroughly with 1x PBS and immediately used for experiments.

Slices of 6% agarose were prepared in a similar fashion, by casting agarose in a dish and slicing as above into 1x PBS. Agarose slices were stored at 4°C.

3.3.6 Device assembly and operation

All pressure-driven flow was achieved using a Chemyx syringe pump (Fusion 200, Houston TX, USA) loaded with a 50 μL Hamilton Model 1705 RN syringe with a 26s gauge, large hub needle. Connections to the device were made with nonshrinkable PTFE TT-30 tubing with 0.012″ I.D. and 0.009″ wall thickness (Weico Wire, Edgewood NY, USA).

Before assembling the device, the microfluidic channel was filled with aqueous solution using a syringe pump. 1 mL of oil was pipetted onto the top of the filled delivery component. The oil was FC-40 containing 0.5 mg/mL R_fOEG (triethyleneglycol mono[1H,1H-perfluorooctyl]ether), unless otherwise noted. Then, the chamber component was lowered onto the delivery component, sandwiching a thin layer of oil between them and avoiding air bubbles. Steady pressure was maintained until the device was clamped with two binder clips. The culture chamber was then

filled with 1x phosphate buffered saline (PBS). A sample of agarose gel or tissue was placed into the chamber and weighed down using a small stainless steel washer (10 mm O.D. and 5.3 mm I.D., Grainger USA).

To deliver fluid through a desired port, the chamber component was slipped relative to the delivery component and aligned under a microscope. The syringe pump was turned on at the desired flow rate to initiate flow. After 3-5 seconds (unless otherwise stated), the pump was turned off and the device was slipped away, to reposition for another delivery or to a closed position. After all deliveries were complete, the sample was removed, then the chamber was flushed with 1x PBS and refilled for the next sample. All delivery experiments were performed at room temperature.

3.3.7 Measurement of gap height

The height of the gap was measured using a ratiometric approach described previously.[38] BSA was labeled with DyLight 488 NHS ester (Thermo Fisher Scientific, Hampton NH, USA) according to manufacturer recommendations. The device was assembled and the channel was filled with 1 mg/mL labelled BSA in 1x PBS. The chamber component was slipped into a closed position, with the delivery port away from any array port, and the pump was started to force fluorescent BSA solution to spread into the gap. Images were collected of both the gap and the channel upstream of the chamber component, using a AxioZoom macroscope (Carl Zeiss Microscopy, Germany) with an Axiocam 506 Mono camera (14-bit images). Assembly, delivery, and imaging were repeated 3 times.

Images were analyzed using Zen 2 software (Blue Edition, Zeiss) to determine the fluorescent intensity in the channel (FI_{ch}) minus background (FI_{cb}) and the gap, using linescans to average the intensity in each region. For each delivery image, 3 linescans were drawn across the interface of

the BSA solution and FC-40, to measure the background fluorescent intensity (FI_{gb}) on the oil side of the interface and the fluorescent intensity of the gap (FI_g) on the BSA side. The channel depth was independently measured to be 155 μm (H_{ch}). The height of the gap (H_g) was calculated to be 14.1±2.3 μm (n = 3 independent measurements) from:

$$H_g = \frac{(FI_g - FI_{gb}) * H_{ch}}{(FI_{ch} - FI_{cb})} \qquad \text{Equation 3.1}$$

3.3.8 Validation of tissue viability after delivery

To assess the viability of tissue slices after delivery on the movable port device, slices were analyzed by flow cytometry. Analysis was performed on lymph node slices from 1 female mouse (n=15) and 1 male mouse (n=21). Slices (n=12) were sequentially placed in the device and treated with a 5-s delivery of labeled 10-kDa dextran, then cultured for 3 hr along with untreated control slices (n=12). Slices were crushed through a 70 μm filter and centrifuged (Sorvall ST40R Centrifuge, Fisher Scientific) at 400G for 5 min. Cells were resuspended in PBS with 2% serum (VWR), and cells from one subset of untreated control slices were killed with 35% ethanol for 10 mins. All cell suspensions were stained with two live-dead discriminator dyes, 0.01 μM Calcein AM and 0.5 μg/mL 7-AAD (Table S3). Cell viability was analyzed using a FACS Calibur flow cytometer (Table S4), acquiring data using BD CellQuest Pro 5.1 software. Suspensions of fresh murine splenocytes were prepared at 1 million cells/mL as single-stained and unstained controls. Cells were gated on scatter, and compensation using these controls was performed using FCS Express 6 software, setting positive and negative ranges of signal for each dye as shown in Figure S7. Compensation matrices were calculated based on median fluorescent intensity, and applied to experimental plots.

3.3.9 Delivery experiments

All deliveries were monitored in real time using a Zeiss AxioZoom macroscope (Carl Zeiss Microscopy, Germany) with an Axiocam 506 Mono camera, using filter cubes for GFP (Zeiss filter set #38), Rhodamine (#43), and Cy5 (#50). Images (14 bit) were collected before, during, and after delivery. For deliveries with a single fluorescent tracer, time lapse images were collected at 1-sec intervals, while for delivery of multiple tracers, images were collected every 3 seconds. All images were analyzed in Zen 2 software.

Validation experiment: To validate the conditions required for successful delivery, the oil phase (FC40 with R_fOEG at 0, 0.25, 0.5, 1 mg/mL), aqueous phase (0.05 mg/mL 40-kDa FITC-labeled dextran, 0.1 mg/mL BSA, or 1 mg/mL BSA), and flow rate of delivery (0.5, 1, 2, 4 μL/min) were systematically varied. The device was assembled and a 6% agarose slice placed into the chamber. The device was aligned, a 5-sec delivery was performed, and then the device was realigned, for a total of 5 consecutive deliveries. Images of the deliveries were analyzed for spreading of the oil/aqueous interface in the oil gap, and for the radial spread of the fluorescent signal from the aligned port during delivery.

Measuring width of delivery in agarose: After alignment of the delivery port to an array port below a 6% agarose slice, a pulse of Fluorescein (FITC) labeled 150-kDa dextran was delivered to the slice at flow rates ranging from 0.1 to 1.6 μL/min (n=4). In a separate experiment, a mixture of ovalbumin (OVA) labeled with NHS-rhodamine, FITC labeled 150-kDa dextran, and Alexa Fluor 647 labeled 40-kDa dextran (all from Thermo Fisher Scientific), each at 0.05 mg/mL, was prepared. The Stokes radii for the dextrans were obtained from the vendor. The OVA and 40-kDa dextran were labeled in-house using succinimidyl ester-dye conjugates, according to manufacturer recommendations. The mixture was delivered at a flow rate of 0.4 μL/min (n=5). Delivery width

was determined from image analysis in Zen software as described previously.[11] Briefly, a linescan was drawn across the delivery region and corrected for the background fluorescence of the slice measured prior to delivery. Data points directly over the port were excluded due to its high fluorescent intensity and the remaining data were fit to a Gaussian curve in Graphpad Prism version 7. The delivery width was defined as 2 standard deviations of the Gaussian curve. To fit the curve of the spread of analyte with respect to time and flow rate, we considered the volume delivered per unit time:

$$(\tfrac{1}{4})\pi w^2 h = Q\Delta t \qquad \text{Equation 3.2,}$$

we approximated the delivery volume to be a cylinder, where w [μm] is the width of the delivery, h [μm] is the height of the sample, Q [μL/min] is the volumetric flow rate and Δt [sec] is the length of time of delivery. Solving for width gives:

$$w = 2\sqrt{\frac{QT}{\pi h}} \qquad \text{Equation 3.3.}$$

These widths were plotted and fit to a two-parameter square root curve, $y = a\sqrt{x - b}$, where x was the flow rate or time of delivery and y was the delivery width.

Delivery to live lymph node tissue: The device was assembled and a lymph node slice was placed onto the chamber. A 3-5 second pulse of Alexa Fluor 647-labeled 40-kDa dextran was delivered at a flow rate of 0.5 μL/min. After the first delivery, the device was repositioned and another delivery was performed. This was repeated for four different slices and with slight variations on three separate occasions.

3.4 Results and Discussion

3.4.1 Design of the chip

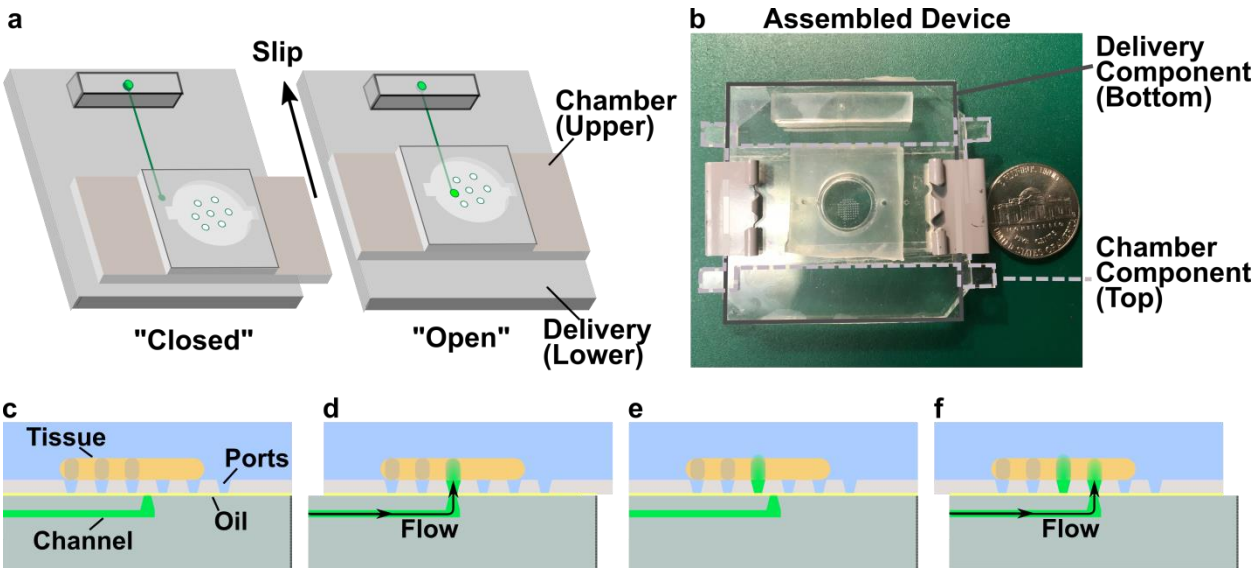

Figure 3.1 Design and prototype of the movable port device. a) 3D schematic of assembled device in closed (ports are unaligned) and open (ports are aligned) positions. b) A photograph of an assembled device, pictured with a United States nickel, with the delivery component (solid) and chamber component (dashed) outlined. c-f) Fluidic control for on-demand delivery through a user-selected port. An oil layer (yellow) separates the aqueous stimulant (green) from the aqueous solution (blue) and tissue (brown and cream) in the culture chamber. c) Delivery port starts in a closed position. d) Delivery port is slipped to align with an array port (open position). Pneumatic pressure flows the stimulant solution into the sample. e) Pneumatic pressure is stopped, and the device is slipped to break up the aqueous column, repositioning the port under the acrylic (closed position). f) A second delivery occurs through another array port if the device is slipped again.

To create a "mobile" port beneath a tissue slice, we designed a SlipChip device with two multi-layer components (Figure 3.1a and b). The lower "delivery" component contained an underlying microchannel that terminated in a single port (delivery port), while the upper "chamber" component included an open perfusion chamber to house the tissue sample. An array of ports (port array) was located at the bottom of the perfusion chamber. With this design, the user placed a tissue sample into the chamber and slipped the port array relative to the delivery port to target a desired subsection of tissue (Figure 3.1a).

The premise of the chip was that an aqueous solution delivered through the microchannel was targeted to a particular array port by an immiscible oil layer, sandwiched between the two

components, which prevented leakage into the gap (Figure 3.1c-f). Once the delivery port was slipped into alignment with an array port, an aqueous column bridged the oil layer between them and enabled pressure-driven flow into the sample (Figure 3.1d). To stop delivery, pressure-driven flow was turned off and the device was slipped to break the aqueous column (Figure 3.1e). This process was repeatable for multiple deliveries (Figure 3.1f).

3.4.2 Design criteria for fabrication and surface chemistry

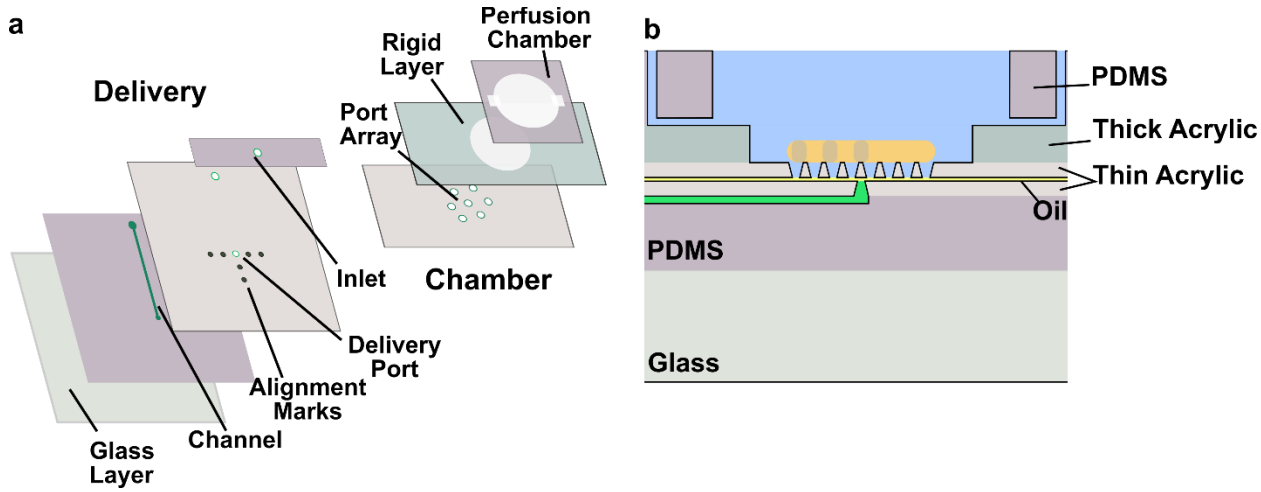

Figure 3.2: Fabrication strategy for the movable port device. a) Exploded view of device showing the layers for each component. b) A cross-section of the assembled device, with the materials labelled for each layer and color coded.

The materials and assembly strategy were selected to enable rapid fabrication of a prototype device (Figure 3.2a). The microchannel and perfusion chamber layers were fabricated from polydimethylsiloxane (PDMS) because of the ease of patterning and bonding this material. Since PDMS is flexible, a rigid glass backing and a thick slab of acrylic were added to the delivery and chamber components, respectively, to avoid bending.[25] To enable slipping, the layers facing the gap between the two components (i.e., the delivery port and port array layers), were fabricated in low-friction acrylic. Acrylic had the additional advantage that it was readily patterned with a CO_2 laser and chemically bonded to the other layers. Laser etching produced conical ports ranging from

90 -110 µm for the bottom and 70-90 µm for the top of the cone, which were oriented as shown in Figure 3.2b during device assembly. In preliminary work, we found that this orientation was required to minimize the flow of culture media from the chamber into the oil gap. To facilitate alignment under opaque tissue, alignment markers were laser etched in a cross-hair pattern with the delivery port at the center (Figure 3.2a).

The dimensions of the device enabled the delivery port to align with any port in the port array without exposing the channel or ports to an air interface. The port array maximized the number of ports in a 25 mm^2 area, while also allowing sufficient distance for the delivery port to manually slip between array ports. An array of 100-µm diameter ports pitched 500-µm center-to-center met these requirements. In future development, this spacing could be reduced by using higher resolution fabrication methods to produce smaller ports and denser port arrays.

The chemistry of the oil/water interface was selected to enable delivery of aqueous solutions of biomolecules. We used FC-40, a water-immiscible fluorocarbon oil, because it is biologically inert and has a moderate viscosity appropriate for SlipChip applications.[24,30] A short-chain surfactant, triethyleneglycol mono[1H,1H-perfluorooctyl]ether (R_fOEG), was included to prevent protein adsorption at the aqueous/oil interface and to control the interfacial tension (Figure 3.3).[34] R_fOEG, unlike longer chain surfactants, facilitates rapid drop coalescence, which was desirable for the formation of the aqueous column.[35]

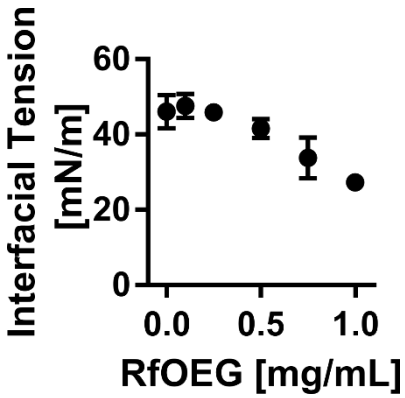

Figure 3.3 Interfacial tension of 1xPBS and FC-40 oil as a function of the concentration of RfOEG. (mean ± Std dev, n=5)

3.4.3 Capillary pressure provided controlled delivery without leakage

Unlike a traditional microfluidic channel, which uses solid walls to constrain pressure-driven fluid flow, this system uses only an oil/water interface to direct the flow of aqueous solution through the gap from the delivery port to the selected array port. We derived a simple physical model to describe the delivery and predict the conditions required for flow without leakage into the gap (Figure 3.4a).

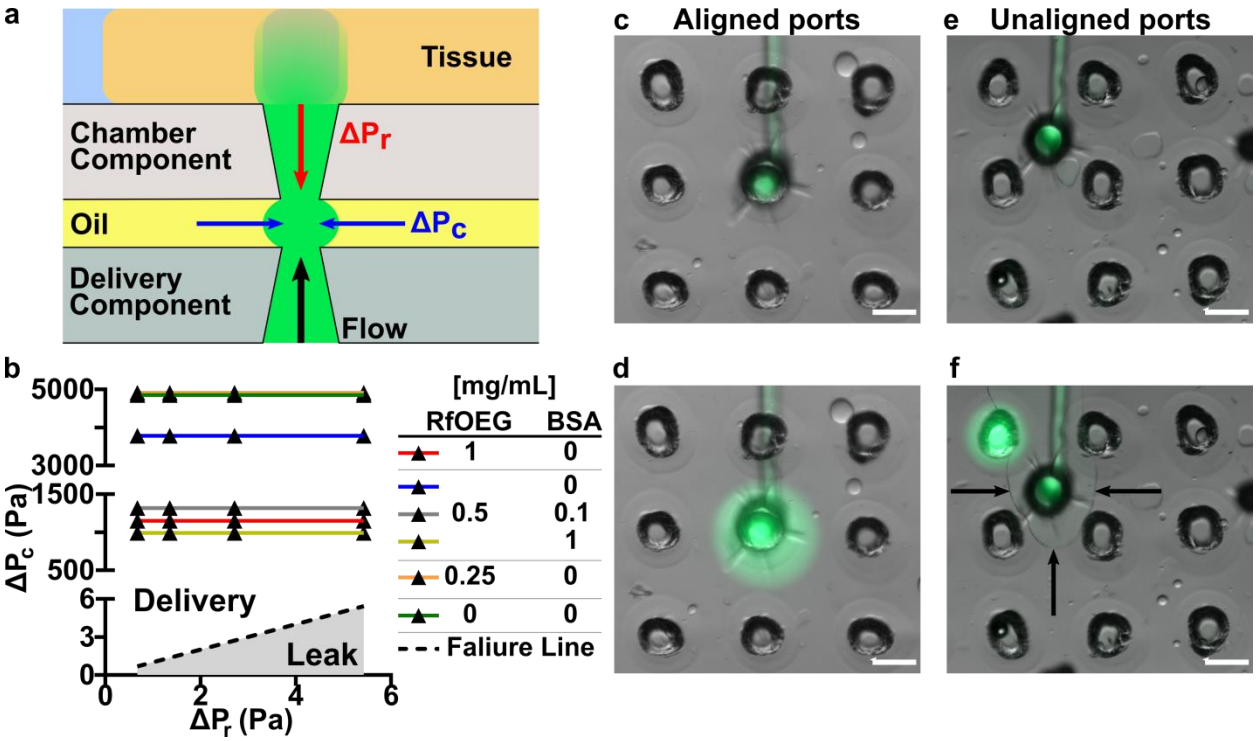

Figure 3.4: Delivery through aligned ports was controlled by the capillary pressure and pressure due to flow resistance. a) Illustration of pressures imposed upon the aqueous column during delivery. ΔP_r is the pressure difference caused by the resistance of the port, and ΔP_c is the capillary pressure at the aqueous/oil interface in the gap. The drawing is not to scale; the depth of the oil layer is exaggerated for clarity. b) A phase diagram of ΔP_r versus ΔP_c. Predicted regimes of delivery to the culture chamber versus a leak into the oil gap are divided by theoretical failure line (dashed). For each condition, five different deliveries were tested for successful flow into the culture chamber versus a leak into the oil gap. The device performed reproducibly under each condition; each triangle (▲) represents five consecutive successful deliveries to a slice of agarose gel. c, d) Micrographs of the delivery port aligned with an array port and the resulting controlled delivery of aqueous solution (green). e) Delivery and array ports were purposely misaligned, resulting in (f) leaking in the gap, visible by the interface that forms in the gap layer (black arrows). Aqueous solution eventually emerged through a port that was not aligned with the delivery port. Scale bars are 200 μm.

Two major pressures exerted on the aqueous column during delivery were considered. The first was the capillary pressure from the oil/aqueous interface, ΔP_c (Figure 3.4a, blue arrows). To have inward capillary pressure rather than outward pressure, which would cause wicking, it was essential that the surfaces exposed to the gap be hydrophobic and fluorophilic. Although acrylic was not naturally wetted by fluorocarbon oil, fluorosilianizing the acrylic layers facing the oil raised the contact angle for an aqueous droplet in oil to > 90° (Table 3.1).

Under these conditions, ΔP_c opposes spreading in the gap and encourages delivery through the connected array port. The capillary pressure was calculated using the Laplace equation,

$$\Delta P_c = \frac{2\gamma cos\theta}{h} \qquad \text{Equation 3.4,}$$

where γ [N/m] is the aqueous/oil interfacial tension, θ [radians] is the contact angle of an aqueous droplet in oil on the fluorinated acrylic substrate, and h [m] is the height of the gap (typically 14 μm in this device).[29,30,36]

Table 3.1: Capillary pressure calculations for conditions tested in Figure 3b. To vary the capillary pressure, both the concentration of RfOEG in FC-40 oil and BSA in 1x PBS was varied. ΔP_c was calculated from Equation 3.4.

Concentration of R_fOEG (mg/mL)	Concentration of BSA (mg/mL)	Interfacial tension γ (mN/m)	Contact angle θ (degrees)	Calculated ΔP_c (Pa)[a]
0	0	46.0	137.9	-4.85×10^3
0.25	0	45.9	139.0	-4.91×10^3
0.5	0	41.6	129.8	-3.78×10^3
1	0	27.2	107.3	-1.15×10^3
0.5	0.1	13.7	132.8	-1.32×10^3
0.5	1	11.4	127.6	-9.90×10^2

[a] *The gap height was as 14.1 μm for this calculation to match gap height measurements.*

The second major pressure working on the system during delivery was the pressure due to flow resistance through the array port, ΔP_r (Figure 3.4a, red arrow). This pressure acts counter to the delivery and encourages spreading in the gap. The pressure difference across the array port was

calculated by first finding the flow resistance of the port, R [$\frac{Pa*s}{m^3}$], using the Poiseuille equation for laminar flow:

$$R = \frac{8\mu L}{\pi r^4} \quad \text{Equation 3.5}$$

where μ [Pa*s] is the viscosity of the aqueous phase, L [m] is the length of the port, and r [m] is radius of the port.[37] For simplicity, the conical ports were treated as cylindrical in shape, with radius *r* [m] equal to the average of the top and bottom radii of the cone. The pressure drop across the port was calculated as

$$\Delta P_r = Q * R \qquad \text{Equation 3.6}$$

where Q [$\frac{m^3}{s}$] is the volumetric flow rate through the port.[37]

Table 3.2: Calculation of pressure due to flow resistance for varied flow rates in Figure 3b. ΔP_r was calculated according to Equation 3.5 and Equation 3.6.

Flow rate Q (m^3/s)	**Calculated ΔP_r (Pa)[b]**
8.33×10^{-12}	0.68
1.67×10^{-11}	1.36
3.33×10^{-11}	2.72
6.67×10^{-11}	5.43

[b] *The viscosity used in this calculation was 1.00×10^{-3} Pa s, the port length was 200 μm, and the port radius was approximated as 100 μm.*

We predicted that the aqueous column would be contained and successful delivery to the chamber would occur if the capillary pressure was greater than the pressure due to flow resistance ($\Delta P_c > \Delta P_r$). To test this hypothesis, we selected 24 different conditions of varied ΔP_c and ΔP_r, spanning a >10-fold range of each variable (Figure 3.4b). ΔP_r was varied by changing the flow rate, and ΔP_c was varied by changing the concentrations of oil-phase R_fOEG and aqueous-phase bovine serum albumin (BSA). ΔP_r and ΔP_c were calculated for each condition using Equations 3.4 and 3.6. Due to experimental constraints, ΔP_c was at least two orders of magnitude larger than ΔP_r

in all cases (Table 3.1 and Table 3.2), and no experimentally feasible approach fell in the predicted leak regime. Therefore, to illustrate what a leak would look like, we deliberately misaligned the delivery port and initiated flow (Figure 3.4e). This forced the aqueous solution into the gap (visible as an interface in the oil layer), and delivery eventually occurred through an unaligned port (Figure 3.4f).

To match the prediction, all tested conditions needed to have successful flow into the chamber with no leaking in the gap. Each condition was tested experimentally in five consecutive deliveries to a slice of agarose gel, each made after slipping to a different port in the chamber array (Figure 3.4b). Deliveries were monitored by timelapse microscopy. Leaks were indicated by the formation of a visible interface in the gap layer (Figure 3.4f), while flow into the chamber was indicated by a radial spread of fluorescent signal originating from the aligned port (Figure 3.4c and d). In all cases, no spreading was observed in the gap, and the delivery occurred through the aligned port. These results matched the prediction of the model, supporting its validity.

We were also concerned with protein adsorption during slipping and its potential impact on the ability to perform repetitive deliveries with the device. We tested this by delivering BSA labeled with Dylight 488 at a concentration that was typical or higher than that of most biologically active proteins (50 μg/mL), then slipped away, and repeated this process 5 times. It was found (by fluorescence) that slipping did not cause visible protein

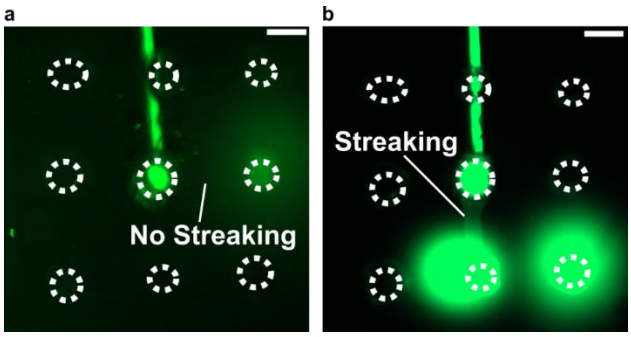

Figure 3.5 Wetting on the top surface of the gap. The scale bar is 200 μm. a) At 0.05 mg/mL BSA, no wetting of the surfaces (no streak of fluorescent signal after slipping was observed after slipping to the center port from the port to its right. b) At 1 mg/mL of BSA, a streak of fluorescence appeared when the port was slipped from the previous port below it. The contrast in the two images is not scaled the same, in order to make the streak visible.

adsorption to the surface, and that sequential deliveries were possible. Next, we tested delivery at BSA concentrations typical of its use as a carrier protein (0.1 and 1 mg/mL). In some cases, the BSA solution wetted the top surface of the gap during slipping (Figure 3.5), but interestingly these streaks of aqueous solution did not affect the precision of subsequent deliveries (Figure 3.4b). No leaking was observed in the gap during subsequent deliveries, and the aqueous fluid remained constrained to the aligned port. Successful delivery may have been facilitated by retained hydrophobicity of the bottom surface of the gap, coupled with a lower flow resistance through the array port than through the thin aqueous streak. We conclude that the current device is suitable for delivery of analytes with lower surface activity (small molecules, dextrans, dilute proteins), and for delivery of concentrated amphipathic proteins in cases where minor loss due to surface adsorption is acceptable. To accommodate quantitative delivery of high concentrations of amphipathic proteins, it may be useful to fabricate the device from a material with a lower surface energy, such as fluorinated polymers.[29,38]

3.4.4 Delivery into the sample was governed by convection

3.4.4.1 Spread of analyte increased as a function of flow rate

Having confirmed that delivery occurred without leakage into the gap, we moved on to characterize the spread of analyte into a sample above the aligned ports. Predictable localization is required to stimulate the substructures found in tissue. First, we tested the effect of flow rate on the spread of analyte by measuring the width of the fluorescent signal, using 6% agarose gel as a model tissue (Figure 3.6a-c). Approximating the delivery region as a cylinder, the width of

fluorescent signal is expected (Equation 3.2 and 3.3) to increase with the square root of the product of volumetric flow rate and time and the experimental data were indeed well fit by such a curve (Figure 3.6c). This result confirmed that even at higher flow rates, fluid was not lost into the gap between the two components. The device provided delivery resolution as low as 200 µm at the lowest flow rates (0.1 and 0.2 µL/min), which is sufficient for stimulation of subsections of murine and human tissue.[1,10,39]

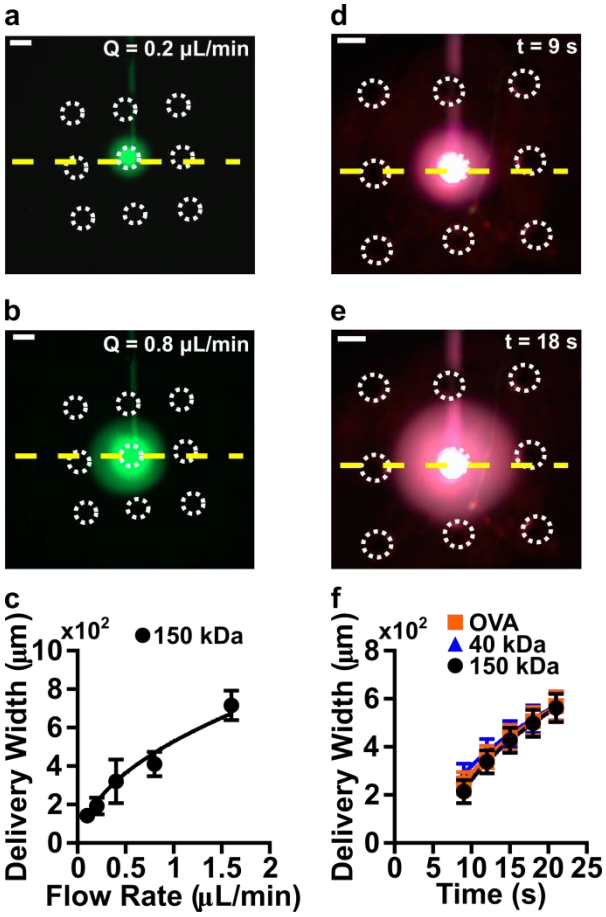

Figure 3.6 The spread of analyte was controlled by the flow rate and length of delivery. a, b) A representative delivery of 150-kDa fluorescein-labeled dextran to 6% agarose (t = 10 s), at (a) 0.2 µL/min and (b) 0.8 µL/min. c) The width of the fluorescent signal increased with flow rate (n=4). d, e) A mixture of model stimulants was delivered to 6% agarose for (d) 9 and (e) 18 seconds at a flow rate of 0.4 µL/min. f) The width of the fluorescent signal increased similarly with the length of time of the delivery for all three model stimulants, regardless of molecular size (n=5). Graphs show mean and std. dev. Data were fit to the equation $y=a\sqrt{(x-b)}$, with R2 =0.89(c), 0.84(f, OVA), 0.81 (f, 40-kDa), and 0.87 (f, 150-kDa). Scale bars in images are 200 µm.

3.4.4.2 Analyte size did not affect the spread

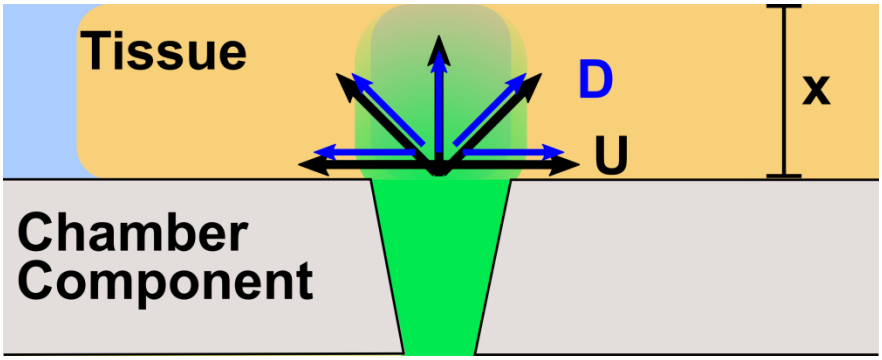

Figure 3.7 An illustration of the geometry used to calculate the Peclét number. D [m2/s] is the diffusion coefficient of the analyte through the tissue matrix. U [m/s] is flow velocity through the tissue. The diffusion distance, x [m], was set to the thickness of the tissue (300 µm).

As an analyte solution is delivered through the port, the analyte experiences simultaneous convection and diffusion through the tissue or hydrogel matrix. The Péclet number (*Pe*) is a dimensionless number that compares the rates of convection and diffusion. For this geometry (Figure 3.7), it was defined by the equation,

$$Pe = Ux/2D \qquad \text{Equation 3.7,}$$

where U [m/s] is the velocity at the terminus of the port, x [m] is distance through the tissue, and D [m^2/s] is the diffusion coefficient. At large Pe (>> 1), convection dominates transport, while at small Pe (<< 1), diffusion dominates. Even for the slowest flow rate used in these experiments, we calculated Pe = 760, based on U = 2.1 x10^{-4} m/s (0.1 µL/min), x = 300 µm (the thickness of the agarose slice), and D = 4.2 x10^{-11} m^2/s, the diffusion of 40-kDa dextran in dilute agarose gel.[11,40] Based on the high Péclet number, the delivery width is expected to essentially independent of the rate of diffusion, and therefore of the size of the molecule.

To test the prediction that convection dominates the analyte spread, three model stimuli of varying size were delivered to agarose gel (Figure 3.6d-f): ovalbumin (OVA), 40-kDa dextran, and 150-kDa dextran. These molecules have Stokes radii of approximately 30, 45, and 85 Å,

respectively.[41] All three stimuli (regardless of Stokes radii) had similar fluorescent signal widths at each time point, consistent with convection controlling the spread of analyte (Figure 3.6f).

The validations performed in agarose serve as a starting point for estimating the timing and flow rate needed to achieve a desired spatial resolution of delivery in tissue. Tissues vary by orders of magnitude in their permeability to fluid flow,[42] which is expected to affect the velocity of convection through the tissue during delivery. To maintain the same spatial resolution of delivery, the delivery pulse should be slower or shorter in a more permeable (less dense) tissue, and faster or longer in a less permeable (more dense) tissue.

3.4.5 Tissue viability was not affected by stimulation on the device

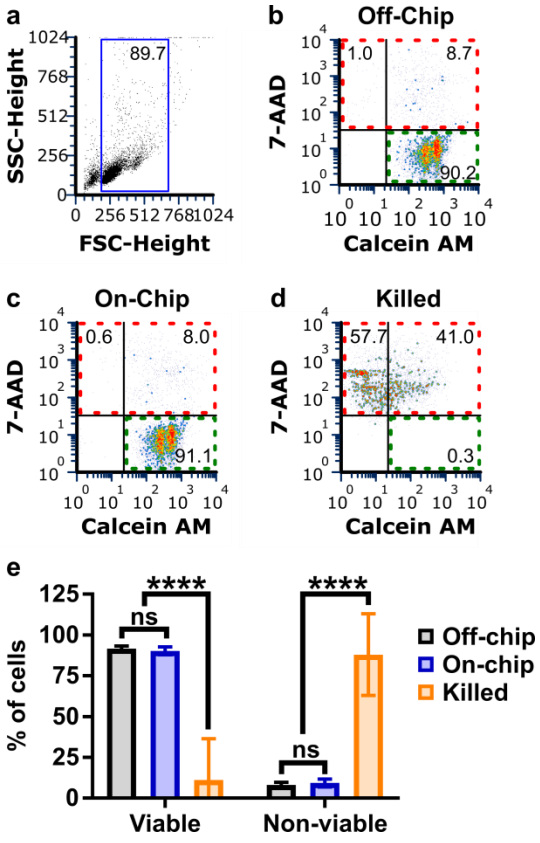

*Figure 3.8: Tissue viability was unaffected by stimulation on the device. Slices were dissociated and analyzed by flow cytometry. a-d) Cells obtained from tissue slices were (a) gated on scatter and (b-d) analyzed for intensity of Calcein AM and 7-AAD, for (b) slices cultured off-chip, (c) slices treated on the device, and (d) slices killed with 35% ethanol. Viable gate (high Calcein AM, low 7-AAD) shown in green dashed boxes; non-viable gate (high 7-AAD) shown in red dashed boxes. e) The percentage of cells that were viable differed significantly only between killed controls and both device-treated (on-chip) samples and live (off-chip) controls. Likewise, the percentage of cells that were non-viable differed significantly only between live/device and killed samples. **** indicates p-value < 0.0001.*

Next, we tested whether on-chip stimulation affected the viability of tissue slices, using lymph node tissue as a model system. The materials of the chip, PDMS and acrylic, are both compatible with a variety of biological samples during short exposures,[42,43] and FC-40 oil has a long history of use with cell cultures.[44–47]

Therefore, we hypothesized that tissue viability would be unaffected by the brief period of potential exposure required for local stimulation on the device. To test this hypothesis, fresh lymph node slices were placed in the device, treated with a short delivery, and then returned to a standard cell culture incubator for 3 hr. The total time that each tissue slice spent on the device was about 2 minutes, which is representative of a typical stimulation experiment. The 3-hr incubation provided time for any delayed effects of on-chip exposure to take hold, for example toxicity mediated by protein transcription or translation. Control slices were left undisturbed in the incubator for the same period. After this period, all slices were crushed and stained with Calcein AM and 7-AAD. Flow cytometry analysis (Figure 3.8a-d) showed that there was no significant difference in viability between cells from the chip-treated and off-chip live control samples (Figure 3.8e), which indicates that the stimulation on the device had no negative effect on the health of the tissue on this timescale. We have previously shown that lymph node slices (off-chip) retain viability for at least 6 hr.[10] Therefore, it is reasonable to assume that acute responses (< 6 hr) can be studied with this local delivery system, e.g. to study initial responses to inflammatory stimuli.[48] Culture for overnight or longer would require sterilization of the device and aseptic handling during the experiment.

3.4.6 On-demand stimulation of live tissue slices through the movable port

The ultimate purpose of this device was to enable one or more deliveries without manual manipulation of a tissue slice after its placement into the device. Delivery to murine lymph node

tissue was used as a proof-of-concept. The lymph node is a structured organ with sub-regions that are a few hundred microns across, including B cell-rich follicles near the periphery and a central paracortical region containing T cells and antigen-presenting cells.[39] We have previously used delivery to specific regions of lymph node slices to quantify protein diffusion in each region and to deliver model protein therapeutics, using a device with a stationary port.[10,11]

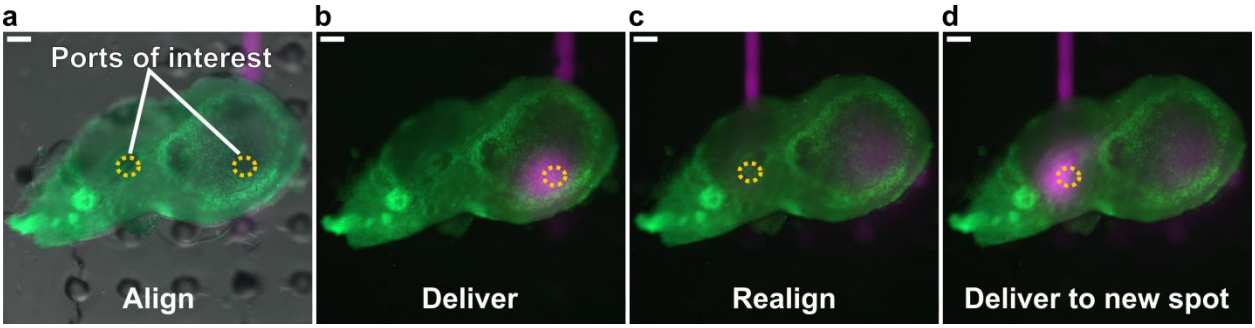

Figure 3.9 The SlipChip-based device was capable of multiple deliveries to lymph node slices. a) Overlay of bright field and fluorescence images of a representative lymph node slice, with the two ports of interest highlighted by a yellow outline. Bright green indicates B220 immunostaining for B cells. The array of ports is visible in an out-of-focus plane below the tissue. A solution containing 40-kDa dextran (magenta) is visible in the channel below. b) A first delivery of 40-kDa dextran to the lymph node slice. c) The device was realigned for the second delivery. d) Second delivery of the 40-kDa dextran to the lymph node slice. Scale bar is 200 μm.

Here, we tested whether the movable-port device could deliver to specific regions of interest without manual alignment of the tissue. Lymph node slices were immunostained in advance with a FITC labeled B cell-specific antibody (anti-B220) to visualize the geography of the tissue. A slice was placed onto the device and not touched again, and the delivery port was slipped to deliver 40-kDa dextran first to one region and then another. Figure 3.9 shows a representative experiment with a typical two-lobed lymph node sample (Figure 3.9a), featuring delivery to a T cell region (Figure 3.9b), slipping to a new position in the other lobe of the tissue (Figure 3.9c), and a second delivery (Figure 3.9d). As expected for 40-kDa dextran, a relatively small macromolecule, much of the first delivery diffused away from the initial site in the 30 seconds used for realignment. All deliveries successfully targeted the designated areas, in 4 independent tissue slices, and in similar experiments conducted on 3 separate days.

As described in the introduction, state-of-the-art microfluidic devices for local fluid delivery to tissue samples are either movable pen-like probes or devices featuring stationary ports below the tissue. In contrast to movable probes that use bidirectional push-pull fluid flow,[15–18,21] unidirectional fluid delivery through a port (movable or fixed) cannot simultaneously collect fluid samples for off-line analysis. However, unidirectional flow better enables delivery through thick tissue slices (here, 300 μm). We and others have previously used fixed ports to deliver samples to targeted regions;[10–14] this was achieved by strategically placing the tissue sample over the port, and moving it as needed with gentle force. The movable port strategy reported here provides a novel mode of local stimulation that requires minimal tissue handling; the tissue could be placed nearly at random over the port array and still target the region of interest. The primary tradeoff for this increased flexibility was that the operation of the device was more complicated than for stationary ports, since the user must reconfigure the chip mid-experiment. However, the design is compatible with mechanical slipping using micromanipulators,[30] and with future automation.

Further development of this microfluidic technology will focus on improving on the fabrication methods for this device. The fabrication described here enabled rapid production of prototype devices; future versions of the chip will be redesigned for hot embossing or injection molding for rapid fabrication. Use of fluorinated polymeric substrates may minimize surface adsorption of proteins, and use of narrower and more densely spaced ports may improve the delivery resolution. As the current device is already sufficient for local delivery to substructures of interest, it will be used to facilitate drug screening in lymphoid tissue going forward.

3.5 Conclusions

Here we have reported a novel microfluidic device with a movable port for live tissue stimulation. The tissue rests atop an array of ports, which are slipped by the user to align over a single pump-fed port below. Slipping is lubricated and leakage is prevented by a layer of biocompatible oil between the two components of the chip. Incorporation of pump-driven flow that crosses the oil layer is an innovative use of a SlipChip design, and we showed that successful delivery to the tissue chamber that was consistent and predictable due to the high capillary pressure present in the system. The width of the stimulated region was determined by flow rate and time of delivery, and sequential local deliveries to live tissue were possible without manual realignment of the tissue. Though demonstrated here for lymph node tissue, the device is expected to be compatible with any mechanically stable soft tissue sample or hydrogel, and could be used to study the effects of local fluid flow and drug delivery. In the future, combining on-demand local stimulation with spatially resolved readouts of cell activity in tissue may enable the application of this device to the study of drug responses in tissues.

3.6 References:

1. Huang, Y., Williams, J. C. & Johnson, S. M. Brain slice on a chip: opportunities and challenges of applying microfluidic technology to intact tissues. *Lab. Chip* **12**, 2103 (2012).
2. Sivagnanam, V. & Gijs, M. A. M. Exploring Living Multicellular Organisms, Organs, and Tissues Using Microfluidic Systems. *Chem. Rev.* **113**, 3214–3247 (2013).
3. Lander, A. D. How Cells Know Where They Are. *Science* **339**, 923–927 (2013).
4. Müller, P. & Schier, A. F. Extracellular Movement of Signaling Molecules. *Dev. Cell* **21**, 145–158 (2011).

5. Nelson, C. M. & Bissell, M. J. Of Extracellular Matrix, Scaffolds, and Signaling: Tissue Architecture Regulates Development, Homeostasis, and Cancer. *Annu. Rev. Cell Dev. Biol.* **22**, 287–309 (2006).
6. Qi, H., Kastenmüller, W. & Germain, R. N. Spatiotemporal Basis of Innate and Adaptive Immunity in Secondary Lymphoid Tissue. *Annu. Rev. Cell Dev. Biol.* **30**, 141–167 (2014).
7. Pompano, R. R., Chiang, A. H., Kastrup, C. J. & Ismagilov, R. F. Conceptual and Experimental Tools to Understand Spatial Effects and Transport Phenomena in Nonlinear Biochemical Networks Illustrated with Patchy Switching. *Annu. Rev. Biochem.* **86**, 333–356 (2017).
8. Lämmermann, T. In the eye of the neutrophil swarm-navigation signals that bring neutrophils together in inflamed and infected tissues. *J. Leukoc. Biol.* **100**, 55–63 (2016).
9. Rana, K. & Neeves, K. B. Blood flow and mass transfer regulation of coagulation. *Blood Rev.* **30**, 357–368 (2016).
10. Ross, A. E., Belanger, M. C., Woodroof, J. F. & Pompano, R. R. Spatially resolved microfluidic stimulation of lymphoid tissue ex vivo. *The Analyst* **142**, 649–659 (2017).
11. Ross, A. E. & Pompano, R. R. Diffusion of cytokines in live lymph node tissue using microfluidic integrated optical imaging. *Anal. Chim. Acta* **1000**, 205–213 (2018).
12. Mohammed, J. S., Caicedo, H. H., Fall, C. P. & Eddington, D. T. Microfluidic add-on for standard electrophysiology chambers. *Lab. Chip* **8**, 1048–1055 (2008).
13. Chang, T. C. *et al.* Parallel microfluidic chemosensitivity testing on individual slice cultures. *Lab Chip* **14**, 4540–4551 (2014).
14. Tang, Y. T. *et al.* Development and characterization of a microfluidic chamber incorporating fluid ports with active suction for localized chemical stimulation of brain slices. *Lab. Chip* **11**, 2247–2254 (2011).

15. Chen, D. *et al.* The chemistrode: A droplet-based microfluidic device for stimulation and recording with high temporal, spatial, and chemical resolution. *Proc. Natl. Acad. Sci.* **105**, 16843–16848 (2008).
16. Juncker, D., Schmid, H. & Delamarche, E. Multipurpose microfluidic probe. *Nat. Mater.* **4**, 622–628 (2005).
17. Queval, A. *et al.* Chamber and microfluidic probe for microperfusion of organotypic brain slices. *Lab. Chip* **10**, 326–334 (2010).
18. Kaigala, G. V., Lovchik, R. D., Drechsler, U. & Delamarche, E. A Vertical Microfluidic Probe. *Langmuir* **27**, 5686–5693 (2011).
19. Asperti-Boursin, F., Real, E., Bismuth, G., Trautmann, A. & Donnadieu, E. CCR7 ligands control basal T cell motility within lymph node slices in a phosphoinositide 3–kinase–independent manner. *J. Exp. Med.* **204**, 1167–1179 (2007).
20. Legradi, A., Varszegi, S., Szigeti, C. & Gulya, K. Adult rat hippocampal slices as in vitro models for neurodegeneration: Studies on cell viability and apoptotic processes. *Brain Res. Bull.* **84**, 39–44 (2011).
21. Slaney, T. R. *et al.* Push-pull perfusion sampling with segmented flow for high temporal and spatial resolution in vivo chemical monitoring. *Anal. Chem.* **83**, 5207–5213 (2011).
22. Lovchik, R. D., Kaigala, G. V., Georgiadis, M. & Delamarche, E. Micro-immunohistochemistry using a microfluidic probe. *Lab. Chip* **12**, 1040–1043 (2012).
23. Kashyap, A., Autebert, J., Delamarche, E. & Kaigala, G. V. Selective local lysis and sampling of live cells for nucleic acid analysis using a microfluidic probe. *Sci. Rep.* **6**, (2016).
24. Du, W., Li, L., Nichols, K. P. & Ismagilov, R. F. SlipChip. *Lab. Chip* **9**, 2286–2292 (2009).

25. Chang, C.-W., Peng, C.-C., Liao, W.-H. & Tung, Y.-C. Polydimethylsiloxane SlipChip for mammalian cell culture applications. *Analyst* **140**, 7355–7365 (2015).
26. Liang *et al.* Individually addressable arrays of replica microbial cultures enabled by splitting SlipChips. *Integr. Biol.* **6**, 796 (2014).
27. Li, L. & Ismagilov, R. F. Protein crystallization using Microfluidic technologies based on valves, droplets, and SlipChip. (2010) doi:10.1146/annurev.biophys.050708.133630.
28. Li, L., Du, W. & Ismagilov, R. User-Loaded SlipChip for Equipment-Free Multiplexed Nanoliter-Scale Experiments. *J. Am. Chem. Soc.* **132**, 106–111 (2010).
29. Li, L., Karymov, M. A., Nichols, K. P. & Ismagilov, R. F. Dead-End Filling of SlipChip Evaluated Theoretically and Experimentally as a Function of the Surface Chemistry and the Gap Size between the Plates for Lubricated and Dry SlipChips. *Langmuir* **26**, 12465–12471 (2010).
30. Pompano, R. R., Platt, C. E., Karymov, M. A. & Ismagilov, R. F. Control of initiation, rate, and routing of spontaneous capillary-driven flow of liquid droplets through microfluidic channels on SlipChip. *Langmuir* **28**, 1931–1941 (2012).
31. Mohammed, J. S., Caicedo, H., Fall, C. P. & Eddington, D. T. Brain Slice Stimulation Using a Microfluidic Network and Standard Perfusion Chamber. *J. Vis. Exp. JoVE* (2007) doi:10.3791/302.
32. Qin, D., Xia, Y. & Whitesides, G. M. Soft lithography for micro- and nanoscale patterning. *Nat. Protoc.* **5**, 491–502 (2010).
33. Tang, L. & Lee, N. Y. A facile route for irreversible bonding of plastic-PDMS hybrid microdevices at room temperature. *Lab. Chip* **10**, 1274–1280 (2010).

34. Roach, L. S., Song, H. & Ismagilov, R. F. Controlling nonspecific protein adsorption in a plug-based microfluidic system by controlling interfacial chemistry using fluorous-phase surfactants. *Anal. Chem.* **77**, 785–796 (2005).
35. Cristini, V. & Tan, Y.-C. Theory and numerical simulation of droplet dynamics in complex flows—a review. *Lab Chip* **4**, 257–264 (2004).
36. Hansang Cho, Ho-Young Kim, Ji Yoon Kang, & Tae Song Kim. How the capillary burst microvavle works. *J. Colloid Interface Sci.* **306**, 379–385 (2007).
37. Beebe, D. J., Mensing, G. A. & Walker, G. M. Physics and applications of Microfluidics in biology. *Annu. Rev. Biomed. Eng.* **4**, 261–286 (2002).
38. Ren, K., Dai, W., Zhou, J., Su, J. & Wu, H. Whole-Teflon microfluidic chips. *Proc. Natl. Acad. Sci.* **108**, 8162–8166 (2011).
39. Willard-Mack, C. L. Normal structure, function, and histology of lymph nodes. *Toxicol Pathol* **34**, 409–424 (2006).
40. Nicholson, C. & Tao, L. Hindered diffusion of high molecular weight compounds in brain extracellular microenvironment measured with integrative optical imaging. *Biophys. J.* **65**, 2277–2290 (1993).
41. Erickson, H. P. Size and Shape of Protein Molecules at the Nanometer Level Determined by Sedimentation, Gel Filtration, and Electron Microscopy. *Biol. Proced. Online* **11**, 32 (2009).
42. Wiig, H. & Swartz, M. A. Interstitial Fluid and Lymph Formation and Transport: Physiological Regulation and Roles in Inflammation and Cancer. *Physiol. Rev.* **92**, 1005–1060 (2012).
43. Regehr, K. J. *et al.* Biological implications of polydimethylsiloxane-based microfluidic cell culture. *Lab. Chip* **9**, 2132 (2009).

44. Midwoud, P. M., Janse, A., Merema, M. T., Groothuis, G. M. M. & Verpoorte, E. Comparison of Biocompatibility and Adsorption Properties of Different Plastics for Advanced Microfluidic Cell and Tissue Culture Models. *Anal. Chem.* **84**, 3938–3944 (2012).
45. Walsh, E. J. *et al.* Microfluidics with fluid walls. *Nat. Commun.* **8**, 816 (2017).
46. Lagus, T. P. & Edd, J. F. A review of the theory, methods and recent applications of high-throughput single-cell droplet microfluidics. *J. Phys. Appl. Phys.* **46**, 114005 (2013).
47. Holtze, C. *et al.* Biocompatible surfactants for water-in-fluorocarbon emulsions. *Lab. Chip* **8**, 1632–1639 (2008).
48. Calabro, S. *et al.* Vaccine adjuvants alum and MF59 induce rapid recruitment of neutrophils and monocytes that participate in antigen transport to draining lymph nodes. *Vaccine* **29**, 1812–1823 (2011).

Chapter 4: Versatile and selective fluorination of the surface of polymeric materials after stereolithography 3D printing

Adapted From:
Catterton, M., Montalbine, A. N. & Pompano, R. (2021)
doi:10.26434/chemrxiv.14167472.v1.

4.1 Abstract

With the microfluidics community embracing 3D resin printing as a rapid fabrication method, controlling surface chemistry has emerged as a new challenge. Fluorination of 3D printed surfaces is highly desirable in many applications due to chemical inertness, low friction coefficients, anti-fouling properties and the potential for selective hydrophobic patterning. Despite sporadic reports, silanization methods have not been optimized for covalent bonding with polymeric resins. As a case study, we tested the silanization of a commercially available (meth)acrylate-based resin (BV-007A) with a fluoroalkyl trichlorosilane. Plasm oxidation was unnecessary for silanization of this resin. Solvent-based deposition in a fluorinated oil (FC-40) generated the highest comparted to other methods tested, yielding hydrophobic surfaces with contact angle > 110˚ under optimized conditions. Attenuated Total Reflectance-Fourier Transform Infrared (ATR-FTIR) spectroscopy indicated that the increase in contact angle correlated with consumption of a carbonyl moiety, suggesting covalent bonding of the silane without plasma oxidation. Consistent with a covalent bond, the silanization was resistant to mechanical damage and hydrolysis in methanol, and was stable over long-term storage. When tested on a suite of photocrosslinkable resins, this silanization protocol generated highly hydrophobic surfaces (contact angle > 110˚) on three resins and moderate hydrophobicity (90 – 100˚) on the remainder. Selective patterning of hydrophobic regions in an open 3D-printed microchannel was possible in combination with simple masking techniques. Thus, this facile fluorination strategy is expected to be applicable for resin-printed materials in a variety of contexts including micropatterning and multiphase microfluidics.

4.2 Introduction

As the microfluidics community has increasingly adopted resin 3D printing for device fabrication, including stereolithography (SLA) and digital light processing (DLP) printing,[1,2] methods to control the surface chemistry of 3D printed devices are emerging as a critical challenge.[3] In resin printing, UV/visible light is used to cross-link a photocurable, polymeric resin in a layer-by-layer fashion to produce a 3D structure.[1,2] While methods for surface functionalization are well established for traditional materials such as glass and polydimethylsiloxane (PDMS), those methods do not necessarily translate directly to the polymeric materials used for 3D printing. A particular challenge is to generate a fluorinated surface on a 3D printed chip. Fluorinated surfaces offer many advantages for microfluidic device design, such as controlled surface wettability for passive fluidic control, chemical inertness, resistance to surface fouling, and low friction coefficient.[4–7] These properties historically made fluorinated surfaces invaluable for multiphase microfluidic chips. [8–13] By patterning fluorination amidst a non-fluorinated surface, patterned hydrophobicity has been used to generate droplets, create microarrays, and control microfluidic valving.[14–16] Therefore, facile methods to selectively fluorinate the surface of polymeric SLA and DLP resins are required, particularly for the commercially available resins used by most laboratories.

Currently, there are few methods available to generate a fluorinated surface on 3D printed material, particularly a patterned surface. One option is to start directly with a fluorinated resin,[17] but these are rare in practice due to limited commercial options. Additionally, fully fluorinated devices are not readily patterned at the surface due to their chemical inertness. Alternatively, selective surface patterning is possible by using printed pieces modified at the surface with fluorinated coatings.[3,18,19] Polymeric liquid coatings provide a robust hydrophobic layer up to

hundreds of micrometers thick,[18] but may be inappropriate for microscale features that are easily blocked or filled in. A chemical vapor deposition method can be used to generate a thin, highly hydrophobic coating by polymerizing a fluorinated acrylate film on the surface, but has limited use in enclosed channels.[20,21] Thin coatings can also be achieved by including a polymerization initiator in the resin, to provide covalent anchor points for fluorinated polymer brushes.[19] However, polymer brushes may exhibit poor mechanical stability during abrasion.[3]

Silanization using fluorinated silanes is a reliable method for molecular-scale surface modification of glass and polydimethylsiloxane (PDMS),[22,23] but silanization of polymeric materials can be challenging. So far there have been sporadic reports of silanization of resin 3D printed microfluidic devices, e.g. to fluorinate 3D printed molds for PDMS[24] and to attach reactive functionalities for bonding of 3D printed pieces.[25] In some cases, the printed polymer had to be coated with a layer of silica to enable silanization.[26,27] Extensive surface oxidation is usually required to generate enough silane-reactive functional groups (e.g. hydroxyls) at the polymer surface, but not all polymers can withstand such treatment, as they may degrade after plasma exposure.[4,28,29] To date, there has been little testing of the conditions required for direct fluoroalkyl silanization of resin printed pieces, nor characterization of the hydrophobicity and stability of the silanized surface.

Here, we aimed to develop a robust and straightforward silanization protocol using (tridecafluoro-1,1,2,2-tetrahydrooctyl) trichlorosilane, a fluoroalkyl silane, and a suite of commercially available SLA and DLP resins to generate a highly fluorinated surface for use in microfluidic devices. While optimizing the reaction conditions to generate the highest possible contact angle, we found, surprisingly, that surface oxidation using air plasma was unnecessary for silanization. To characterize the surface and investigate reactive groups involved in forming a

covalent bond between the printed resin and the fluoroalkyl silane, we measured the air/water contact angle of the silanized surface and used infrared (IR) spectroscopy. We tested the ability of the method to selectively pattern hydrophobic regions in a 3D printed open microchannel, and further tested the applicability of the optimized method to four additional resins. The method is facile, versatile, and allows for dynamic patterning of a hydrophobic surface on a resin-printed piece.

4.3 Methods

4.3.1 3D Printing

Printed parts were designed using Autodesk Inventor 2018. The CAD files were sliced at 50 µM intervals using MII Utility Shortcut V 3.27 and printed using a CADworks3D M50-405 printer (MiiCraft, CADworks3D). The commercial resins included were BV-007A (Clear) (MiiCraft, CADworks 3D), Green Master Mold (MiiCraft, CADworks 3D), Dental LT Clear Resin (V2) (FormLabs), and Asiga PlasClear V2 (iMakr). A house-made photoresin consisting of 0.4 % w/v phenylbis(2,4,6-trimethylbenzoyl)phosphineoxide (Irgacure 819) (Therofisher) dissolved in poly(ethylene glycol) diacrylate (PEG-DA) (MW 250) (Sigma Aldrich) was also included in the suite of resins tested.[30] The printer setting for each resin can be found in Table 4.1. Printed parts were rinsed with either 95% ethanol (Koptec), isopropanol (Fisher chemical), or methanol (Fisher chemical) as recommended for by the manufacturer for the resin. Printed pieces were post-cured in an UV-light box, then stored at room temperature on the bench top in polystyrene petri dishes (Fisher) prior to silanization.

Table 4.1: Printing settings used for each resin on the CADworks3D M50 printer with a 405 nm light source. For all resins, the peeling speed was Slow, and gap adjustment was 0.1 mm.

Resin	Curing time (s)	Base layers	Base curing (s)	Buffer layers	Light power (%)	Rinsing solvent	Post-curing time
BV-007A	1.15	1	9.0	1	75	MeOH	20 sec
Green master mold	5.00	1	40	2	100	IPA	10 min
Dental	4.50	1	8.5	3	78	IPA	30 min
Plasclear	10.0	1	22	2	78	EtOH	2 min
PEG-DA	2	1	3	1	100	EtOH	30 sec

4.3.2 Surface Treatment of 3D Printed Pieces

Where noted, some printed parts were plasma treated using a BD-20AC laboratory corona treater (Electro-Technic Products, Chicago IL, USA). Printed parts were placed 3 mm below the plasma source and treated for 5 – 60 s immediately prior to surface silanization. For gas-phase deposition, 200 μL of neat tridecafluoro-1,1,2,2-tetrahydrooctyl trichlorosilane (Gelest Inc., Morrisville PA, USA) was placed in a vacuum desiccator in a small polypropylene dish, followed immediately by the printed parts, and a vacuum was applied for 2 hours at room temperature. For solvent deposition, the surface of the printed part was submerged in a 10% v/v solution of tridecafluoro-1,1,2,2-tetrahydrooctyl trichlorosilane in solvent (Fluorinert FC-40 (Sigma Aldrich) or 200 proof ethanol (Koptec) for 30 min at room temperature, unless otherwise specified. After silanization, surfaces were rinsed with 95% ethanol and DI water and dried with a nitrogen gun.

4.3.3 Contact Angle Measurement

Surface air/water contact angles were measured using a ramé-hart goniometer (model 200-00, ramé-hart instrument co., Succasunna NJ, USA) and DROPimage Advanced software. Contact angle was measured for 3 separate printed pieces per condition, by pipetting one 5-μL droplet of

DI water per print onto the silanized surface. 8x8x8 mm^3 cubes were used for the printed piece, and oriented so the smooth flat face of the printed cube was tested.

4.3.4 Surface Chemistry Characterization with Infrared Spectroscopy

The surface chemistry of the printed parts was examined by using an iD7 ATR Nicolet IS5 FT-IR spectrophotometer (Thermo Fischer Scientific). The IR spectrum was measured on the flat smooth face of a 10x10x2 mm^3 printed rectangular prism. The instrument was set to a constant gain of 4, and the background was collected prior to each session. Data was collected, visualized, and processed using the OMNIC software (Thermo Fischer Scientific).

4.3.5 Robustness testing

Printed pieces were silanized according to the optimized method. To test the resistance to mechanical damage, the parts were rubbed against a clean petri dish for 30 s, and the air/water contact angles of the silanized surfaces were measured before and after. To test stability after storage, silanized printed parts were stored in a petri dish at room temperature under ambient light, and the air/water contact angles were repeatedly measured over time. Finally, contact angles were measured before and after soaking the printed parts for 2 hours in methanol.

4.3.6 Selective Patterning of 3D Printed Surfaces

Rectangular prisms (20x15x3 mm^3) were printed using BV-007A resin. Each print contained an embossed cross-shaped open channel with a rectangular cross-section (1 mm deep, 2 mm wide). Scotch tape (3M) was cut and aligned manually to prevent the fluoroalkyl silane solution from coming into contact with portions of the printed surface inside the channel. Taped pieces were immersed in a solution of 10% v/v (tridecafluoro-1,1,2,2-tetrahydrooctyl) trichlorosilane in FC-40 for 30 min in a fume hood at room temperature. After treatment, pieces were rinsed with 95%

ethanol and DI water and dried with nitrogen. To test the functionality of the patterned surface, solutions of food coloring in water were pipetted into the arms of the embossed features.

4.3.7 Data Analysis

Statistical tests and curve fitting were performed using Graphpad Prism version 9. Half-lives and half-times of exponential fits were calculated according to

$$half\ time = ln\,2\,/k \qquad \text{Equation 4.1}$$

where k is the rate constant from the fit.

4.4 Results and Discussion

4.4.1 Plasma oxidation was not necessary or effective for silanization of SLA printed pieces

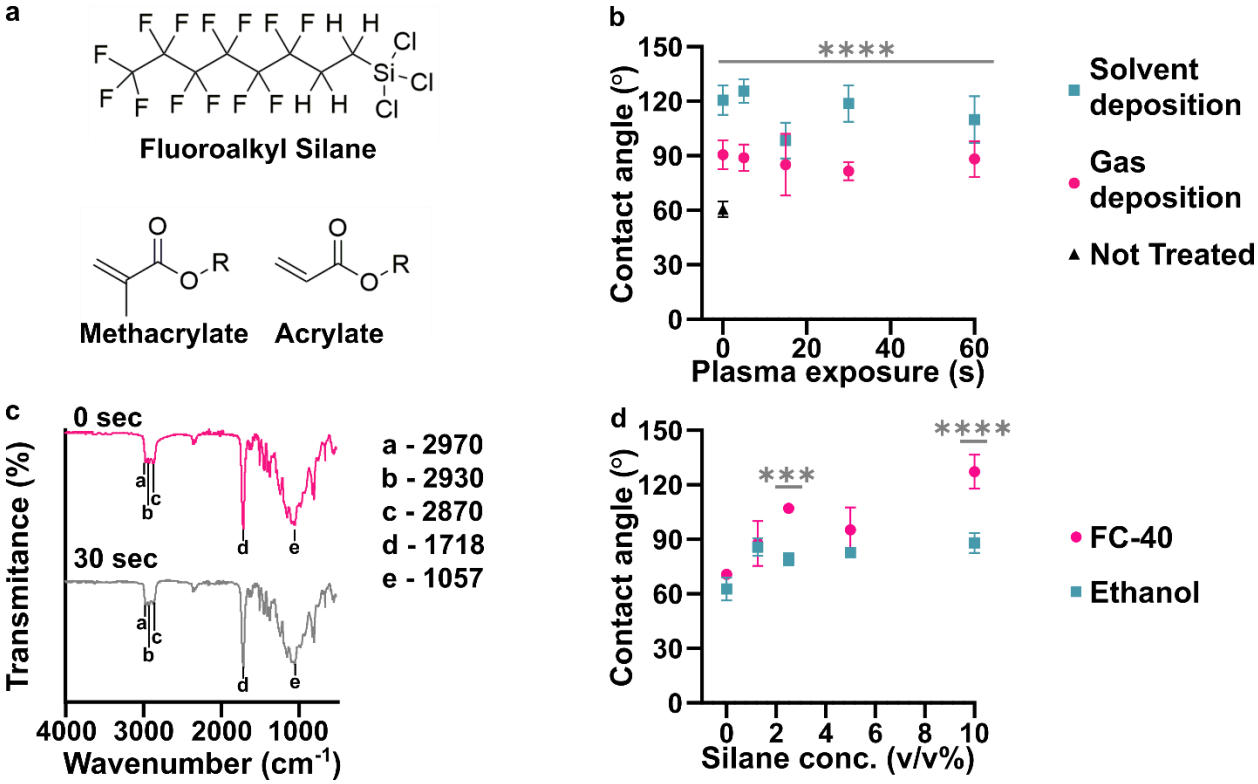

*Figure 4.1: Effects of plasma treatment and silanization on the chemistry and hydrophobicity of DLP printed pieces. (a) Chemical structures of the fluoroalkyl silane and monomer acylate and methacrylate base used for many resin formulations. (b) Air/water contact angles of BV-007A after silanization by solution-phase (blue squares, FC-40 solvent) or gas-phase (pink dots) deposition after varied times of treatment with air plasma (n=3, mean ± std dev). The black triangle represents printed BV-007A pieces that received neither plasma treatment nor any silane treatment. Two-way ANOVA for solution vs gas-phase silanization (**** p<0.0001). (c) ATR-FT IR spectrum of the BV-007A surface with no exposure to air plasma (pink) and after 30 s plasma treatment (grey), without silanization. (d) Air/water contact angles of BV-007A surface after solution-phase silanization in FC-40 (pink dot) or ethanol (blue square). Two-way ANOVA with Sidak's multiple comparisons to compare between solvents (****p <0.0001, *** p<0.001).*

While the precise composition of most commercial resins is proprietary, MSDS information states that many are based on acrylate and/or methacrylate polymers (Figure 4.1a). Silanization of related polymeric materials such as poly(methyl methacrylate) (PMMA) requires oxidation to generate hydroxyl groups that undergo condensation reactions with the silane reagent.[4,11] Similarly, prior reports of silanization of an acrylate-based 3D printed material included activation of the surface with plasma treatment.[24,25] Therefore, we first tested the efficacy of silanization of

3D printed pieces as a function of the duration of exposure to air plasma. As a case study, we selected a clear (meth)acrylate-based resin formulated specifically for printing microfluidic devices, BV-007A resin from MiiCraft, and sought to silanize it with (tridecafluoro-1,1,2,2-tetrahydrooctyl) trichlorosilane (Figure 4.1a). Two common methods of silanization were tested: gas-phase deposition [24,31–34] and liquid-phase deposition.[11,31] For the latter, we used a 10% v/v solution of silane in FC-40 fluorinated oil.

Surprisingly, we found that even in the absence of plasma treatment (0 s exposure), silanization significantly increased the air/water contact angle for both methods (gas phase, $p<0.005$; solvent, $p<0.001$) compared to the 60˚ contact angle of the unslianized printed piece (Figure 4.1b, and Figure 4.2). While gas-phase deposition provided a contact angle near 90˚, the lower boundary for hydrophobicity, the solution-phase method provided a significantly larger ($p < 0.0001$) contact angle close to 120˚, the upper limit for a flat, fluorinated surface.[23,35,36] Plasma treatment from 5 to 60 s did not further increase the contact angle. Wanting to further test the impact of plasma cleaning on the surface chemistry, we next used IR spectroscopy to investigate functional groups on the surface of printed BV-007A pieces.

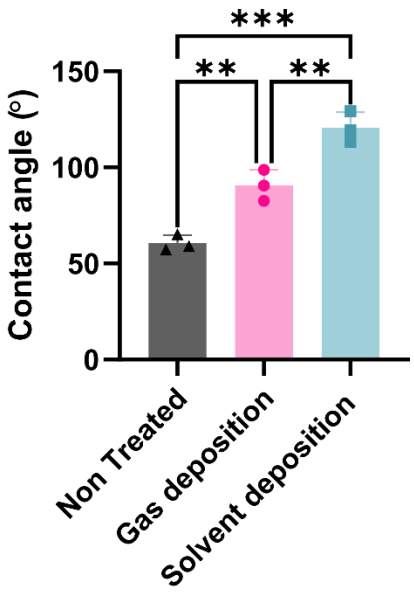

*Figure 4.2 Air/water contact angles of BV007A after silanization by either gas-phase (pink dots) or solution-phase (blue squares, FC-40 solvent) deposition, and a not treated (black triangles) control (n-3, mean ± std dev) without air plasma activation. One-way ANOVA with Tukey's multiple comparison test against the different silanization methods.(**p<0.005, ***p<0.0005)*

We expected that sufficient exposure of BV-007A pieces to air plasma would oxidize the surface to form alcohol and/or carboxylic acid groups.[37] To characterize the surface chemistry and investigate the extent of surface activation at short plasma treatment times, we collected surface ATR FI-IR spectra of the

printed pieces (Figure 4.1c). As expected for (meth)acrylate-based BV-007A, the spectra closely resembled that of commercial sheet of PMMA (Figure 4.3). The peaks at 2970, 2930, and 2870 cm^{-1} were assigned to alkane sp^3 C-H stretching. A major C=O stretch peak at 1718 cm^{-1} was attributed to the carbonyl in the backbone of the (meth)acrylate-based polymer as well as other carbonyl-containing components of the resin, e.g. photoinitiators and photoabsorbers. The C-O-C stretching was assigned to the peaks ranging from 1000 – 1300 cm^{-1} in the fingerprint region.[38] Treating BV-007A printed pieces with air plasma for 30 – 60 s did not alter the IR spectra substantially (Figure 4.1c and data not shown). In particular, no characteristically broad alcohol band (3550 – 3200 cm^{-1}) was observed, and there was no change in the alkyl CH stretches or carbonyl peak. These data were consistent with plasma treatment not affecting the contact angle after silanization (Figure 4.1b). As a positive control, oxidation from the plasma treatment was verified using both glass and PDMS, whose contact angle decreased after 5 s of plasma treatment as expected (Table 4.2). Prior reports of plasma treatment of PMMA used longer treatment times (5 min and greater) to modulate the surface polarity,[39,40] but we found that treatment of BV-007A pieces with air plasma for longer than 2 min generated cracks in the surface. Since plasma treatment was unnecessary for silanization and in fact was ineffective at oxidizing the BV-007A surface at short times, we proceeded to optimize and characterize the silanization of BV-007A pieces it its absence.

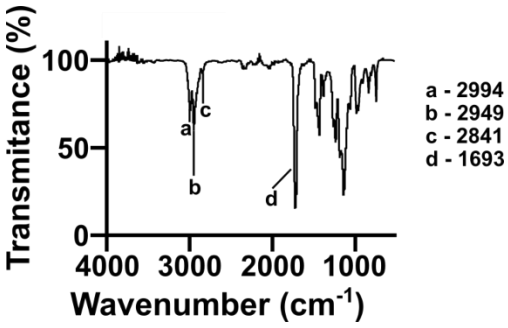

Figure 4.3 The ATR FT-IR spectra of a 1.5 mm acrylic sheet (McMaster-Carr, Princeton, NJ USA). Peaks a, b, and c were assigned to the sp3 C-H stretching in the polymer backbone. Peak d was assigned to the carbonyl group.

.

Table 4.2 The contact angle for plasma treated glass and PDMS. N=2

Material	Plasma time (sec)	Contact angle (degree)
Glass	0	33 ± 2
	5	12 ± 0.3
	30	10 ± 2
PDMS	0	82 ± 5
	5	24 ± 1
	30	32 ± 7

4.4.2 Solvent deposition was most effective when a fluorocarbon oil was used as a solvent.

Having established that solution-phase deposition was more effective than gas-phase deposition, we further optimized the choice of solvent and concentration of silane. Two solvents were tested: ethanol (200 proof), a common solvent for deposition of trichlorosilanes,[31,41] and FC-40, a fluorinated oil.[11] Whereas deposition from ethanol solution was largely ineffective (contact angles < 90˚) regardless of silane concentration, deposition from FC-40 solution had a concentration-dependent effect, yielding an average contact angle of ~ 120˚ at 10 % v/v silane (Figure 4.1d). Therefore, 10% v/v of the fluorinated silane in FC-40 was used for all further experiments.

4.4.3 Time dependence of the reaction provides support for covalent bond formation

Next, we tested the time dependence of the silanization reaction. The contact angle increased in a time-dependent manner with a half-time of 3.4 min, reaching a plateau after 15 min (Figure 4.4a). To complement the contact angle data and assess the extent of bond formation between the fluoroalkyl silane and BV-007A, ATR-FT IR spectra were collected from these samples (Figure 4.4b). The spectra changed noticeably over this time period. In particular, the carbonyl stretch at

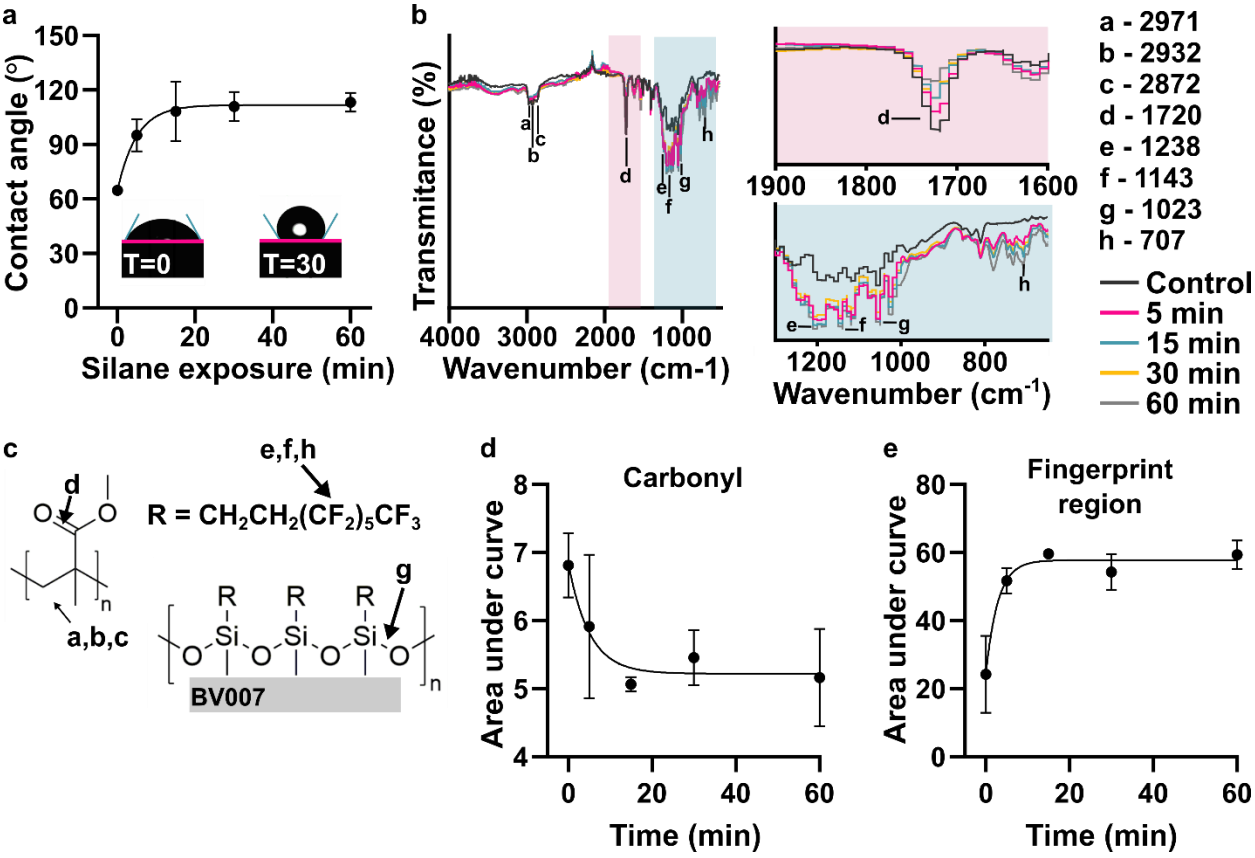

Figure 4.4: Time dependence of the chemical reaction. (a) Contact angle of the fluorinated surface after various amount of silane treatment (n=3, mean ± std dev). The data were fit to an exponential curve, $y = 111 - 46.9e^{-0.201x}$, R^2 =0.844. Insets show images of droplets on BV-007A surface after 0 and 30 min of silanization. (b) ATR-FT IR spectrum of printed BV-007A pieces after various times of silane treatment. Two regions of interest are highlighted: the carbonyl peak at 1720 cm^{-1} and the finger print regions 650-1300 cm^{-1}. (c) The chemical structures present in a methyl methacrylate-based resin and from the fluoroalkyl are labeled with the corresponding IR spectra peak. (d) The area under the carbonyl peak decreased in a time-dependent manner (n=3, mean ± std dev), fit to an exponential decay $y = 55.9e^{-0.115x} + 43.3$, R^2 =0.936. (e) The area under the curve of the finger print region increased in a time-dependent manner, fit to an exponential curve, $y = 57.7 - 24.2e^{-0.348x}$, R^2 =0.855.

1716 cm^{-1} decreased in intensity over time (Figure 4.4b - c), and the peak area was well fit by exponential decay equation with a half-life of 3.5 min (Figure 4.4d). This observation suggested a molecular reaction between the resin and the fluoroalkyl silane that consumes a carbonyl, though the data do not distinguish between the methacrylate carbonyl and any carbonyls that may be present in the resin's photoinitiators or photoabsorbers.

An immediate increase in fingerprint region intensity was consistent with the addition of fluoroalkyl silane to the surface of the print (Figure 4.4b, c and e). New peaks included those at 1023 cm^{-1}, assigned to Si-O-R stretching,[42] 1232 and 1142 cm^{-1}, consistent with asymmetric and symmetric C-F stretches, and 707 cm^{-1}, assigned to the C-F wag.[43] This increase had a half-time of only 2.0 min, shorter than the decay of the carbonyl, suggesting that physical adsorption of the silane may have preceded the covalent reaction (Figure 4.5). The -C-H stretch peaks at 2872, 2932, and 2971 cm^{-1} were still present after silanization (Figure 4.4b - c).[44] From both the contact angle measurements and the IR spectra, we concluded that the silanization reaction likely resulted in a covalent bond, and that 30 min was sufficient for reaction completion and generation of a highly hydrophobic surface.

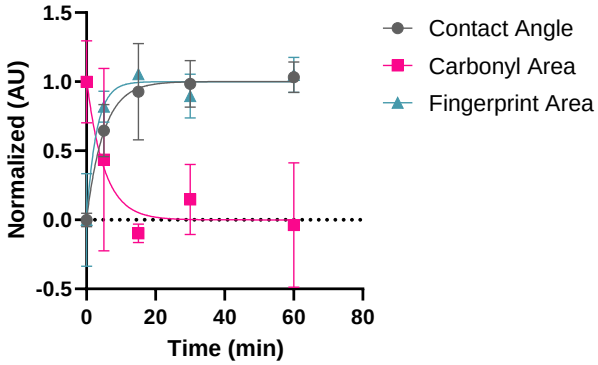

Figure 4.5 Normalized data of the contact angle, carbonyl peak area, and fingerprint area after various amount of time exposed to the fluoroalkyl silane. Data was normalized using the equation $y_{normalized} = (y - min)/(max - min)$*, where min and max were the min and max y-values of the original data, respectively (i.e. the mean value at t = 0 and the plateau). The data were fit to one-phase exponential curves. Contact angle:* $y = 1 - 0.003e^{-0.2x}$*,* R^2 *=0.84. Carbonyl area:* $y = 1e^{-0.2x}$*,* R^2 *=0.51. Fingerprint area:* $y = 1 - 0.0006e^{-0.3x}$*,* R^2 *=0.85.*

4.4.4 Robustness and stability of fluorination procedure

To establish the practical utility of the method, we considered the sensitivity of the procedure to the state of the printed piece and characterized the stability of the hydrophobic surface. First, we considered that the surface chemistry of the printed piece may change over time and potentially alter the reactivity with the trichlorosilane, e.g. due to slow cross-linking of residual monomer under ambient light.[45,46] To test the efficacy of silanization as a function of light-induced aging, printed parts were treated with either the manufacturer-recommended 20 s or an extended 360-s

UV exposure during the post-curing process. We estimate that continuous 360-s exposure was an equivalent dose of light as being on a bench top under ambient light for 32 days from Equation 4.2.

$$Time\ (Day) = \frac{Light\ box\ dose\ (J) * 1\ (Day)}{Amibent\ light\ intensity\ \left(\frac{J}{s}\right) * 86400\ (s)} \qquad \text{Equation 4.2}$$

The extended UV cure created discoloration and warped some of the pieces, so only pieces with a flat top surface were used for subsequent silanization. No significant difference was observed in the water contact angles of the control pieces (20 s) compared to the pieces with extended UV exposure (360 s), either before or after silanization (Figure 4.6a). This result was consistent with our informal observations that month-old BV-007A pieces yielded similar contact angles after silanization as recently printed (1-3 days old) pieces. Therefore, the silanization method appears insensitive to the age of the piece, at least in this timescale, which enables robust fabrication procedures.

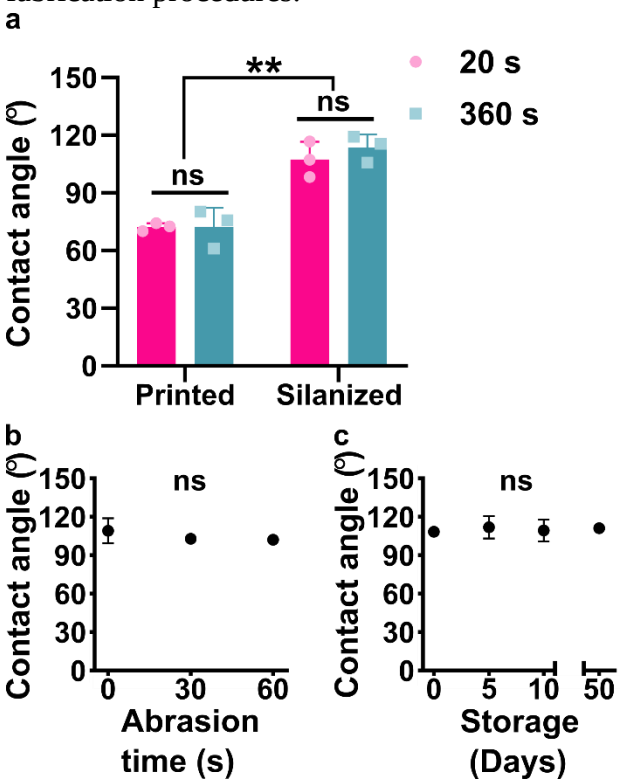

*Figure 4.6 Robustness of the method to the age of the printed piece, abrasion, and storage time after silanization. (a) Contact angle of DLP printed pieces (BV-007A) that were silanized with or without extended UV curing (n=3 printed parts for each condition, mean ± std dev). Two-way ANOVA with Tukey's multiple comparisons (ns, $p>0.05$, ** $p<0.005$). (b,c) Contact angle of silanized BV007 after deliberate mechanical abrasion (b) or long term storage (c) (n=3 printed parts for each condition, mean ± std dev). One-way ANOVA (ns, $p>0.05$).*

Next, we assessed the robustness of the silanized surface when subjected to mechanical damage and extended storage, a property that affects the range of potential uses, handling, and storage. Silanized printed pieces were subjected to gentle mechanical damage by manually rubbing the piece against a clean polystyrene surface, mimicking normal wear and tear during use. The water contact angle of the fluorinated pieces of BV-007A was not significant altered by this process (Figure 4.6b), indicating that the surface is stable under mild abrasion conditions. Similarly, when silanized pieces of BV-007A were stored on the bench, the contact angles remained unchanged for at least 50 days, the longest time point measured (Figure 4.6c). We did observe that the initial contact angle in these experiments was slightly lower than in previous experiments, which we attribute to hydrolysis of the trichlorosilane during storage because replacement of the silane stock improved the hydrophobicity (data not shown). We concluded that the silanized surface was quite stable and the method was robust to the age of the resin though sensitive to the quality of the silane stock, all of which are consistent with the formation of a covalent bond during the silanization reaction.

4.4.5 Patterning of surface hydrophobicity on 3D printed parts

Compared to printing with a fully fluorinated resin, site-specific patterning is an advantage of post-print modifications, offering the potential for passive fluidic control. Therefore, we tested the ability of the silanization protocol to selectively pattern hydrophobic patches on the surface of BV-007A resin, using a pair of intersecting open channels in a simple, recessed cross design. The arms of the cross were protected from the silanization using adhesive tape, while the center square was silanized to generate a pattern of four separate fluid compartments, separated by a surface tension barrier. In the non-silanized control, colored solutions pipetted into the arms of channel mixed readily in the center of the cross (Figure 4.7a, Not treated), whereas a micropatterned hydrophobic

patch in the center of the cross successfully constrained the solutions to the arms (Figure 4.7a, Pattern). These data demonstrate that because the silanization method requires contact of the liquid silanization solution with the printed surface, it is easily patterned by physical masking strategies to define the silanized area.

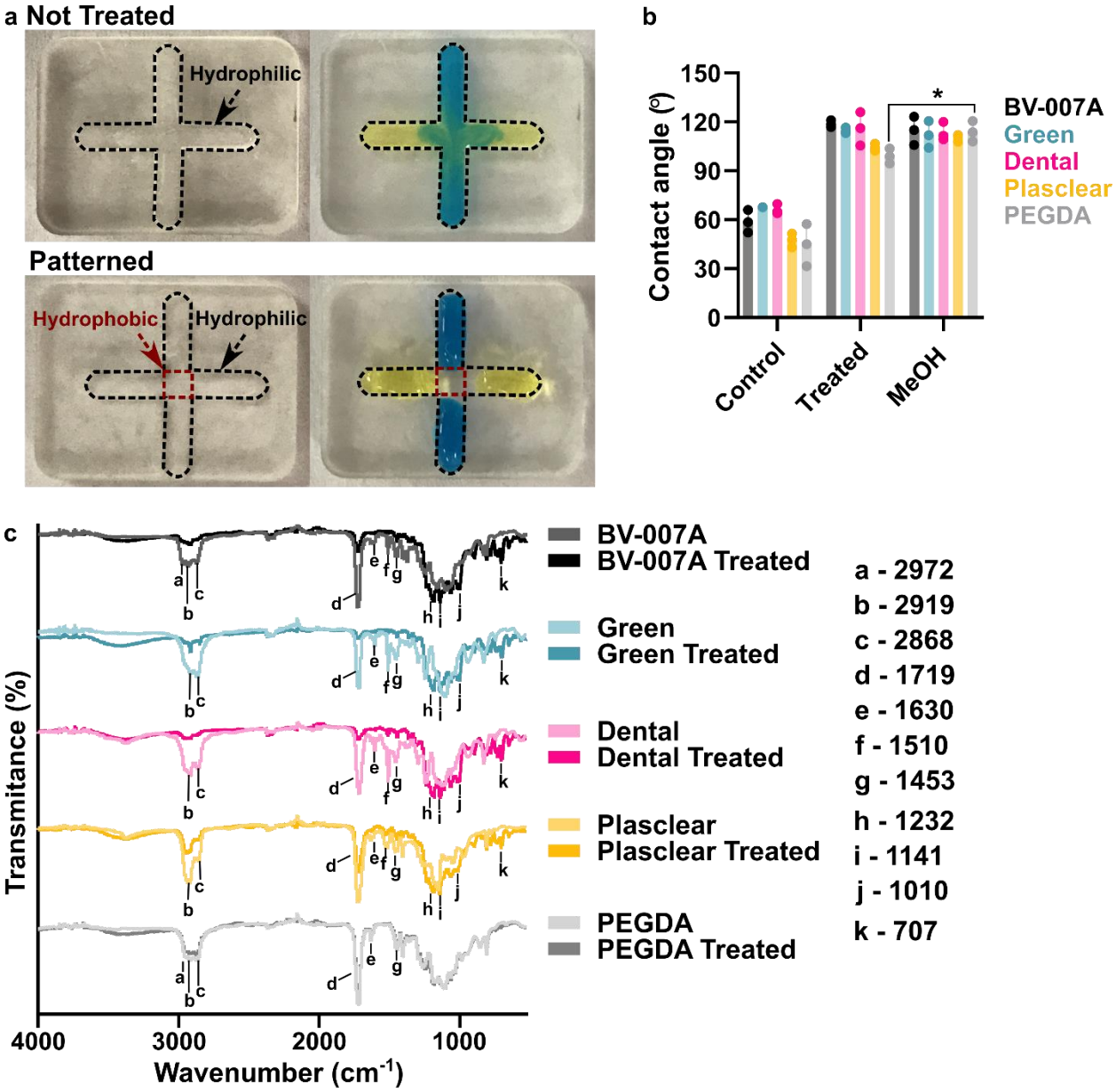

*Figure 4.7 Using the optimized silanization procedure for surface patterning and on other SLA/DLP resins. (a) Photos showing selective surface patterning. Parts printed in BV-007A were patterned so that the center of the cross was hydrophobic. In a non-silanized piece (top), the blue and yellow food dyes mixed in the center; in the piece patterned by local silanization (bottom), the droplets remained distinct from each other. The width of the channels was 2 mm. (b) Air/water contact angles for resins prior to silanization, after silanization with the optimized procedure, and after soaking in methanol (n=3 printed parts for each condition, mean ± std dev). Two-way ANOVA with Tukey's multiple comparisons tests (ns, $p>0.05$, ** $p<0.005$). (c) ATR FT-IR spectra of pieces printed using the various resins, before and after silanization (n=3 printed parts for each condition).*

4.4.6 Silanization of a suite of SLA resins demonstrates broad applicability

This silanization protocol would be most useful if applicable across a variety of SLA and DLP resins. Therefore, in addition to BV-007A, we tested three commercially available resins: Dental (FormsLab), Green Master Mold resin (CADworks3D), and Plasclear (iMakr), plus a polyethylene glycol diacrylate (PEG-DA)-based resin developed by the Folch laboratory.[30] Based on our prior data that the extent of reaction correlated with diminished absorbance from the carbonyl in the IR spectrum, we hypothesized that any resin with an acrylate (BV007A and PEG-DA) or methacrylate (Dental, Green Master Mold, and Plasclear) backbone, or possibly with carbonyl-containing photoinitiators or photoabsorbers, would react with the fluoroalkyl silane. Following the optimized protocol, all printed pieces were submerged in a 10% (v/v) solution of fluorinated silane in FC-40 oil for 30 min, without plasma treatment. This procedure successfully increased the contact angle for each material compared to its non-treated control (Figure 4.7b). The Green Master Mold, Dental, and BV007 resins were highly hydrophobic after silanization, with contact angles of ~ 115-118˚. In contrast, the PEG-DA and Plasclear resins had a mildly hydrophobic contact angle, near 100˚. This trend was reproduced in two independent experiments. To ensure that any physically adsorbed silane was removed, the silanized pieces were soaked for 2 hours in methanol.[47] In all cases, the hydrophobic surface persisted, again suggesting that the silane was covalently bound (Figure 4.7b). Surprisingly, the contact angle increased for both the Plasclear and PEGDA resins, an observation that remains to be explored.

We examined the surface chemistry of the printed pieces by ATR FT-IR to potentially explain the difference in susceptibility to silanization between resins (Figure 4.7c). The pair of peaks at 1453 and 1510 cm^{-1} are useful to distinguish PMMA from poly(methyl acrylate) (PMA).[48] The 1453 cm^{-1} peak, which was present in all samples, is attributable to a methylene vibration -CH2-

found in both PMMA and PMA. The peak at 1510 cm^{-1}, attributable to the methyl vibration C-CH3, is indicative of PMMA. This peak was present in all four commercial resins tested, suggesting the presence of methacrylates in these materials; as expected, it was not seen in the PEGDA sample. A small peak at 1630 cm^{-1}, assigned to C=C bonds from residual (meth)acrylate monomers,[49] was present in all samples.

Next, changes in the surface IR spectra after silanization were examined. The three resins that exhibited a larger change in contact angle after silanization (BV-007A, Green Master Mold, and Dental) also showed a larger decrease in the intensity of the carbonyl peak at 1719 cm^{-1} (Figure 4.7c). Furthermore, the decrease in the carbonyl peak correlated with appearance of peaks consistent with deposition of the fluoroalkyl silane. The peaks at 1232, 1142 and 707 cm^{-1} were again assigned to stretches and wagging of the fluoroalkyl chain,[20,43] and they increased after silanization for the four commercial resins. Similarly, the peak at 1010 cm^{-1} that increased after silanization in the commercial resins may be a part of the Si-O-R stretch (usually a strong and broad stretch, 1000-1100 cm^{-1}).[42] In contrast, Plasclear and PEGDA, which had smaller changes in contact angle, showed less consumption of the carbonyl, and PEGDA showed no increase in the finger print region. From these data, we concluded that while all five resins showed an increase in contact angle that was resistant to removal by methanol, only a fraction of them formed a covalent bond that consumed a carbonyl. It may be significant that PEGDA, which has no added photoabsorbers, was the least reactive of the materials towards the silane, this possibility was not tested further here.

4.5 Conclusions

We have demonstrated a robust and versatile strategy to control the surface chemistry and hydrophobicity of DLP 3D printed parts by reacting the printed surface with an alkyl-fluorinated silane. This method required only submerging the resin pieces in a silane solution, without any pre-treatment. The reaction between the silane and the resin appeared to consume a carbonyl present in the resin material, and was consistent with covalent bond formation. The fluorinated surface was resistant to mechanical damage, methanol soaking, and 50 days of storage, and the method was compatible with printed parts even after significant light exposure. Selective patterning of a hydrophobic surface was demonstrated in 3D printed open channels by a simple masking method. Furthermore, the method was effective with a suite of (meth)acylate based resins, with higher contact angles correlating with greater consumption of the carbonyl. We anticipate that simple approach to controlling the surface chemistry of resin 3D printed microfluidic parts, including for selective fluorination of specific regions, will advance the fabrications of complex two-phase devices and enable greater control of the wettability of 3D printed parts.

4.6 References

1. Bhattacharjee, N., Urrios, A., Kang, S. & Folch, A. The upcoming 3D-printing revolution in microfluidics. *Lab Chip* **16**, 1720–1742 (2016).
2. Waheed, S. *et al.* 3D printed microfluidic devices: enablers and barriers. *Lab Chip* **16**, 1993–2013 (2016).
3. Jiang, P., Ji, Z., Wang, X. & Zhou, F. Surface functionalization – a new functional dimension added to 3D printing. *J. Mater. Chem. C* **8**, 12380–12411 (2020).

4. Ward, L. J., Badyal, J. P. S., Goodwin, A. J. & Merlin, P. J. Solventless coupling of perfluoroalkylchlorosilanes to atmospheric plasma activated polymer surfaces. *Polymer* **46**, 3986–3991 (2005).
5. Yallup, K. & Iniewski, K. *Technologies for Smart Sensors and Sensor Fusion*. (CRC Press, 2014).
6. Grover, W. H., von Muhlen, M. G. & Manalis, S. R. Teflon films for chemically-inert microfluidic valves and pumps. *Lab Chip* **8**, 913 (2008).
7. Halvey, A. K., Macdonald, B., Dhyani, A. & Tuteja, A. Design of surfaces for controlling hard and soft fouling. *Phil. Trans. R. Soc. A.* **377**, 20180266 (2019).
8. Du, W., Li, L., Nichols, K. P. & Ismagilov, R. F. SlipChip. *Lab Chip* **9**, 2286–2292 (2009).
9. Shui, L., Eijkel, J. C. T. & van den Berg, A. Multiphase flow in microfluidic systems – Control and applications of droplets and interfaces. *Advances in Colloid and Interface Science* **133**, 35–49 (2007).
10. Köster, S. *et al.* Drop-based microfluidic devices for encapsulation of single cells. *Lab Chip* **8**, 1110–1115 (2008).
11. Subramanian, B. *et al.* Surface Modification of Droplet Polymeric Microfluidic Devices for the Stable and Continuous Generation of Aqueous Droplets. *Langmuir* **27**, 7949–7957 (2011).
12. Lee, J., Moon, H., Fowler, J., Schoellhammer, T. & Kim, C.-J. Electrowetting and electrowetting-on-dielectric for microscale liquid handling. *Sensors and Actuators A: Physical* **95**, 259–268 (2002).
13. J. Jebrail, M., S. Bartsch, M. & D. Patel, K. Digital microfluidics: a versatile tool for applications in chemistry, biology and medicine. *Lab on a Chip* **12**, 2452–2463 (2012).

14. Kobayashi, T., Shimizu, K., Kaizuma, Y. & Konishi, S. Novel combination of hydrophilic/hydrophobic surface for large wettability difference and its application to liquid manipulation. *Lab on a Chip* **11**, 639–644 (2011).
15. Feng, W., Ueda, E. & Levkin, P. A. Droplet Microarrays: From Surface Patterning to High-Throughput Applications. *Advanced Materials* **30**, 1706111 (2018).
16. Feng, Y., Zhou, Z., Ye, X. & Xiong, J. Passive valves based on hydrophobic microfluidics. *Sensors and Actuators A: Physical* **108**, 138–143 (2003).
17. Kotz, F., Risch, P., Helmer, D. & Rapp, B. Highly Fluorinated Methacrylates for Optical 3D Printing of Microfluidic Devices. *Micromachines* **9**, 115 (2018).
18. Helmer, D. *et al.* Transparent, abrasion-insensitive superhydrophobic coatings for real-world applications. *Sci Rep* **7**, 15078 (2017).
19. Wang, X. *et al.* i3DP, a robust 3D printing approach enabling genetic post-printing surface modification. *Chem. Commun.* **49**, 10064–10066 (2013).
20. Gupta, M. & Gleason, K. K. Initiated Chemical Vapor Deposition of Poly(1H,1H,2H,2H-perfluorodecyl Acrylate) Thin Films. *Langmuir* **22**, 10047–10052 (2006).
21. Thompson, B. *et al.* Engineered hydrophobicity of discrete microfluidic elements for double emulsion generation. *Microfluid Nanofluid* **20**, 78 (2016).
22. de Givenchy, E. T. *et al.* Fabrication of Superhydrophobic PDMS Surfaces by Combining Acidic Treatment and Perfluorinated Monolayers. *Langmuir* **25**, 6448–6453 (2009).
23. Nishino, T., Meguro, M., Nakamae, K., Matsushita, M. & Ueda, Y. The Lowest Surface Free Energy Based on −CF3 Alignment. *Langmuir* **15**, 4321–4323 (1999).

24. Waheed, S. *et al.* Enhanced physicochemical properties of polydimethylsiloxane based microfluidic devices and thin films by incorporating synthetic micro-diamond. *Scientific Reports* **7**, 15109 (2017).
25. Carrell, C. S., McCord, C. P., Wydallis, R. M. & Henry, C. S. Sealing 3D-printed parts to poly(dimethylsiloxane) for simple fabrication of Microfluidic devices. *Analytica Chimica Acta* **1124**, 78–84 (2020).
26. Ohtani, K. *et al.* Surface Treatment of Flow Channels in Microfluidic Devices Fabricated by Stereolithography. *Journal of Oleo Science* **63**, 93–96 (2014).
27. Anderson, A. & Ashurst, W. R. Enabling Organosilicon Chemistries on Inert Polymer Surfaces with a Vapor-Deposited Silica Layer. *Langmuir* **25**, 11541–11548 (2009).
28. Antonucci, J. M., Dickens, S. H., Fowler, B. O., Xu, H. H. K. & McDonough, W. G. Chemistry of Silanes: Interfaces in Dental Polymers and Composites. *J Res Natl Inst Stand Technol* **110**, 541–558 (2005).
29. Weikart, C. M. & Yasuda, H. K. Modification, degradation, and stability of polymeric surfaces treated with reactive plasmas. *Journal of Polymer Science Part A: Polymer Chemistry* **38**, 3028–3042 (2000).
30. Urrios, A. *et al.* 3D-printing of transparent bio-microfluidic devices in PEG-DA. *Lab Chip* **16**, 2287–2294 (2016).
31. Catterton, M. A., Dunn, A. F. & Pompano, R. R. User-defined local stimulation of live tissue through a movable microfluidic port. *Lab Chip* **18**, 2003–2012 (2018).
32. Saini, G., Sautter, K., Hild, F. E., Pauley, J. & Linford, M. R. Two-silane chemical vapor deposition treatment of polymer (nylon) and oxide surfaces that yields hydrophobic (and

superhydrophobic), abrasion-resistant thin films. *Journal of Vacuum Science & Technology A* **26**, 1224–1234 (2008).

33. Mayer, T. M., de Boer, M. P., Shinn, N. D., Clews, P. J. & Michalske, T. A. Chemical vapor deposition of fluoroalkylsilane monolayer films for adhesion control in microelectromechanical systems. *J. Vac. Sci. Technol. B* **18**, 2433 (2000).
34. Duffy, D. C., McDonald, J. C., Schueller, O. J. A. & Whitesides, G. M. Rapid Prototyping of Microfluidic Systems in Poly(dimethylsiloxane). *Anal. Chem.* **70**, 4974–4984 (1998).
35. Grate, J. W. *et al.* Correlation of Oil–Water and Air–Water Contact Angles of Diverse Silanized Surfaces and Relationship to Fluid Interfacial Tensions. *Langmuir* **28**, 7182–7188 (2012).
36. Kim, Y. M., Arkles, B. & Pan, Y. The Role Of Polarity In The Structure Of Silanes Employed In Surface Modification. in *Silanes and Other Coupling Agents, Volume 5* 51–64 (Brill Academic Publishers, 2009). doi:10.1163/ej.9789004165915.i-348.37.
37. Ii, E. G., Barankin, M. D., Guschl, P. C. & Hicks, R. F. Surface Activation of Poly(methyl methacrylate) via Remote Atmospheric Pressure Plasma: Surface Activation of Poly(methyl methacrylate) via Remote …. *Plasma Processes Polym.* **7**, 482–493 (2010).
38. Huszank, R., Szilágyi, E., Szoboszlai, Z. & Szikszai, Z. Investigation of chemical changes in PMMA induced by 1.6 MeV He+ irradiation by ion beam analytical methods (RBS-ERDA) and infrared spectroscopy (ATR-FTIR). *Nuclear Instruments and Methods in Physics Research Section B: Beam Interactions with Materials and Atoms* **450**, 364–368 (2019).
39. Pawde, S. M. & Deshmukh, K. Surface characterization of air plasma treated poly vinylidene fluoride and poly methyl methacrylate films. *Polymer Engineering & Science* **49**, 808–818 (2009).

40. Riau, A. K. *et al.* Surface Modification of PMMA to Improve Adhesion to Corneal Substitutes in a Synthetic Core–Skirt Keratoprosthesis. *ACS Appl. Mater. Interfaces* **7**, 21690–21702 (2015).
41. Tang, L. & Lee, N. Y. A facile route for irreversible bonding of plastic-PDMS hybrid microdevices at room temperature. *Lab Chip* **10**, 1274–1280 (2010).
42. Launer, P. & Arkles, B. Infrared Analysis of Organosilicon Compounds: Spectra-Structure Correlations. *Gelest* (2013).
43. Hoque, E., DeRose, J. A., Houriet, R., Hoffmann, P. & Mathieu, H. J. Stable Perfluorosilane Self-Assembled Monolayers on Copper Oxide Surfaces: Evidence of Siloxy−Copper Bond Formation. *Chem. Mater.* **19**, 798–804 (2007).
44. Abasi, C. Y., Wankasi, D. & Dikio, E. D. Adsorption Study of Lead(II) Ions on Poly(methyl methacrylate) Waste Material. *Asian J. Chem.* **30**, 859–867 (2018).
45. Tey, J. N., Soutar, A. M., Mhaisalkar, S. G., Yu, H. & Hew, K. M. Mechanical properties of UV-curable polyurethane acrylate used in packaging of MEMS devices. *Thin Solid Films* **504**, 384–390 (2006).
46. Decker, C. & Zahouily, K. Photodegradation and photooxidation of thermoset and UV-cured acrylate polymers. *Polymer Degradation and Stability* **64**, 293–304 (1999).
47. Long, T. M., Prakash, S., Shannon, M. A. & Moore, J. S. Water-Vapor Plasma-Based Surface Activation for Trichlorosilane Modification of PMMA. *Langmuir* **22**, 4104–4109 (2006).
48. Kotera, A., Shima, M., Akiyama, K., Kume, M. & Miyakawa, M. Copolymerization Characteristics of Methyl Acrylate and Methyl Methacrylate. II. Analysis of Methyl Acrylate-Methyl Methacrylate Copolymers by Infrared Spectroscopy. *BCSJ* **39**, 758–761 (1966).

49. Hadavand, B. S. & Hosseini, H. Investigation of viscoelastic properties and thermal behavior of photocurable epoxy acrylate nanocomposites. *Science and Engineering of Composite Materials* **24**, 691–697 (2017).

Chapter 5: Rapid fabrication of a polymeric SlipChip with movable ports by digital light processing 3D printing

5.1 Abstract:

SlipChips are microfluidic devices comprised of two parts separated by an oil layer that can be reconfigured to change fluidic pathways. These types of devices are able to perform a wide range of functions, including tissue stimulation. In most cases, SlipChip device functionality is dependent on an optically clear, smooth, and flat surface that is fluorophilic and hydrophobic. Currently, fabrication of these devices at the prototype stage requires a skilled microfluidic technician, e.g. for wet etching or alignment steps. Here, we used digital light processing (DLP) 3D printing is a rapid, reproducible and sharable fabrication method for microfluidic devices. As a case study, we used a movable microfluidic port device is a SlipChip comprised of two multi-layer components: an enclosed channel with a delivery port and a culture chamber for tissue slices with a permeable support. The movable port device was used as a case study for the fabrication of SlipChips with DLP 3D printing. Clear 3D printed parts were assessed for their optical transparency, flatness, and susceptibility for fluorination, which is critical for SlipChips. The device design was optimized for both components, focusing on printability of the channels, ports, and chip-to-world connections. The 3D printed SlipChip was able to deliver aqueous solution from the bottom to top components without leakage into the oil layer. We demonstrated the function of the device by locally delivering a tracer solution to a slab of hydrogel and a living tissue slice, with as low as 120-µm resolution. By demonstrating the compatibility of 3D printing with fabrication of SlipChip devices, this work will enhance the ability to rapidly prototype such devices at mid-scale levels of production.

5.2 Introduction

The ability to produce microchips easily and with minimal manual assembly, while retaining rapid prototyping capabilities, is highly desirable for pushing microfluidic devices past the first hand-built prototype stage. Scaled up fabrication is critical to conducting experiments at moderate scale (dozens of devices) and for propagating such technology to collaborators. In particular, this scale of fabrication would be useful for SlipChips, which are two-phase, reconfigurable microfluidic devices. SlipChips usually comprise of two planar components that can be "slipped" relative to one another that contain recessed features to hold droplets or streams of aqueous solution, and are separated by a thin layer of oil.[1] SlipChip devices were first developed in the Ismagilov lab [1] as a new technology to perform in low resource settings.[2–4] The first SlipChips were fabricated from glass plates, which offer ideal surface properties and optical clarity but require wet etching with HF, a hazardous procedure that requires a skilled technician [1,5]. Since then, many different Slip-based designs have evolved, including rotational based Slipdisc and paper-based SlipPADs, to perform a wide range of laboratory processes such as PCR, cell culture and local delivery to tissue slices.[6–15] Novel slip-based devices that have multiple layers per component have complex fabrication and bonding strategies, which hinders production scale and prototyping.[10,14] Injection molding simplifies fabrication at large scale, but it is not compatible with prototyping.[16] An alternative method is needed to fabricate SlipChips at a moderate scale, while retaining the ability to rapidly prototype.

Any fabrication system for SlipChip devices must be able to meet three major requirements needed for SlipChip function, in addition to fabricating the features needed for the intended application. First, the surfaces in contact with the central oil layer must flat and smooth, which is necessary to create a small (< 2 μm) gap height of between the two components. This gap height

requirement has been previously demonstrated in other SlipChips.[2] Next, to prevent the aqueous phase from spreading into the oil-filled gap between components, these surfaces must be hydrophobic. If a fluorinated oil is used, a fluorophilic surface is preferred. Finally, for SlipChips that rely on visual alignment or optical detection, the layers must be optically transparent.

We considered that digital light projection (DLP) 3D printing, which uses UV or blue light to cure photocrosslinkable resins layer-by-layer,[17,18] may facilitate SlipChip fabrication and allow for rapid prototyping. This additive method is quickly gaining popularity for fabricating small parts and microfluidic devices, because of the high feature resolution and reproducibility in parts and rapid fabrication speed compared to traditional soft-lithography.[19–22] While 3D printing has not been reported previously for SlipChips, two of the three fabrication requirements are met: We recently described a method for fluorination of a DLP-printed surface based on a solvent-based deposition of a fluoroalkyl silane, and others have demonstrated smooth and transparent prints by using clear resins on a glass surface.[23,24]

As a case study for fabrication of a SlipChip by 3D resin printing, we considered a microfluidic movable port device (MP device) previously developed by our lab [10]. Local delivery devices like this one are used to study intrinsic tissue properties and to screen for potential drugs.[10,15,25–28] The MP device lessens the amount of user-handling of a tissue slice, by repositioning the port below a tissue slice for local delivery with the device. The MP device is a SlipChip that consists of two multilayer components. The bottom component contains an enclosed channel terminating in a single microfluidic delivery port (channel component), and the top component features a semipermeable tissue culture well (chamber component). In the original hand-built prototype, an

extensive fabrication process limited the accessibility and distribution of the MP device to other labs and collaborators.[10]

Before a MP device could be rapidly fabricated by DLP printing, there were three challenges remaining to be addressed**.** The first challenge, applicable to any 3D printed SlipChip, was ensuring that the two surfaces closest to the oil gap must be flat across the width of the component (30 mm). Photocurable resins shrink when crosslinked, inducing mechanical stress that can warp the print if not addressed in the print design.[29] The second challenge is integration of an array of microscale ports and enclosed channel in a manner compatible with commercial 3D printers,[30] without disrupting the flat surface. The third challenge, specific for biological applications, was biocompatibility of the printed resin with tissue slices housed in the delivery component. The question of resin toxicity is of great interest to the microfluidics community and is still under active investigation.[24,31,32]

Here, we established an approach to fabricate a 3D printed SlipChip for the first time, using the MP device as a case study. First, we validated the selection of a DLP resin designed for microfluidic devices to meet the optical transparency, surface roughness, surface chemistry, and viability requirements of the movable port device. Next, the device design for fabrication with a DLP print was optimized to minimize the fabrication time and fabrication steps. Finally, the functionality was tested by delivering aqueous solutions to both agarose and lymph node tissue slices, to confirm the absence of leaks into the gap and the ability to stimulate locally.

5.3 Methods

5.3.1 Device design, 3D printing, and laser etching

All 3D printed parts were designed using Autodesk Inventor 2018. The CAD files were sliced at 50 µm intervals using MII Utility Shortcut V 3.27 and printed using a CADworks3D M50-405 printer (MiiCraft, CADworks3D Toronto, Canada) in BV-007A resin (MiiCraft, CADworks 3D). The printer settings for the BV-007A resin at a 50-µm slice height was a slow peeling speed, 0.1 mm gap adjustment (unless printing on glass which was 0.27 mm), 1.15 s curing time, 1 base layer, 9.0 s base curing time, 1 buffer layer, and 75% light power. To print parts on glass, a cover glass slide 36 x 60 mm with a thickness of 0.13-0.17 mm (Ted Pella, Redding, CA, USA) was attached to the baseplate by curing a thin layer of BV-007A, with a 405 nm UV-light (Amazon, Seattle, WA, USA).[24] The parts were rinsed with methanol (Fisher Chemical) and post-cured in a UV-light box for 20 s. To complete the chamber component, an array of ports with an 80-µm diameter were laser etched (Versa Laser 3.5, Universal Laser Systems, Scottsdale AZ, USA) into the printed BV-007A part, using a power setting of 7% and a speed of 10%.

5.3.2 Surface profilometry

To assess surface roughness, the root mean square deviation of the surface height of the printed parts were measured with a Zygo optical surface profilometer (Zygo, Berwyn, PA, USA) at the Nanoscale Materials Characterization Facility at UVA. An 8 x 8 x 8 mm^3 cubes were printed, and surface roughness was measured on all sides, specifically the surfaces: printed against the aluminum baseplate or printed against glass, closest to the polytetrafluoroethylene (PTFE) sheet at the bottom of the vat, and the sides of the print. As a positive control, a glass slide plated with 30 nm of Au/Pd by a Technics sputter coater (Technics) was also analyzed.

5.3.3 Fluorination of resin surface and contact angle measurements

Parts printed in BV-007A was silanized using our recently described method.[23] The parts were submerged into a 10% v/v solution of tridecafluoro-1,1,2,2-tetrahydrooctyl trichlorosilane (Gelest Inc., Morrisville PA, USA) in Fluorinert FC-40 (Sigma Aldrich, St. Louis, MO, USA) for 30 min at room temperature. The surfaces were rinsed with 95% ethanol (Koptec) and DI water and finally dried with a nitrogen gun.

Surface air/water contact angles and three-phase contact angles were measured on cubic printed pieces (8 x 8 x 15 mm^3) using a ramé-hart goniometer (model 200-00, ramé-hart instrument co., Succasunna NJ, USA) and DROPimage Advanced software. The contact angle was measured in triplicate (3 separate printed pieces per condition), by pipetting one 5-µL droplet of 1x phosphate buffered saline (PBS) (DPBS without calcium or magnesium (Lonza, Walkersville, MD, U.S.A.) onto the smooth, flat face printed against the PTFE sheet of the cube. For three-phase contact angle, the printed cube with a droplet was inverted into a cuvette filled with FC-40 oil containing 0.5 mg/mL triethyleneglycol mono[1H,1H-perfluorooctyl]ether (R_fOEG) synthesized in-house as reported previously.[10]

5.3.4 Measurement of curvature of printed pieces

Images of the side profiles of 3D printed 30 x 30 mm prism with various heights (2 – 5 mm) were collected using a Zeiss AxioZoom microscope. The displacement from horizontal due to curvature was manually measured in Zen 2 software.

5.3.5 Animal work and tissue slice collection

All animal work was approved by the Institutional Animal Care and Use Committee at the University of Virginia under protocol #4042, and was conducted in compliance with guidelines

the Office of Laboratory Animal Welfare at the National Institutes of Health (United States). Both male and female C57BL/6 mice aged 19 - 21 weeks (Jackson Laboratory, USA) were housed in a vivarium and given water and food ad libitum. Lymph nodes were harvested from the mice following humane isoflurane anesthesia and cervical dislocation. The tissues were sliced according to a previously published protocol.[33] Briefly, peripheral lymph nodes were collected and embedded in 6% w/v low melting point agarose (Lonza, Walkersville MD, USA) in 1× PBS. After the agarose had hardened, agarose blocks containing lymph nodes were extracted with a 10 mm tissue punch (World Precision Instruments, Sarasota, FL, USA). The blocks were mounted with super glue on a stage and sliced into 300-μm thick sections using a Leica VT1000S vibratome (Bannockburn, IL, USA) in ice-cold 1× PBS. The lymph nodes were sliced at a speed setting of 90 (0.17 mm/s) and frequency of 3 (30 Hz). Slices were cultured in "complete RPMI": RPMI (Lonza, 16-167F) supplemented with 10% FBS (VWR, Seradigm USDA approved, 6 89510-186), 1× L-glutamine (Gibco Life Technologies, 25030-081), 50 U/mL Pen/Strep (Gibco), 50 μM beta-mercaptoethanol (Gibco, 21985-023), 1 mM sodium pyruvate (Hyclone, GE USA), 1× non-essential amino acids (Hyclone, SH30598.01), and 20 mM HEPES (VWR, 97064–362). Slices of 6% agarose was collected in a similar manner but were stored in 1 x PBS instead of complete media.

5.3.6 Analysis of tissue viability

To assess the viability of lymphocytes after a brief exposure to BV-007A, tissue slices were placed in 10 mm diameter well in 30 x 30 x 5 mm 3D printed parts filled with 1x PBS for 15 min at room temperature. Then all slices used in viability experiments were cultured in "complete media" for 4 hr at 37˚C with 5% CO_2. Following a previously established protocol,[33,34] the viability of live lymph node tissue slices was assessed by flow cytometry. Briefly, individual slices were crushed to generate cell suspensions. The suspensions were stained with 75 μL of 67 nM Calcein

AM (eBioscience, San Diego, CA, USA) in 1x PBS for 20 min at 37˚C. Stained samples were washed by centrifugation at 400 g for 5 min and brought up in 1x PBS + 2% FBS (flow buffer). 5 μg/mL of 7-AAD (AAT Bioquest, Sunnyvale, CA, USA) was then added to the cell suspension. The samples were run on a Guava 4-color cytometer (6-2L) and analyzed using the Guava® InCyte™ Software. Single stain compensation controls were run on crushed lymph node slices. The Calcein-AM single stain contained a 1:1 mixture of Calcein-labelled and unstained live cells. The 7-AAD single stain contained a 1:1 mixture of live and killed cells; the latter were prepared by treating cells with 35% ethanol for 10 mins. Calcein positive and 7-AAD negative cells were defined as viable cells.

5.3.7 Assembly and local delivery with the 3D printed SlipChip

Prior to assembling the SlipChip, the channel in the delivery component was filled using pressure-driven flow via a Chemyx syringe pump (Fusion 200, Houston TX, USA). A 0.5 mg/mL solution of FITC-conjugated dextran (150 kDa and 70-kDa for agarose and tissue deliveries experiments respectively) was flowed into the channel using a 50 μL Hamilton syringe (model 1705 RN; 26 s gauge, large hub needle) and non-shrinkable PTFE TT-30 tubing (0.012 in. I.D., 0.009 in. wall thickness, Weico Wire, Edgewood NY, USA). Next, 500 μL of FC-40 oil containing 0.5mg/mL R_fOEG was pipetted onto the top of the filled delivery component. Then, the chamber component was lowered onto the delivery component and the two components were clamped together with two binder clips, sandwiching a thin layer of oil between them. The culture chamber on the top of the chip was then filled with 1× PBS. A sample of agarose gel or tissue was placed into the chamber and weighed down using a small stainless-steel washer (10 mm O.D. and 5.3 mm I.D., Grainger USA). The chamber component was manually slipped relative to the delivery component and visually aligned under a microscope to align to a desired port. To initiate a delivery,

the syringe pump was turned on at a flow rate specified for each experimetn. After 5 seconds, the pump was turned off and the device was slipped away, to reposition for another delivery or to a closed position. After all deliveries were complete, the sample was removed, and the chamber was flushed with 1× PBS and refilled for the next sample. All delivery experiments were performed at room temperature.

All deliveries were monitored in real time using a Zeiss AxioZoom upright microscope with a PlanNeoFluor Z 1×/0.25 FWD 56 mm objective, Axiocam 506 mono camera and HXP 200 C metal halide lamp (Zeiss Microscopy, Germany), using filter cubes for GFP (Zeiss filter set #38), and Violet Chroma Filter (49021, ET-EBFP2). Images (16 bit) were collected before, during, and after delivery. During deliveries, time lapse images were collected at 1 s intervals. All images were analyzed in Zen 2 software.

5.3.8 Analysis of delivery widths

After alignment of the delivery port to an array port below a 6% agarose slice, a pulse of Fluorescein (FITC) labeled 150 kDa dextran was delivered to the slice at flow rates ranging from 0.2 to 1 μL min^{-1} (n = 3). After delivery, the device was slipped to remove the background fluorescence of the channel from beneath the delivery. Delivery width was determined from image analysis as previously described.[28] Line scans were drawn across the radial delivery and the background autofluorescence of the resin was subtracted. The data was fit to a Gaussian curve in GraphPad Prism version 8. The width was defined as 2 standard deviations of the Gaussian curve. To fit the curve of the spread of analyte with respect to time, we used the previously published analytical model,[10] using Equation 3.2 and 3.3.

5.3.9 Delivery to lymph node tissue

The device was assembled and a lymph node slice was placed onto the chamber. A 5 second pulse of FITC-labeled 70 kDa dextran was delivered at a flow rate of 0.25 μL min^{-1}. After the first delivery, the device was repositioned and another delivery was performed. This was repeated for four different slices and with slight variations on the number of deliveries on three separate occasions.

5.4 Results and Discussion

5.4.1 DLP Resin material considerations for use in a SlipChip device

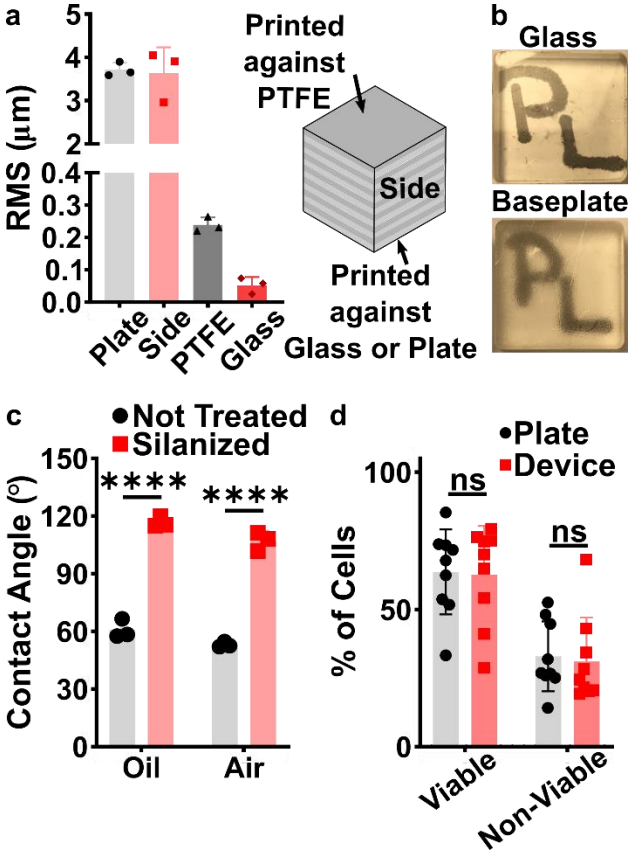

*Figure 5.1 Investigation the compatibility of the resin of, surface roughness, optical transparency, surface chemistry, and biocompatibility (a) The root mean square (rms) of the surfaces was measured for BV-007A printed against a micro-milled aluminum baseplate, the final print layer closest to the PTFE vat bottom, printed against a glass slide, or the side of the print (n=3, mean ± Std Dev). A schematic of a resin cube with the different faces for surface roughness measurements labeled. (b) An image of a clear resin (BV-007A) printed on glass or the micro milled aluminum baseplate. (c) The contact angle of the BV-00A was increased using a fluoroalkyl silane (n=3, mean ± Std Dev) Two-way ANOVA turkey's multiple comparison test, **** $p < 0.0001$. Air and oil refer to the phase surrounding the water droplets on the resin surface. The oil phase contained 0.5 mg/mL R_fOEG) (d) The percent of viable and non-viable cells after 15 min exposure to BV-007A resin compared to a plate control (n=9, mean ± Std Dev) Two-way ANOVA turkey's multiple comparison test, $p > 0.05$. Cells were considered viable if they were high in calcein AM and low in 7-AAD. Non-viable was any cell high in 7-AAD.*

Before designing the microfluidic device, we first selected and validated a resin for its suitability for the intended use of the SlipChip. First, we addressed the surface roughness and optical transparency of the DLP printed parts. Glass, a well-validated material for SlipChip fabrication, had a surface roughness (root mean square (RMS) of a surface) of 5 ± 0.5 nm (n=3). However in the past, some SlipChips have included 2-µm posts to set a gap height between the two glass components.[2] Therefore, we considered that surface roughness ≤ 2 µm would be acceptable. This degree of smoothness will allow for a small gap height between parts which prevents the aqueous phase from leaking between the two components. For surface roughness, we investigated the surface of various sides of a BV-007A cube (8x8x8 mm) in comparison to the

surface of glass. The surface roughness for four different printing conditions: against baseplate, against glass, sides of the print, or against PTFE was measured by an optical profilometer (Figure 5.1a). As expected, the surfaces printed against the baseplate and on the sides of the cube were rough, with RMS > 3 μm (Figure 5.1a). In contrast, the surface roughness of the faces printed against glass and PTFE were both ≤ 0.3 μm (Figure 5.1a), which was determined to be sufficiently smooth. From this data, we concluded that the print must be oriented such that the surfaces intended to contact the oil gap layer in the assembled device are printed against glass or the PTFE sheet. Additionally as previously described,[24] printing against glass provides optical transparency to a printed part. Optical transparency was demonstrated by comparing a rectangular prism in a clear resin (BV-007A) that was printed against glass to the opacity of a print done against a rough aluminum baseplate (Figure 5.1b). The optical transparency obtained by printing against glass allows for visual alignment of channels and ports in the movable port device.

The surface chemistry of BV-007A can be modified to be fluorophilic and hydrophobic. The surface of the components in contact with the oil must be hydrophobic and fluorophilic. Both glass and plastic SlipChips have used a fluoroalkyl silane to achieve this surface chemistry.[2,10] Recently, we described a fluoroalkyl silanization method for SLA resins. [23] Here, this method was applied to the BV-007A and the three-phase contact angle of a 1 x PBS droplet in FC-40 oil, on the surfaces of the resins interface was larger than 115° (Figure 5.1c), which will ensure no leaking between the two components.[10]

The MP Device is intended to be used with live tissue slices; therefore, it is critical that tissue viability is not affected by the BV-007A printed pieces. During use of the movable port device, the tissue slice is in contact with the material only for the short period that the delivery occurs (less

than 5 min for the alignment and multiple deliveries). Lymph node tissue slices were used to test viability, because primary cells in tissues are fragile and applications of the device depends on the ensured viability of the tissue smaple.[10] We tested an exposure period of 15 min to triple the time spent in contact with the resin during use of the device. The viability after this short exposure was comparable to slices that were never in contact with the printed material (Figure 5.1d). In the future, we hope to identify a resin that is biocompatible with tissue for longer time periods and provides the high print resolution of BV-007A.

5.4.2 Optimization of the key features of the channel component.

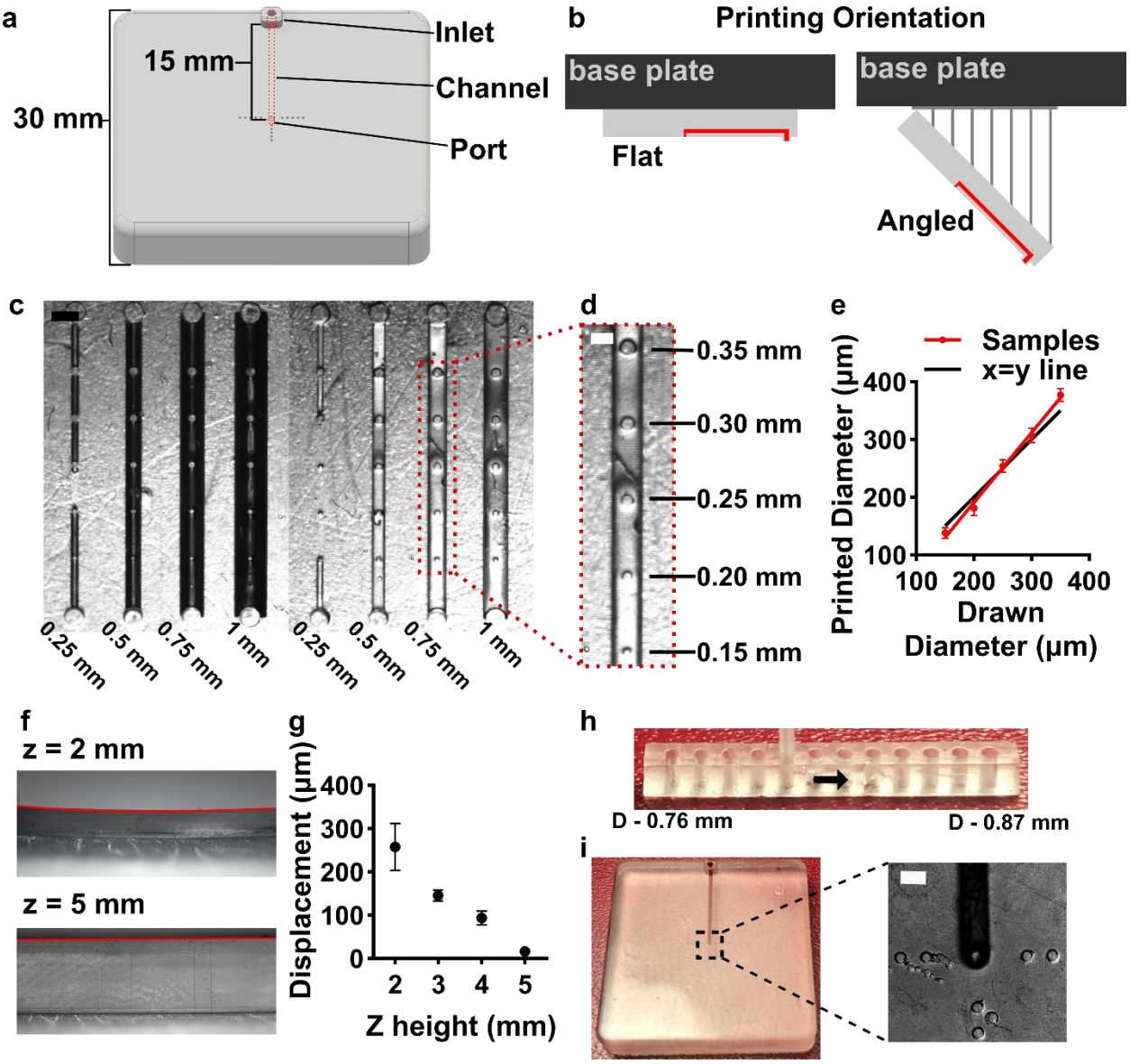

Figure 5.2 The optimization of the channel component of the movable port device. (a) The channel design shown as the AutoCAD inventor drawing. (b) Schematic of printing orientation need to achieve a smooth surface on the top of the component (flat) compared to a rough surface orientation (angled). The red line represents the enclosed channel. (c) An image of the channel optimization piece which varied the cross-section dimensions (0.25 x 0.25 – 1 x 1 mm legs), cross-section shape (diamond versus square) and port diameters. (d) Inset of ports on top of channel (0.35 mm -0.15 mm diameter). (e) Printed diameter of port versus drawn dimension (mean ± Std Dev, n=8) fit to the line y = 1.2x – 51. The black line is x=y. (f) Image of print warping decreasing by increasing the height (z) of the print. (g) Displacement of the print from horizontal (µm) versus the height of the print (mm) (mean ± Std Dev, n=3). (h) Inlet connection optimization part used to fit a PTFE tubing (0.78 OD) with the tightest connection. (i) An image of the channel component with the channel filled with red food dye, inset shows a micrograph of the delivery port with alignment markers, scale bar 0.5 mm.

For the channel component (Figure 5.2a), the key features were the enclosed channel, the delivery port, and the inlet. Before optimizing the features, the orientation of the print was considered to ensure a smooth surface was generated on the side of the component with the delivery port. As seen previously, the face of the print will affect the smoothness of the surface. For DLP printing, a common practice is to print at 45˚ angles to achieve higher resolution features in the prints (Figure 5.2b, angled). This does not work for the MP device, since the printed surface that would contain the delivery port would then be on the side of a print with a rough beveled surface. Therefore, all printing optimization must be done with the design oriented flat against the baseplate to achieve a smooth surface on the top component (Figure 5.2b, flat).

The enclosed channels must be optimized to minimize the channel cross-section that can be printed (Figure 5.2c). The length of a channel will affect how small of a channel cross-section can be printed, because it affects how easily the part can be cleared of unreacted resin through the small terminating delivery port. A 15-mm length channel was necessary to ensure the terminating end can be positioned anywhere below the port array of the chamber component. The cross-section size (1 x 1 – 0.25 x 0.25 mm) and shape (diamond or square oriented relative to the baseplate) were varied for 15-mm long channels (Figure 5.2c). The minimum cross-section dimension printed was 0.5 x 0.5 mm for both shapes. Fluorescence background from the channel can be seen during a delivery through transparent materials. Therefore, by choosing the square over the diamond shape design for enclosed channels, the horizontal width of each channel feature was minimized (Figure 5.2c).

The delivery ports diameter was optimized in a similar manner (Figure 5.2d). All ports were successfully printed above the channel with diameter ranging from 0.35-0.15 with close fidelity to drawn dimension (Figure 5.2e). Ports with a diameter below 0.15 mm failed to print when tested

in another array (Figure 5.3). The channel was also printed close to the top of the part to minimize UV-exposure from subsequent steps. This position helped to prevent the channel from becoming blocked during printing.

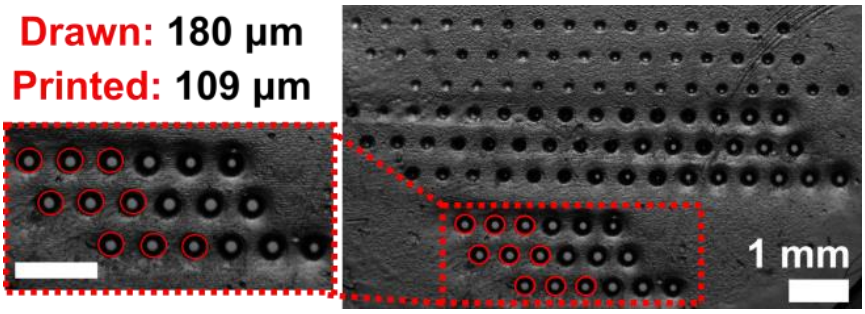

Figure 5.3: Port array for size optimization. Outlined and in the insert are the two fully printed port (n=9 ports completely printed) sizes with the chosen port size of drawn 180 µm is outlined in red.

A flat profile was essential to the channel component to minimize gap height within the device. The flat profile was achieved by rounding the sharp corners and increasing the height (z) of the print to minimize stress during printing.[35,36] Polymerization of resins causes shrinkage and associated stress that results in the parts deforming by curling out of plane, which unacceptably increases the gap height between parts.[35] The height of the print (z) was varied (2 - 5 mm) (Figure 5.2f) and a 30 x 30 mm footprint required at least 5 mm thickness to prevent the part from curling (Figure 5.2g). We hypothesize that the additional layers added strength to the part that was greater than the stress that caused curling in thinner parts.

To connect with the real world a simple female connection inlet was used to fit the 0.78 OD PTFE tubing (Figure 5.2h). Mock inlets ranging in diameter from 0.76 - 0.87 mm were printed and PTFE tubing was tested for a tight fit. The 0.8 mm diameter was determined to give a snug fit that would prevent leaking at the inlet. Utilizing all the optimized conditions, a flat and smooth 3D printed channel component could be successfully printed that had a simple inlet and an enclosed channel that terminated in the smallest delivery port possible (Figure 5.2i).

5.4.3 Optimization of the chamber component.

The key feature that needed optimization in the chamber component was the support for the tissue, which allows for delivery to the tissue from below and remains transparent for visual alignment. We originally tried to create a 1-step fabrication method by either embedding a mesh support, or directly printing the port array (Figure 5.4a and b). We found it simple to embed a mesh in the component by adding it to the baseplate or glass prior to printing (Figure 5.4a). Unfortunately, due to resin shrinking during polymerization, the mesh would not remain taught. Additionally, COMSOL modeling predicted that the increased distance from the delivery port caused by the mesh would greatly increase the minimum delivery width in tissue (Data not shown).

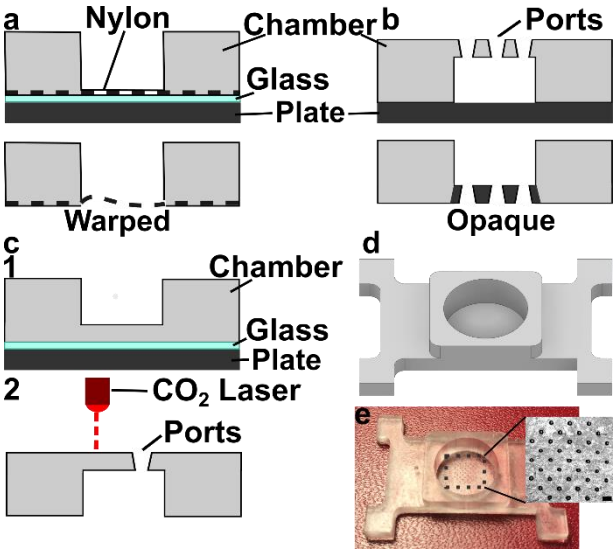

Figure 5.4 The optimization of the chamber component of the movable port device. Three fabrication strategies were tested: (a) incorporating a mesh, (b) directly printing and (c)laser etching the ports after printing. (d and e) The optimized design of the chamber component shown as the AutoCAD inventor drawing and the 3D printed pieces, inset the ports etched into the chamber scale bar 0.5 mm.

Next, we attempted to directly print the small ports in an array (Figure 5.4b and Figure 5.3). The orientation during printing affected both the minimum port size and the transparency of the print. The bottom of the chamber component must be smooth, which means it needed to be printed against glass or the Teflon vat. When the bottom of the chamber is oriented so that it was printed against glass on the baseplate, the first layer is usually overexposed to ensure the print adhered to the glass for the duration of the printing process. This necessary step prevents small

features from being printed in the first couple of layers due to the small bleed over of light from overexposure. Next, we tested printing the ports could when the chamber was oriented so that the bottom of the component is closest to the Teflon vat. To identify the smallest reproducible delivery port through 300-µm, we printed an array of ports sizes 30—190 µm in diameter (n=9) (Table 5.1 and Figure 5.3). Ports drawn with 180 µm diameter were the smallest to print all replicates, with final diameter of 109 ± 4 µm (Figure 5.3), similar to the size of the ports in our prior local delivery SlipChip [10]. Unfortunately, the resulting orientation of the component created an unsupported overhang during printing which led to the stretching of the unsupported part of the print. The stretching of the component created a distorted region that was not transparent. Since there was no way to fabricate the port array in a single step that met all the requirements for the movable port chamber, we elected to use a two-step process (Figure 5.4c).

Table 5.1 Port diameter was optimized for consistency and the smallest size (n=9).

Drawn Diameter (µm)	% Printed	Actual Diameter (µm)
140	0	NA
150	22	57 ± 1
160	44	74 ± 1
170	88	85 ± 10
180	100	109 ± 4
190	100	119 ± 26

After printing the chamber component on glass with the bottom of the chamber closest to the glass, a CO2 laser was used to etch a port array into the chamber in a similar manner to the previously published device.[10] The resulting ports had a diameter of 81 ± 2 µm (n=74) with no bump on the gap side of the device (Figure 5.5),

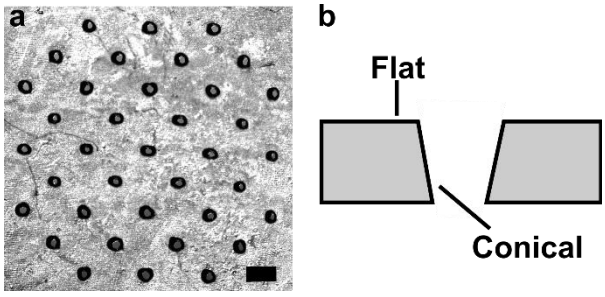

Figure 5.5 Laser etched port shapes. (a) An enlarged version of the inset in Figure 5.4 of the laser etch port array. The scale bar is 0.5 mm. (b) A side view of the created ports with a flat profile on both sides of the port which was different from the original device.

which is within the range of the port width of the MP device array.[10] While this approach requires access to a laser etcher (e.g. an inexpensive trophy etcher), both processes are rapid (<1 min to etch the array), and the chamber is made of a single material (Figure 5.4d and e).

5.4.4 The DLP printed Movable Port SlipChip was tested for functionality

To test that the device does not leak into the gap during use, the device was assembled (Figure 5.6a and b) and used for three short deliveries, this was repeated for two more reassemblies of the device. During and after deliveries fluorescent and brightfield imaging was used to monitor the gap area and no interface between the aqueous and oil phases were observed for 9 out of 9 deliveries. This means that as long as the device is aligned correctly there will be no risk of the aqueous phase spreading into the gap. Next, we measured the delivery widths of FITC labeled 150

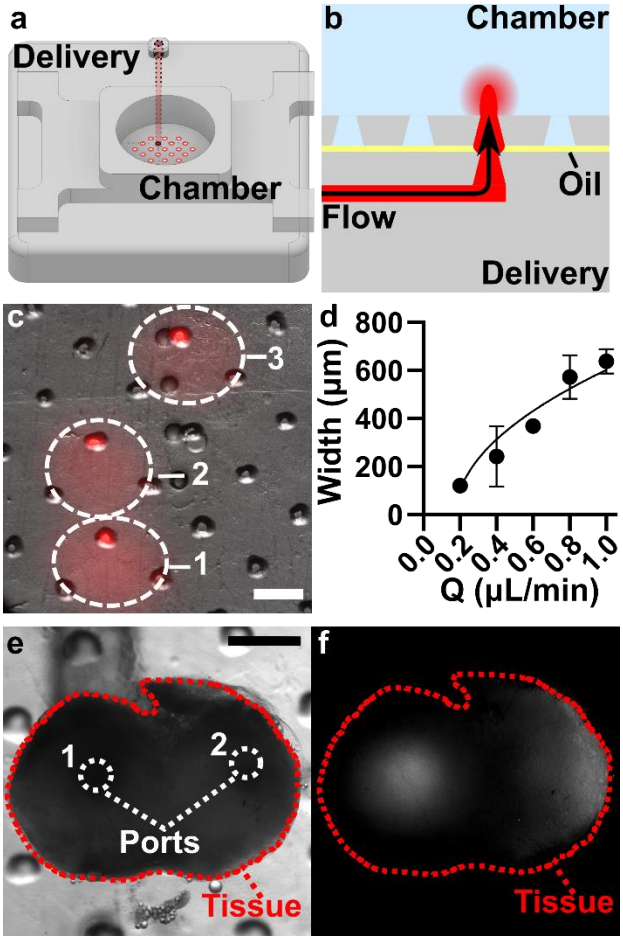

Figure 5.6 Demonstration of local delivery to both agarose and live tissue slices. (a) A schematic of the assembled device. (b) Sideview of the delivery through the device. (c) An image after three deliveries to a slab of agarose. The fluorescent dextran deliveries to the transparent agarose are outlined by white dotted lines. Scale bar 500 µm. Numbers indicate the order of the subsequent deliveries. (d) A graph of delivery widths as a function of flow rate (mean ± Std Dev, n=3). Fit to a curve $y = 663\sqrt{x - 0.178}$, R^2= *0.85 (e) A brightfield image of a tissue slice outlined in red in the assembled device prior to delivery. The ports used for sequential deliveries were outlined in white and number indicate order of deliveries. Scale bar 500 µm. (f) a fluorescent image of two deliveries of FITC labeled 70 kDa dextran (white signal) to the live tissue.*

kDa dextran delivered to 6% agarose to ensure the device could target sub-structures in tissues. Due to the high background caused by the channel, deliveries with a diameter smaller than the width of the channel cannot be observed until the delivery port is slipped away after delivery. Delivery widths were measured for a range of flow rates after a 5 sec pulse delivery, at various locations within the same agarose slice (Figure 5.6c and d). This demonstrated that the device was robust enough to withstand multiple slipping and alignment steps and showed that delivery widths could target substructures of a lymph nodes (0.2 µL/min flow rate had a width of 120 µm.[37] Next, we delivered to multiple location in live tissue slices. Since the tissue is opaque the targeting specific regions relied on the alignment markers incorporated on the delivery component. Distinct regions within the lymph nodes were successfully targeted during delivery (Figure 5.6e and f).

5.4.5 Future outlook for the technical advancement of the movable port device.

The next critical step for the MP device is extending the culture of tissue on chip. Biocompatibility of SLA resins is one of the major hurdles for adoption of the fabrication method for a large number of microfluidic devices. There are many components of the SLA resin, such as monomers, photoinitiators and photoabsorbers, and plasticizers that may affect the viability of a biological sample.[24] In our initial studies, we attempted to culture cells overnight using a variety of post-processing treatments on BV-007A to remove cytotoxic components, but found no treatment that would improve viability of cells after a 24 hour exposure to BV-007A (Data not shown). This issue will be discussed further in **Chapter 6**.

There are two major limitations to the current design of the movable port devices. The first is the use of binder clips, which requires a skilled hand to be able to slip the device. Another way to clamp the two components together would be to use magnets. This would require a design that included magnet holders but still allowed the components to move freely in both the x- and y-

directions during alignment. Novel clamping methods can now be explored with the ability to rapid prototype changes of the device design using the new fabrication method. A second major limitation with the current version is the large fluorescent background of the channel. A micromanipulator could be used with the device to control the slipping without the need for visual alignment. This would allow for printing the components in an opaque material that minimizing the background fluorescence from the channel during imaging steps. Additionally, without the need to for visual alignment the previously explored direct printing method for the chamber component could be used further simplifying the device fabrication.

5.5 Conclusion:

This paper demonstrates the first 3D printed SlipChip with the movable port device as a case study. DLP 3D printing produces smooth flat surfaces that can be chemically modified to become selectively fluorinated, which is necessary for SlipChips. The resin parts were biocompatible with short term (15 min) exposures needed for local delivery to tissue slices. The channel component was designed to be printed in a singles step and contain an inlet, enclosed channel and small terminating delivery port. The chamber component required a two-step fabrication using laser etching but the average port size in the chambers array was reduced from the previous device. The device was shown to be able to perform multiple slipping and delivery steps without leakage in between the components. The spread of the delivery was again dependent of pump-driven flow and able to target sub-structures in a tissue slice. The new DLP 3D printing fabrication method will enable the movable port technology to become accessible to other labs, by greatly simplifying the fabrication steps, materials, and time. Rapid prototyping with DLP 3D printing is essential for future improvements to the movable port device as well as advancing other novel SlipChip device designs.

5.6 References:

1. Du, W., Li, L., Nichols, K. P. & Ismagilov, R. F. SlipChip. *Lab. Chip* **9**, 2286 (2009).
2. Pompano, R. R., Platt, C. E., Karymov, M. A. & Ismagilov, R. F. Control of initiation, rate, and routing of spontaneous capillary-driven flow of liquid droplets through microfluidic channels on SlipChip. *Langmuir* **28**, 1931–1941 (2012).
3. V. Zhukov, D. *et al.* Microfluidic SlipChip device for multistep multiplexed biochemistry on a nanoliter scale. *Lab. Chip* **19**, 3200–3211 (2019).
4. Li, L., Du, W. & Ismagilov, R. User-Loaded SlipChip for Equipment-Free Multiplexed Nanoliter-Scale Experiments. *J. Am. Chem. Soc.* **132**, 106–111 (2010).
5. Culbertson, C. T., Sibbitts, J., Sellens, K. & Jia, S. Fabrication of Glass Microfluidic Devices. in *Microfluidic Electrophoresis: Methods and Protocols* (ed. Dutta, D.) 1–12 (Springer, 2019). doi:10.1007/978-1-4939-8964-5_1.
6. Yu, M. *et al.* Multistep SlipChip for the Generation of Serial Dilution Nanoliter Arrays and Hepatitis B Viral Load Quantification by Digital Loop Mediated Isothermal Amplification. *Anal. Chem.* **91**, 8751–8755 (2019).
7. Li, L. & Ismagilov, R. F. Protein crystallization using Microfluidic technologies based on valves, droplets, and SlipChip. (2010) doi:10.1146/annurev.biophys.050708.133630.
8. Liang *et al.* Individually addressable arrays of replica microbial cultures enabled by splitting SlipChips. *Integr. Biol.* **6**, 796 (2014).
9. Chang, C.-W., Peng, C.-C., Liao, W.-H. & Tung, Y.-C. Polydimethylsiloxane SlipChip for mammalian cell culture applications. *Analyst* **140**, 7355–7365 (2015).
10. Catterton, M. A., Dunn, A. F. & Pompano, R. R. User-defined local stimulation of live tissue through a movable microfluidic port. *Lab. Chip* **18**, 2003–2012 (2018).

11. Shen, F. *et al.* Multiplexed Quantification of Nucleic Acids with Large Dynamic Range Using Multivolume Digital RT-PCR on a Rotational SlipChip Tested with HIV and Hepatitis C Viral Load. *J. Am. Chem. Soc.* **133**, 17705–17712 (2011).
12. Li, X., Scida, K. & Crooks, R. M. Detection of Hepatitis B Virus DNA with a Paper Electrochemical Sensor. *Anal. Chem.* **87**, 9009–9015 (2015).
13. Lyu, W. *et al.* Slip-driven microfluidic devices for nucleic acid analysis. *Biomicrofluidics* **13**, 041502 (2019).
14. Banerjee, I. *et al.* Slipdisc: a versatile sample preparation platform for point of care diagnostics. *RSC Adv.* **7**, 35048–35054 (2017).
15. Ross, A. E. & Pompano, R. R. Diffusion of cytokines in live lymph node tissue using microfluidic integrated optical imaging. *Anal. Chim. Acta* **1000**, 205–213 (2018).
16. Schoepp, N. G. *et al.* Rapid pathogen-specific phenotypic antibiotic susceptibility testing using digital LAMP quantification in clinical samples. *Sci. Transl. Med.* **9**, (2017).
17. Hull, C. W. Apparatus for production of three-dimensional objects by stereolithography. (1986).
18. Quan, H. *et al.* Photo-curing 3D printing technique and its challenges. *Bioact. Mater.* **5**, 110–115 (2020).
19. Waheed, S. *et al.* 3D printed microfluidic devices: enablers and barriers. *Lab. Chip* **16**, 1993–2013 (2016).
20. Amin, R. *et al.* 3D-printed microfluidic devices. *Biofabrication* **8**, 022001 (2016).
21. Bhattacharjee, N., Urrios, A., Kang, S. & Folch, A. The upcoming 3D-printing revolution in microfluidics. *Lab. Chip* **16**, 1720–1742 (2016).

22. Mehta, V. & Rath, S. N. 3D printed microfluidic devices: a review focused on four fundamental manufacturing approaches and implications on the field of healthcare. *Bio-Des. Manuf.* **4**, 311–343 (2021).
23. Catterton, M., Montalbine, A. N. & Pompano, R. Versatile and Selective Fluorination of the Surface of Polymeric Materials After Stereolithography 3D Printing. (2021) doi:10.26434/chemrxiv.14167472.v1.
24. Urrios, A. *et al.* 3D-printing of transparent bio-microfluidic devices in PEG-DA. *Lab. Chip* **16**, 2287–2294 (2016).
25. Chang, T. C. *et al.* Parallel microfluidic chemosensitivity testing on individual slice cultures. *Lab Chip* **14**, 4540–4551 (2014).
26. Horowitz, L. F., Rodriguez, A. D., Ray, T. & Folch, A. Microfluidics for interrogating live intact tissues. *Microsyst. Nanoeng.* **6**, 69 (2020).
27. Mohammed, J. S., Caicedo, H. H., Fall, C. P. & Eddington, D. T. Microfluidic add-on for standard electrophysiology chambers. *Lab. Chip* **8**, 1048–1055 (2008).
28. Ross, A. E., Belanger, M. C., Woodroof, J. F. & Pompano, R. R. Spatially resolved microfluidic stimulation of lymphoid tissue ex vivo. *The Analyst* **142**, 649–659 (2017).
29. Karalekas, D., Rapti, D., Gdoutos, E. E. & Aggelopoulos, A. Investigation of shrinkage-induced stresses in stereolithography photo-curable resins. *Exp. Mech.* **42**, 439–444 (2002).
30. Beauchamp, M. J., Nordin, G. P. & Woolley, A. T. Moving from millifluidic to truly microfluidic sub-100-μm cross-section 3D printed devices. *Anal. Bioanal. Chem.* **409**, 4311–4319 (2017).
31. Warr, C. *et al.* Biocompatible PEGDA Resin for 3D Printing. *ACS Appl. Bio Mater.* **3**, 2239–2244 (2020).

32. Piironen, K., Haapala, M., Talman, V., Järvinen, P. & Sikanen, T. Cell adhesion and proliferation on common 3D printing materials used in stereolithography of microfluidic devices. *Lab. Chip* **20**, 2372–2382 (2020).
33. Belanger, M. C. *et al.* Acute Lymph Node Slices Are a Functional Model System to Study Immunity Ex Vivo. *ACS Pharmacol. Transl. Sci.* **4**, 128–142 (2021).
34. Ball, A. G., Belanger, M. C. & Pompano, R. R. Detergent wash improves vaccinated lymph node handling ex vivo. *J. Immunol. Methods* **489**, 112943 (2021).
35. Ligon, S. C., Liska, R., Stampfl, J., Gurr, M. & Mülhaupt, R. Polymers for 3D Printing and Customized Additive Manufacturing. *Chem. Rev.* **117**, 10212–10290 (2017).
36. Huang, Y.-M. & Lan, H.-Y. Compensation of distortion in the bottom exposure of stereolithography process. *Int. J. Adv. Manuf. Technol.* **27**, 1101–1112 (2006).
37. Willard-Mack, C. L. Normal Structure, Function, and Histology of Lymph Nodes. *Toxicol. Pathol.* **34**, 409–424 (2006).

Chapter 6: Conclusions and Future Directions

6.1 Conclusions

Here I have demonstrated the application of a microfluidic device for local delivery with a model of diseased tissue using live slices from vaccinated lymph nodes and progressed local delivery technology with a movable microfluidic port. Events in vivo begin from a local source and it is imperative that we are able to mimic them when studying ex vivo tissue slices.

In **Chapter 2**, I measured the diffusivity and tortuosity of inflamed lymph node tissue using a microIOI technique. These results indicated that there might be adjuvant-dependent changes to the diffusivity of the tissue. In tissues slices vaccinated with CFA and Poly(I:C) we saw increased diffusion coefficients for both 3 and 10 kDa on day 4 post-vaccination compared to slices vaccinated with Alum and the vehicle control. For the larger, 70 kDa, dextran and model immunotherapies there was no change in the diffusion coefficients on this day for any vaccinated condition, suggesting that any change in the extracellular space in the tissue was smaller than the hydraulic radius of those molecules. These trends need to be verified at physiological temperatures, and a biological explanation for the change in diffusivity needs to be investigated. A novel method to measuring width of the extracellular space in live ex vivo tissue would be a powerful technique that can answer questions about the change in the extracellular space in vaccinated lymph nodes. Understanding changes in transport during immune responses could lead to improved design and development of immunotherapies.

Chapter 3 reported a novel movable microfluidic port device fabricated with a SlipChip design for live tissue stimulation. Delivery occurred by aligning a delivery port beneath a user-selected port in an array and using pump-driven flow to control the amount, and therefore the width, of the delivery. A layer of biocompatible oil between the two components of the chip prevented leaking

between the components and lubricated the chip for slipping. Incorporation of pump-driven flow was an innovation in SlipChip design, and we showed that successful delivery was due to the high capillary pressure in the system. Sequential local deliveries to live tissue were possible without manual realignment of the tissue, and novel deliver in patterns could be achieved that would not possible with static ports. The device is expected to be compatible with any mechanically stable soft tissue sample or hydrogel, and could be used to study the effects of local fluid flow and drug delivery.

In **Chapter 4**, I demonstrated a robust and versatile strategy to control the surface chemistry and hydrophobicity of digital light processing (DLP) 3D printed parts through silanization. The method required submerging the resin pieces in a fluorinated-alkyl silane solution, without any pre-treatment to the piece. IR spectroscopy revealed that reaction between the silane and the resin appeared to consume a carbonyl present in the resin material, and was consistent with covalent bond formation. The fluorinated surface generated by this method was robust, demonstrating resistance to mechanical damage, methanol soaking, and 50 days of storage, and the process was compatible with printed parts even after significant light exposure. Selective patterning of a hydrophobic surface was achieved with a simple masking method. The method was compatible with a suite of (meth)acrylate-based resins, which continue to demonstrate that higher contact angles correlated with greater consumption of the carbonyl. With this simple approach to controlling the surface chemistry of resin 3D printed microfluidic parts, two-phase devices like a SlipChip can be fabricated using 3D printing.

The first 3D printed SlipChip was demonstrated in **Chapter 5**. DLP resin printing was shown to simplify the fabrication of the movable port device by reducing procedural steps, materials, and time compared to the original prototype. DLP 3D printing produced the smooth, flat, and optically

clear pieces, which were necessary for a SlipChips device. These properties for the printed parts were achieved by printing against glass or a polytetrafluoroethylene (PTFE) sheet. The resin parts were biocompatible within the short-term (15 min) exposures needed for local delivery to tissue slices. The channel component was designed to be printed in a singles step and contained an inlet, enclosed channel and small terminating delivery port. The chamber component required a two-step fabrication using laser etching, but the average port size in the chamber's array was reduced from the previous device. The device was shown to be able to perform multiple slipping and delivery steps without leakage in between the components. The spread of the delivery was, again, dependent of pump-driven flow and able to target sub-structures in a tissue slice. The new fabrication method will make movable port technology more accessible to other labs, and allow for more complex designs to be tested by rapid prototyping.

Here, I have present novel microfluidic device that will advance local delivery to tissue slices. These types of devices have the potential to investigate healthy and diseased tissue, be used to screen and study novel and existing drugs, and perform local stimulation to investigate cell signaling propagation in tissue, when coupled with novel spatial and temporally resolved in-tissue assays. I think success for a microfluidic device can be defined by its ability to be spread to collaborators for their own use. With the new 3D printed method, I believe the technology I have created can aid collaborators interested in probing the local microenvironment of a tissue.

6.2 Future Directions

6.2.1 Biocompatibility of 3D resin

Extending the ability to culture on DLP 3D printed resin while retaining high printing resolution is the first crucial step toward further incorporation of 3D printed local delivery technology with tissue slices. Biocompatibility of photopolymerized resins is a hot topic necessary

for the field of microfluidics used for biological applications.[1,2] Some commercially available resins claim to be biocompatible, such as those used in the dental industry for implants. Even if a commercially available resin claims biocompatibility, the certification level may not be appropriate for long-term culture with primary cells or tissue slices, especially lymph node slices. Resins that claim biocompatibility may also not have the resolution necessary for printing enclosed microfluidic channels, and exhibit autofluorescence and opacity that would limit some imaging techniques.[3] Solutions to this problem has taken two major approaches: post-processing treatments for the prints and changing resin formulations to make them less toxic.

The first approach of post-processing can be broken down further into two main categories, leaching or removing hazardous components from the printed pieces or coating the surface and forming a barrier between the cells and the hazardous components.[1,4,5] Both approaches have merit but are not easily replicated or applicable for all resins and microfluidic designs. For example, in our own experiments we have found that for BV-007 resins, any extended cleaning procedures compromise the integrity of the printed part and have not improved long term viability (data not shown). Coatings, such as medical grade Parylene-C, can improve biocompatibity but ensuring an even coat that does not block small features may be challenging to achieve.[1]

The second approach is to use a novel resin formulation. Many companies are working towards this solution but in the meantime, there are some promising in-house formulations that have been developed. These formulations use a high molecular weight polyethelyneglycol diacrylate (PEGDA), with little to no additives besides the photo-initator.[5,6] The published formulations that we tested in-house have not performed as well with our primary lymphocytes, and also had poor resolution for printing enclosed channels due to the lack of photoabsorbers in the formulation. The attraction for developing a resin is the complete control that comes with

creating an in-house formulation, that a resin can be modified to fit the parameters needed for your microfluidic device.

I believe that the solution to biocompatibility will be a middle ground between these two solutions. Any novel resin will probably require additional post-processing to be biocompatible. Solving the issue of biocompatibility is crucial for the longevity of all digital light process DLP 3D printed microfluidic devices that are intended for use with cell or tissue culture.

6.2.2 Modifications to the movable port device design

Now that there is a way to rapidly fabricate a movable microfluidic port device, novel device designs can be attempted. This was demonstrated in Chapter 5 with the three different chamber fabrication methods, but the design was only extended far enough to recreate a device similar to the original microfluidic port. What I am proposing here would be designs that will further extend the purpose of the device, and to add a new dimensionality to the delivery.

6.2.2.1 Creating a modular chamber component for long term culture applications

Assaying the tissue post-local stimulation by delivery will require further handling steps, and possible culturing steps. It could be of great interest to further the movable ports device's original goal of minimizing the user handling, by using the chamber component as a culturing tool. Modular chips are microfluidic devices that allow the user to redesign their device before, during, or after an experiment.[7–9] It would be an interesting, and a not far-reaching, challenge to combine the modular approach with the current SlipChip.

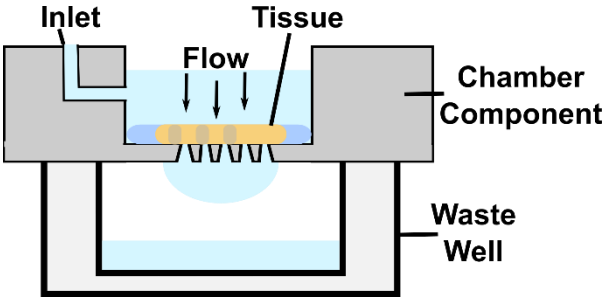

Figure 6.1 Conceptual design for culturing with chamber component of the movable port device.

The chamber component of the device could be redesigned to act as a transwell for culturing purposes when not assembled for delivery (Figure 6.1). This would require biocompatible resin materials before long term culture could be performed. Transversal flow (flow through the tissue) would be a beneficial addition to culture that could be possible with the chamber component. A challenge for this extension would be ensuring that the reassembly with a filled chamber is possible and that oil does not enter into the culture chamber. When assembled in the current design the chamber is empty and then flushed prior to slices being placed into the chip to avoid any excessive oil from being in the chamber. The oil is biocompatible but the droplets could keep the tissue from lying flat against the ports, which is critical to minimize size of the local delivery.

6.2.2.2 Further development of device design to incorporate multiple channels

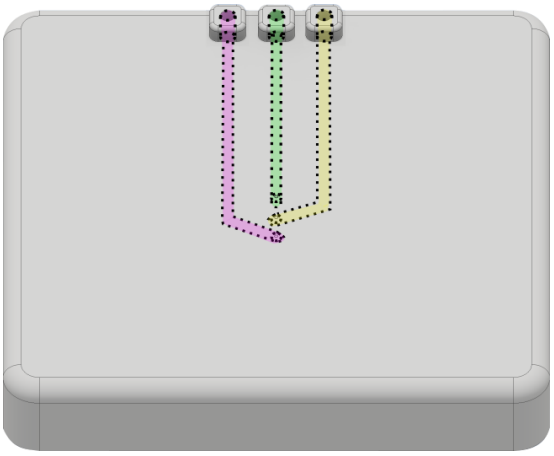

Figure 6.2 Conceptual design of a three-channel delivery component for the movable port device.

Currently, the device does not allow for delivery of analytes that react with one another. If we could deliver through more than one channel, we could begin to use a more complex delivery experimental scheme (Figure 6.2). In pathology that uses immunohistochemistry sometimes labeling is done with a two-antibody system that allows for signal amplification. With two or more channels we could deliver a primary antibody with a target that has typically low expression in tissues to a

region of interest. Then with a second channel, a secondary antibody that is specific for the first can be delivered through the same port in the port array to bind and amplify the signal of the first antibody. One potential issue with this method would be non-specific binding due to a lack of wash steps. This could be solved with a third channel, which would not be any more difficult to incorporate into the design than two channels. A complex design like what has been proposed could open the opportunity to for future assays done by a movable port device.

6.2.3 Incorporating in-tissue assays for spatially resolved read-outs

Advances in in-tissue assays such as a 2-Deoxy-2-[(7-nitro-2,1,3-benzoxadiazol-4-yl)amino]-D-glucose (2-NBDG) assay which monitors glucose uptake in a spatiotemporal manner in tissues slices are starting to allow for more complex read-outs in tissue analysis.[10] With this type of assay, we can begin to probe deeper questions about signal propagation through the tissue. It would be especially interesting to compare to global stimulation to see if there is a change in cell behavior by the two different methods.

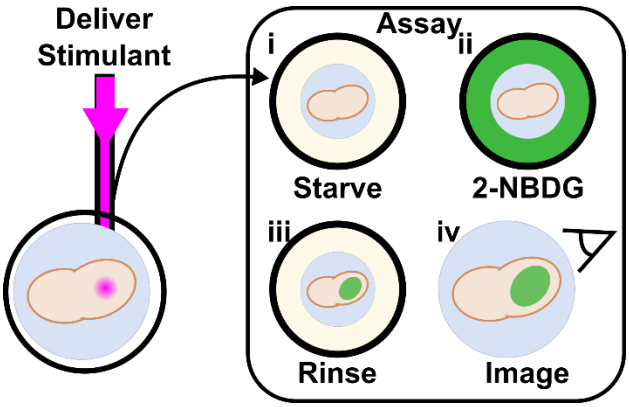

Figure 6.3 Schematic for local stimulation of lymph node coupled with a glucose uptake assay.

Some lymph nodes contain two distinct lobes, it would be interesting if we could stimulate a single lobe and see if the response stays contained within that half of the lymph node or if it creates a global response that spreads through the whole tissue (Figure 6.3). T cells can be activated in a short period of time with phytohaemagglutinin (PHA) or lipopolysaccharide (LPS). A 2-NBDG assay has already been proven to be able to spatially resolve glucose uptake in activated T cells within a tissue slice.[10] Even answering this simple question would be an exciting step forward in the lab's

goal of understanding signaling mechanisms underlying lymph node function. In the future, the lab will develop a dual affinity reagent to map cytokine secretion in lymph nodes. Coupled with the movable technology we could visualize the signal propagation in lymph node tissue.

6.2.4 Develop a microfluidic device for rapid immunohistostaining of live tissue slices.

Immunohistostaining was first developed for thin fixed slices, then adapted by our lab to be used in live tissue slices.[11] This current method relies on the diffusion of antibody through the tissue for transport to the respective receptor, creating a 2.5 hour long step, minimum, in an experimental set up. If convection could be used instead of diffusion, to transport the antibody though the tissue then there is a potential to greatly reduce the time needed for immunostaining. The staining reaction would then be limited to the binding coefficient (Kd) for each antibody. The washing steps after staining could also be improved with convection to remove any unbound antibody quickly as well.

A microfluidic device that can direct flow through a tissue slice could be used to stain tissues with antibodies in minutes. The device would also need to direct flow through a large enough area to cover the biological variation in tissue sample size. Some preliminary COMSOL modeling was done to predict the necessary inlet and outlet diameters need for such a device (Figure 6.4). Ideally the device would be simple enough to use that non-microfluidic users would feel comfortable running the device. Also, the device should be capable of multiplexing by staining multiple tissue slices in a single run. This type of device would expediate long experiments that use immunostained tissues, such as local delivery experiments, or metabolic in-tissue assays that use spatially resolved responses.

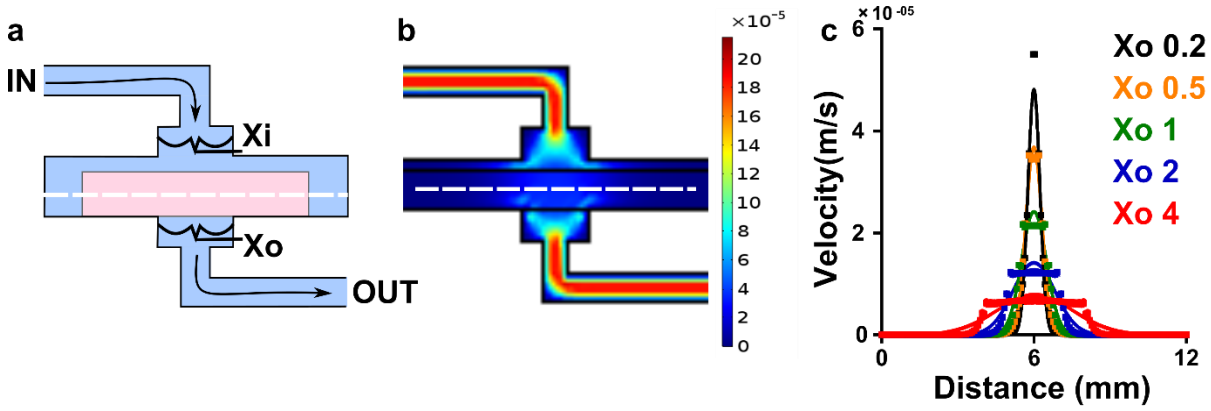

Figure 6.4 COMSOL modeling was used to simulate the fluid velocity through the device. (a) The two parameters that were changed in the simulation was the width of the inlet to the tissue chamber (Xi) and the width of the outlet underneath the tissue (Xo). This schematic shows both Xi and Xo along with the fluid movement through the device. For the simulation both Xi and Xo ranged from 0.2 to 4 mm. The white dotted line represents the line scan the length of the entire chamber. (b) An example of the resulting flow velocities through the device. A line scan is drawn at 150 μm into the tissue. The Xi was 0.5 mm and the Xo was 0.5 mm for this example simulation. (c) The resulting line scans velocities (m/s) of Xo were plotted against their location in the x direction of the line scan.

6.3 References:

1. Hart, C., Didier, C. M., Sommerhage, F. & Rajaraman, S. Biocompatibility of Blank, Post-Processed and Coated 3D Printed Resin Structures with Electrogenic Cells. *Biosensors* **10**, (2020).
2. Waheed, S. *et al.* 3D printed microfluidic devices: enablers and barriers. *Lab. Chip* **16**, 1993–2013 (2016).
3. Kreß, S. *et al.* 3D Printing of Cell Culture Devices: Assessment and Prevention of the Cytotoxicity of Photopolymers for Stereolithography. *Materials* **13**, (2020).
4. Liang, Y.-R. *et al.* 3D-Printed High-Density Droplet Array Chip for Miniaturized Protein Crystallization Screening under Vapor Diffusion Mode. *ACS Appl. Mater. Interfaces* **9**, 11837–11845 (2017).

5. Warr, C. *et al.* Biocompatible PEGDA Resin for 3D Printing. *ACS Appl. Bio Mater.* **3**, 2239–2244 (2020).
6. Urrios, A. *et al.* 3D-printing of transparent bio-microfluidic devices in PEG-DA. *Lab. Chip* **16**, 2287–2294 (2016).
7. Owens, C. E. & Hart, A. J. High-precision modular microfluidics by micromilling of interlocking injection-molded blocks. *Lab. Chip* **18**, 890–901 (2018).
8. Loskill, P., Marcus, S. G., Mathur, A., Reese, W. M. & Healy, K. E. μOrgano: A Lego®-Like Plug & Play System for Modular Multi-Organ-Chips. *PLOS ONE* **10**, e0139587 (2015).
9. Yuen, P. K. A reconfigurable stick-n-play modular microfluidic system using magnetic interconnects. *Lab. Chip* **16**, 3700–3707 (2016).
10. Dunn, A. F., Catterton, M. A., Dixon, D. D. & Pompano, R. R. Spatially resolved measurement of dynamic glucose uptake in live ex vivo tissues. *Anal. Chim. Acta* **1141**, 47–56 (2021).
11. Groff, B. D., Kinman, A. W. L., Woodroof, J. F. & Pompano, R. R. Immunofluorescence staining of live lymph node tissue slices. *J. Immunol. Methods* **464**, 119–125 (2019).